Multiscale Modeling of the Effects of Nanoscale Load Transfer on the Effective Elastic Properties of Carbon Nanotube-Polymer Nanocomposites

Yumeng Li

Dissertation submitted to the Faculty of the

Virginia Polytechnic Institute and State University

in partial fulfillment of the requirements for the degree of

Doctor of Philosophy

in

Aerospace Engineering

Gary D. Seidel, Chair

Romesh C. Batra

Rakesh K. Kapania

Mayuresh J. Patil

Sept. 29, 2014

Blacksburg, Virginia

Keywords: Multiscale modeling, carbon nanotube nanocomposites, interface, molecular dynamic simulation, cohesive zone, composite cylinder model, finite element analysis

Multiscale Modeling of the Effects of Nanoscale Load Transfer on the Effective Elastic Properties of Carbon Nanotube-Polymer Nanocomposites

Yumeng Li

ABSTRACT

A multiscale model is proposed to study the influence of interfacial interactions at the nanoscale in carbon nanotube(CNT)-polymer nanocomposites on the macroscale bulk elastic material properties. The efficiency of CNT reinforcement in terms of interfacial load transferring is assessed for the non-functionalized and functionalized interfaces between the CNTs and polymer matrix using force field based molecular dynamic simulations at the nanoscale. Polyethylene (PE) as a thermoplastic material is adopted and studied first because of its simplicity. Characterization of the nanoscale load transfer has been done through the identification of representative nanoscale interface elements for unfunctionalized CNT-PE interface models which are studied parametrically in terms of the length of the PE chains, the number of the PE chains and the "grip" position. Referring to the non-functionalized interface, CNTs interact with surrounding polymer only through weakly nonbonded van der Waals (vdW) forces in our study. Once appropriate values of these parameters are deemed to yield sufficiently converged results, the representative interface elements are subjected to normal and sliding mode simulations in order to obtain the force-separation responses at 100K and 300K for unfunctionalized CNT-PE interfaces. To study the functionalization effects, atomistic interface representative elements for functionalized CNT-PE interface are

built based on non-functionalized interface models by grafting functional groups between the PE matrix and the graphene sheet. This introduces covalent bonding forces in addition to the non-bonded vdW forces. A modified consistent covalent force field (CVFF) and adaptive intermolecular reactive empirical bond order (AIREBO) potentials, both of which account for bond breaking, are applied to investigate the interfacial characteristic of functionalized CNT-PE interface in terms of the force-separation responses at 100K in both normal opening and sliding mode separations. In these studies, the focus has been on the influence of the functionalization density on the load transfer at the nanoscale interface.

As an important engineering material, Epon 862/DETDA epoxy polymer,a thermoset plastic, has also been used as the polymer matrix material in order to see the difference in interfacial load transfer between a network structured polymer and the amorphous entangled structure of the PE matrix. As for thermoset epoxy polymer, emphasis has been put on investigating the effects of the crosslink density of the epoxy network on the interfacial load transfer ability for both non-functionalized and functionalized CNT-Epoxy interface at different temperatures(100K and 300K) and on the functionalization effect influenceing the interfacial interactions at the functionalized CNT-Epoxy interface.

Cohesive zone traction-displacement laws are developed based on the force-separation responses obtained from the MD simulations for both non-functionalied and functionalized CNT-PE/epoxy interfaces. Using the cohesive zone laws, the influence of the interface on the effective elastic material properties of the nanocomposites are observed and determined in continuum level models using analytic and computational micromechanics approaches,

allowing for the assessment of the improvement in reinforcement efficiency of CNTs due to the functionalization. It is found that the inclusion of the nanoscale interface in place of the perfectly bonded interface results in effective elastic properties which are dependent on the applied strain and temperature in accordance with the interface sensitivity to those effects, and which are significantly diminished from those obtained under the perfect interface assumption for non-functionalized nanocomposites. Better reinforcement efficiency of CNTs are also observed for the nanocomposites with the functionalized interface between CNTs and polymer matrix, which results in large increasing for the effective elastic material properties relative to the non-functionalized nanocomposites with pristine CNTs. Such observations indicates that trough controlling the degree of functionalization, i.e. the number and distribution of covalent bonds between the embedded CNTs and the enveloping polymer, one can tailor to some degree the interfacial load transfer and hence, the effective mechanical properties.

The multiscale model developed in this study bridges the atomistic modeling and micromechanics approaches with cohesive zone models, which demonstrates to deepen the understanding of the nanoscale load transfer mechanism at the interface and its effects on the effective mechanical properties of the nanocomposites. It is anticipated that the results can offer insights about how to engineer the interface and improve the design of nanocomposites.

This work received support provided by the Army Materials Center of Excellence (MCOE) Multilayered Technologies for Armored Structures and Composites (MultiTASC) under Agreement No:W911NF-06-2-0014 and the support provided by AFOSR grant FA9550-12-1-

0205 inthe Multi-Scale Structural Mechanics and Prognosis Program.

Dedication

This dissertation is dedicated to my beloved family.

Acknowledgments

It would not have been possible to complete this doctoral dissertation without the help and support of the kind people around me, to only some of whom it is possible to give particular mention here.

Foremost, I would like to express my deepest appreciation and gratitude to my advisor, Dr. Gary D. Seidel, for his patience, motivation, enthusiasm, and immense knowledge and providing me with the continuous support of my Ph.D study and research. His excellent guidance helped me throughout my time at Virginia Tech. I am truly fortunate to have had the opportunity to work with him.

I would like to thank the rest of my dissertation committee: Dr. Romesh C. Batra, Dr. Rakesh K. Kapania, and Mayuresh J. Patil, for their friendly guidance and thought provoking suggestions.

My sincere thanks also goes to all members in our research group, Dr. Xiang Ren, Skylar Stephens, Adarsh Chaurasia, Naveen Prakash and Engin Sengezer for their valuable help throughout my studies. Also I would like to thank all my friends in Blacksburg for all the

supports they gave and the fun we have had in the past five years.

Last but not the least, I would like to thank my mother who is always there for me.

Contents

List of Figures

List of Tables

Chapter 1

Introduction

1.1 Carbon Nanotubes

Since first reported by Iijima in 1991, carbon nanotubes (CNT) have been one of the hottest research topics because of their exceptionally high stiffness, strength, flexibility as well as superior electrical and thermal properties([1, 2, 3, 4, 5]). CNTs consist of covalently bonded carbon atoms in a long cylinder shape. The two basic types of CNTs are sinlge-wall carbon nanotube (SWCNT) and multiwall carbon nanotube (MWCNT). SWCNT is considered as a single graphene sheet(i.e a single layer of graphite) rolled into a tube at a certain chiral angle ([6]). MWCNT can be similarly considered as SWCNTs stacking with interlayer separations of around 0.34 nm around the hollow core of the innermost layer ([7]). The density of SWCNT is about 1.33-1.4 g/cm^3, which is smaller than the density of most of nanofillers

and just one-half of the density of aluminum ([8]). CNTs are reported to have an axial tensile modulus in the range of 300 to 1200 GPa (comparable to that of diamond (1.2 TPa)) and axial strength in the range of 10 to 150 GPa (higher than that of high-strength steel (2 GPa)) ([8]). With the radius on the order of the nanometers and length on the order of micrometers, CNTs possess high aspect ratios which are beneficial to their use in composites. In addition to superior mechanical properties, SWCNTs exhibit high thermal conductivity ($> 6000W/(mK)$) at room temperature, which is nearly double the thermal conductivity of diamond of 3320 $W/(mK)$ ([8]). SWCNTs can be either metallic or semi-conduction depending on the chirality of the tubes as indicated by the orientation of the carbon atoms around the nanotube circumference ([6]). The three common classifications are arm chair (which are conducting), zigzag (which are semiconduction)and chiral (which can be either semi-conducting or conducting). It is thus envisioned that CNTs can improve both the mechanical as well as the thermal and electrical properties of materials in which they are embedded making them multifunctional materials.

1.2 CNT-reinforced Nanocomposites

Much interest exists in reinforcing polymer materials using CNTs to gain the improvements in the mechanical, thermal and electrical properties. As these are expected to be achieved with minimum weight penalty given the CNTs and polymers have similar densities [9], such multifunctional improvements in properties are envisioned to be extremely beneficial for the

aerospace structures. With the unique combination of the physical, mechanical, electrical and thermal properties, CNTs are considered as promising candidates to perhaps even substitute for conventional micro-scale filler material while imparting multifunctionality to composites wherein they are a constituent.

A sizable body of work is available in the literature reporting efforts to fabricate and characterize polymer nanocomposites based on SWCNTs and MWCNTs in an effort to take advantage of their exceptional high stiffness, strength, superior electrical and thermal properties. For example, in [10] authors obtained the increases in Young's modulus and hardness by factors of 1.8 and 1.6 for poly(vinyl alcohol)(PVA)/MWNTs nanocomposites at 1 wt.% and 2.8 and 2.0 for Poly(9-vinyl carbazole)(PVK)/MWNTs at 8 wt.%. In [11] the authors dispersed MWNTs homogeneously throughout polystyrene matrices by a simple solution-evaporation method. Increases in the range of 36% to 42% for the elastic modulus of the nanocomposites were observed with just 1 wt% addition of CNTs. They also noted that 5 vol% of carbon fibers is needed to increase the polypropylene matrix moduli by the same extent observed in 1 wt% MWNT samples based on results in [12]. In [13] the authors investigated properties of low density polyethylene (LDPE) composites reinforced by MWNTs and reported 89% and 56% increases in the Young's modulus and tensile strength of the composites with 10 wt% CNTs loading, respectively. In [14] the authors reinforced high density polyethylene (HDPE) based composites using CNTs at 0.11, 0.22, 0.33 and 0.44 % volume fraction. It was noted that with increases in the volume fraction of CNTs, a considerable improvement was achieved in Young's modulus from 1.169 GPa (6.74% increasing) to 1.338

GPa (22.23%), and in the strength from 105.51 MPa to 109.86 MPa. Glassy and rubbery epoxy-matrix composites were processed in [15] with the addition of SWCNTs, MWCNTs, graphite and carbon nanofibers (CNTs) at 1 or 4 wt.%. For the composites with the glassy or rubbery matrix, 4% SWCNT/epoxy exhibited approximately the highest tensile modulus increasing by about 11% and 134% in the glassy and rubbery phases, respectively. In [16] the authors reinforced an epoxy matrix using 0.1 wt.% addition of CNTs with variable lengths ranging from 503 to 2091 nm. It was found that nanocomposites containing long carbon nanotubes (2091 and 1689 nm) exhibited better mechanical properties(higher tensile strength (13-25%), elastic modulus (5-20%), fracture strain and toughness(30-45%)) than those containing short carbon nanotubes (1332, 992 and 503 nm).

While the CNT-reinforced polymer nanocomposites exhibit promising increases in the mechanical properties relative to pure polymer material, the experimental results do not meet expectations and typically remain far behind the idealized theoretical predictions obtained from the rule of mixtures and Halpin-Tsai models ([13, 17, 14]). For example, in [13] the authors observed increases in the tensile modulus of CNT-PE nanocomposties from 0.235 GPa to 0.261 GPa with the addition of 1 wt.%, i.e. 11% increase over the neat PE value, however the rule of mixtures would predict the modulus to be 1.23 GPa at this loading of CNTs (assuming well dispersed and the modulus of MWNTs is 1 TPa). Significant effort has been dedicated toward experimentally identifying critical conditions for fabricating CNT-reinforced nanocomposites able to match the theoretical expected mechanical performance. Although CNTs themselves possess extremely high mechanical properties, how to transfer

their properties to the nanocomposites and produce a better macroscale effective material properties remain an issue. In addition to the properties of the individual constituents, several factors have been identified to be critical for the mechanical performance of the CNT-reinforced nanocomposites, such as the alignment and the dispersion of the CNTs as well as the interface between the CNTs and matrix material. In [18] the authors fabricated linear low density polyethylene (LLDPE) matrix composites reinforced by 2 wt% MWNTs through an extrusion process to achieve a degree of alignment of the CNTs. The composites panels were formed by stacking the extruded filaments into layers in a unidirectional fashion and tested under tension in the longitudinal as well as the transverse directions relative to the extrusion direction. The tensile strength and modulus of the composites was observed to increase by about 34 and 38 % in longitudinal directions, but decreased by about 20.2 and 9.47 % in the transverse direction relative to the neat LLDPE thereby demonstrating the alignment of nanotubes in the composites and their reinforcement effects along the extrusion direction. Methods have been proposed to achieve better dispersion of CNTs in the nanocomposites, e.g. ultrasonication, solution mixing of a suspension of CNTs in dissolved polymer, mechanical blending of CNTs and melted polymers and in situ polymerization of monomers with CNTs [8, 19, 20, 21, 22]. In [23] the authors prepared MWCNT/HDPE composites by using immobilized catalyst and reported greatly enhanced mechanical properties, 359% and 281% increases in the Young's modulus with respect to the reference PE and mechanically blended MWCNT/PE composite, respectively, which were believed to be attributed to the better dispersion of CNTs.

Given their large surface area to volume ratio, the interfacial interaction is a crucial issue governing the effective material properties of CNT/polymer nanocomposites [24]. From the processing point of view, the surface modification of the CNTs assists their exfoliation from CNT bundles to individual CNTs by offering repulsive forces between tubes which helps to uniformly disperse them in a polymer matrix in order to maximize the contact surface with the matrix [25]. In addition to governing dispersion, the interface between the CNTs and the polymer matrix is widely believed to be a significant factor affecting the load transfer from the matrix to CNTs, which is critical to fully take advantage of the superb properties of CNTs, and thereby directly impacts nanocomposites mechanical properties [26]. Without proper treatments of the interface, poor load transfer between the polymer matrix and C-NTs has been observed to impact the macroscale mechanical properties of the CNT-polymer nanocomposites resulting in the large difference between the theoretical predictions and the experimental results [27, 28, 29]. In order to fully exploit the reinforcement ability of CNTs in the CNT-polymer nanocomposites, it is critical to improve CNT-polymer interfacial properties, i.e. the efficiency of load transfer at the interface between CNTs and the polymer matrix. As such, increasing interests exist in research on techniques of engineering the interface to achieve better load-transfer properties ([30, 31, 32]). Functionalization of the surface of CNTs includes noncovalent and covalent methods. Noncovalent methods include wrapping polymer chains around CNTs or attaching various surfactants to the surface of CNTs such that only non-covalent bonding interactions occur between the modification molecules and CNT. One example of introducing a surfactant as the wetting agent is discussed in

[33] wherein it is demonstrated that about a 26% increasing in mechanical properties of the nanocomposites is achieved with only 1 wt.% addition of CNTs as opposed to an 11% increase without the surfactant (both with respect to the neat polymer). In covalent methods of surface functionalization, covalent chemical bonds are formed between the polymer chains and CNTs in order to enhance the interfacial strength. In [34] the authors fabricated polymer-MWNTs composite films using PVA or polypropylene as the matrix. In the former case having PVA matrix, increases in Young's modulus, tensile strength and toughness were observed to be 3.7, 4.3 and 1.7 times, respectively, for the nanocomposites with less than 1 wt.% non-functionalized CNTs (i.e. only non-covalent interaction). Crystalline coating of PVA was noted around the nanotubes in this case, which can be viewed as an interphase region and is believed to contribute to the improvement of the mechanical properties. In the latter case, covalent fuctionalization of the CNTs is used in order to achieve better dispersions in chlorinated polypropylene. Increases in Young's modulus, tensile strength and toughness of 3.1, 3.9 and 4.4, respectively, compared to the non-functionalized nanocomposites values were observed at 1 wt.% nanotube loading levels equivalent to the former case. Amino-functionalization of CNTs has been applied as a covalent means of improved load transfer in CNT-epoxy polymer nanocomposites in [30]. There it is reported that a better dispersion and integration of CNTs in the polymer matrix is achieved resulting in remarkable improvement in mechanical properties, e.g. 24.6% increase in the elastic modulus with only 0.5 wt% addition of functionalized CNTs in contrast to only 3.2% increases over the neat polymer value with non-functionalized CNT. In [35] the authors fabricated epoxy-based

nanocomposites reinforced by CNTs with covalently attached amino groups which allowed for the ful integration of CNTs into the nanocomposites as the amino group grafted on the surface can react with the epon resin in the polymer matrix. They reported 30-70% increase in ultimate strength and modulus of the nanocomposites with 1-4 wt% functionalized SWNTs along with an increased strain to failure.

In order to understand and study the interactions between CNTs and polymer, efforts have been made to experimentally characterize the interface in CNT-based nanocomposites. Load transfer properties of nanocomposites with different matrix materials reinforced by CNTs have been evaluated using atomic force microscope (AFM), transmission electron microscope (TEM)/nano-manipulation system (NMS) or Raman spectrum measurement [31, 36, 37]. The load transfer in CNT/epoxy nanocomposites with/without functionalization is evaluated in [31] based on strain-sensitive Raman spectroscopy. Improved load transfer efficiency is reported by the authors for functionalized CNT/epoxy nanocomposites based on the observation of higher initial G'-band slope and higher strain corresponding to the shift of G'-band. However, as these are indirect measurements of the CNT-polymer interaction, no quantitative information was given as to the magnitude of the interfacial strength. In [36] and [37] the authors measured the interfacial shear strength of CNT-dispersed polymer nanocomposites using AFM and reported 47Mpa for MWNT/polyethylene-butene nanocomposites and 3.7-14Mpa for CNT/PEEK nanocomposites, respectively. However, only a few experiments on direct exploration of the load transfer capability of the CNT-polymer interface in nanocomposites have been reported and the results exhibit wide variations [37] due to the

reasons as concluded in [38] such as "(i) the lack of proper direct measuring techniques at the nanometer scale; (ii) tremendous limitations on the specimen size; (iii) an uncertainty in the data obtained from indirect measurements; (iv) inadequate preparation techniques of test specimens and the lack of control over the alignment and distribution of nanotubes." Therefore, computational material science techniques and multiscale modeling techniques are beginning to play a key roll in more systematically investigation of the tailoring of interfacial strength at the nanoscale and its corresponding influence on the macroscale mechanical properties of the CNT-reinforced nanocomposites.

1.3 Nanocomposite Modeling

Given the potential applications across a widely range of industries, there is a need to develop models to predict the mechanical, thermal and electrical properties of the nanocomposites for design efforts. A significant amount of effort has been dedicated in particular towards analytical and numerical studies of the mechanical properties of the CNT-based nanocomposites. One of the key challenges is that nanocomposite properties are governed by features which exist in and interact across a wide range of length scales, from the discrete atomistic nanometer scale through continuum micro, meso, and macroscales. In this section, current theories and models are reviewed for addressing material behavior of nanocomposites at the various length scales.

Many efforts have been dedicated towards analytical and numerical studies of the mechan-

ical properties of the CNT-based nanocomposites using continuum models. In [39, 40] the authors modeled CNT/polymer nanocomposite using cylindrical, square and hexagonal representative volume elements (RVEs), including single short/long CNTs or multiple aligned CNTs to predict the elastic mechanical properties of nanocomposites using continuum finite element analysis. Increase of the stiffness of the composites at a volume fraction of 3.6% in the CNT axial direction was found to be as much as 33% for the case of infinitely long CNTs, i.e. CNTs which extend the full length of the RVEs used. A large microscale continuum model with short/long rigid aligned fibers was applied in [41] to model CNT-based nanocomposites. The effective elastic mechanical material properties of the nanocomposites were calculated by solving the boundary integral equations using a fast multipole boundary element method. There it was observed that better reinforcement (i.e. larger increases in elastic properties) were obtained using long CNTs in the nanocomposite. As some of the very first works for predicting the properties of nanocomposites, perfect bonding assumptions are made in these continuum models without considering the effects of interphase or interface regions between CNTs and polymer matrix in nanocomposites. In [42] and [43] the authors have studied the effective elastic properties of carbon nanotube reinforced composites and discussed the influence of the alignment, clustering, and the presence of an interphase region using both finite element method (FEM) and composite cylinders model (CCM) micromechanics techniques. The interphase is a finite thickness region surrounding the CNT where the local polymer morphology has been perturbed by the CNT presence [44]. In contrast, the interface is a zero thickness region representing atomic forces responsible for load transfer

between the CNT and polymer. The influence of the interphase with prescribed material properties is investigated as the third phase in the FEM and CCM models based on continuum mechanics. The calculated moduli match well with the experimental moduli for CNT reinforced nanocomposites with fairly low volume fractions, but overpredict the observed experimental values when the volume fraction of CNTs was increased.

Because CNT/polymer nanocomposites consists of polymer molecules and CNTs both of which have dimensions at the nanoscale, their interactions with each other may highly depend on the local morphologies at the interface. Efforts have been made to model and characterize the CNT/polymer nanocomposites using molecular dynamic (MD) /molecular mechanics (MM) simulations to investigate the influence of atomistic details on the continuum properties of nanocomposites. In [45] the authors have studied and reported the stress-strain behaviors of CNT-polymer nanocomposites with short and continuous CNTs in a PE matrix using MD simulation. MD was also used in [46] to calculate the Young's modulus of single-wall nanotube (SWCNT)-PE nanocomposites (SWNT volume fraction of 2%), where it was observed that the nanocomposites did not show significant enhancement relative to pure PE system. In [47] assassination has been made for the thermal and mechanical properties of DGEBA/44DDS epoxy system with/without the addition of CNTs based on the stress-strain relations calculated using atomistic modeling and MD simulations. A moderate increase around 18% was observed for the elastic modulus of the DGEBA/44DDS epoxy resin by adding 11.8 wt.% of SWCNTs. However, it is still controversial to estimate the bulk material properties using the virial stress at the nanoscale because of arguments

about the equivalence of the virial stress and Cauchy stress [48]. In [49] the authors compared the tensile response and fracture of CNT-based nanocomposites with crystalline and amorphous PE using MM simulations and observed that the increase in strength is larger by reinforcing an amorphous PE matrix with a through CNT, which also encompasses the interface effects, but neglects the influence of the temperature. The mechanical performance of nanocomposites reinforced by the pristine or functionalized CNTs were studied in [50] using MD simulations. A huge increase (around 50%) in the Young's modulus was observed for the nanocomposites using the functionalized CNTs as the filler as oppose to the unchanged mechanical properties of the nanocomposites with the pristine CNTs as compared to the neat crosslinked epoxy. Such observations demonstrate the significant role of the interface in the enhancement of mechanical properties in nanocomposites. While atomistic simulations are able to include both non-covalent and covalent interfacial interactions between CNTs and the polymer matrix in the study of nanocomposites, however pure atomistic studies are in general limited in the size of the representative volume elements (RVEs) and the length of simulation time, i.e the number and aspect ratio of CNTs included in the simulation system. Among the few studies towards combing nanoscale and microscale modeling, an approach linking the nanoscale structure and the macroscale properties was developed in [51, 52]. Therein the idea of an effective continuum fiber is proposed to model the nanotube, the polymer near the nanotube and the interface between them based the atomistic simulations, i.e. homogenizing the interface and interphase along with the CNT into an effective nanofiber. The effective nanofiber then serves as a link between this so called

equivalent-continuum and micromechanics models to predict the bulk material properties of SWCNT/polyimide composite systems wherein the micromechanics RVEs can have multiple CNTs with multiple orientations, e.g. randomly oriented, can be considered in simulations on continuum time scales. Here again, the comparison with the experimental data is good for low volume fraction nanocomposites (e.g. less than 0.2%). It is noted, however, that the equivalent-truss model applied in the equivalent-continuum modeling does not retain the effect of the temperature on the interface, and that the homogenization of the effective fiber does not retain the sensitivity of the interface on the applied load.

In the experimental and computational modeling studies, it has been observed that interface not only affects the dispersion of CNTs, but also influences the macroscale effective material by dictating load transfer efficiency and thereby governs the overall mechanical performance of the nanocomposites. Given the challenges associated with directly probing materials at the nanoscale, there is increasing interest in and reliance on computational materials science techniques to characterize the interface between the CNTs and polymer matrix using the continuum models and atomistic simulation [53, 54, 55]. In analytical studies, most of work has tried to apply microscale rules developed for microscale fibers in traditonal composites towards predicting nanocomposites properties [53, 56]. In [53] the authors calculated the interfacial shear strength in CNT-polymer nanocomposites by using the extended Kelly-Tyson model and reported that the interface may be stronger than the bulk polymer in terms of sustaining shear. However, microscale modeling assumptions may not be valid when directly applied to nanoscale structures due to the assumptions like perfect bonding. As the interface

and interphase region involve the polymer chains in the very near vicinity (around 3 nm) of CNTs, the CNTs interact with the surrounding polymers mainly through vdW forces, which allows for sliding and debonding of CNTs with respect to the matrix material under variable loading conditions. In [57] effort has been made to include the vdW interactions in their model by directly fitting vdW potential to a cohesive zone model and study the interfacial shear stress by conducing pullout tests. When implemented within the finite element method (FEM), cohesive zone models are able to simulate interface debonding and sliding in the composites, however it is difficult to obtain physically meaningful and accurate cohesive law parameters for the nanoscale interface from continuum studies. A cohesive law, describing the relation of the normal/shear traction and the opening/sliding displacement across the interface has been developed in [58] in terms of the area density of CNT and the volume density of polymer. However, continuum models are basically considering both the reinforcement and the matrix material as continuum bodies and are using assumptions about the interface developed for and applicable to microscale continuum fibers. However, by ignoring the atomistic details of CNTs and the polymer, the continuum modeling is not able to observe and characterize the atomistic morphology at the interface around CNTs, and more importantly, how it evolves under load. As it is believed that the behavior of the interface is highly dependent on the local atomistic configuration, MD simulations are therefore better suited in capturing the detailed information about the load transfer at the interface than the continuum models. Applying MD towards understanding nanoscale load transfer, in [55] and [46] the authors conducted pullout tests of CNTs in polymer matrix using MD simulations

and reported interfacial shear strengths up to 75 MPa for SWCNT-epoxy resin nanocomposites and to around 141.40 MPa for SWCNT-PE nanocomposites. In [54] comparison has been done for the behavior of polymer-nanotube interface with non-bonded interaction to the interface with chemical bonds between the nanotube and matrix, and concluded that the shear strength can be increased for the polymer-nanotube interface by introduction of a low density of covalent bonds between the matrix and nanotubes. However, those studies researched and reported only the shear strength, which gives only one mode (i.e. sliding mode) of interface load transfer. To consider a range of loading conditions, it is important to know the response of the interface under normal mode separation as well. The separations in both normal and sliding directions were studied in [59] for the non-functionalized interface in CNT-PE nanocomposites using MD simulations in an effort to characterize the load transfer only associated with vdW interactions and observed that the normal separation response was significantly stronger than the sliding mode. It is therefore expected that the functionalized interface, which in addition to the non-boned vdW interactions has covalent bond interactions that are associated with the grafting of the functional groups between CNTs and the polymer matrix, would therefore demonstrate even greater enhancement of the normal mode response so that when combined with the observed functionalized sliding mode response from the pullout test, the overall strength and load transfer ability of the interface in the nanocomposite would be significantly improved.

1.4 Objectives and Outline of the Present Research

In the present work a multiscale modeling approach is proposed for assessing the effects of the non-functionalized and functionalized interface between the CNTs and a polymer matrix in nanocomposites. At the smallest length scale, force field based atomistic MD simulations are used to assess the interface force-separation response following the approach employed by Awasthi et al. [59]. The force-separation response is then mapped into a cohesive law used to describe the interface load transfer in larger length scale continuum micromechanics studies. This hierarchical approach allows for off-line MD simulations to provide relevant atomistic temperature dependent interfacial load transfer information to continuum simulations which can use larger RVEs and time scales in determining effective elastic properties. Special emphasis is placed on assessing MD interface RVE characteristics in determining a converged set of cohesive zone parameters. Opening mode and sliding mode separations of the CNT-polymer interface model have been performed using MD at a given temperature for the interface in order to obtain the force-separation responses of the graphene sheet. s based on peak traction and the energy of separation for non-functionalized and functionalized interface have been embedded in the next level analytic and computational micromechanics models to construct a multiscale model for exploring the bulk mechanical properties of the nanocomposites.

Two different material systems, CNT-PE and CNT-Epoxy nanocomposites, are studied. For the thermoplastic CNT-PE nanocomposites, parametric studies are conducted in terms of

the number and the length of polymer chains, and the 'grip' position in order to obtain the suitable size of the representative interface elements at the nanoscale. The interface between PE and CNTs at different temperatures are characterized in normal opening mode separation. For the thermoset polymer epoxy (Epon 862/DETDA), algorithms for the cross-linking process are developed to prepare the atomistic structures of the epoxy with variable cross-linking densities. Simulations are performed to explore the influence of cross-linking density and the temperature on the load transfer across the interface of CNT-Epoxy nanocomposites in terms of the force-separation response.

In the aforementioned experimental studies, treatments of the CNT surface have been explored to improve the load transfer at the interface. It was observed and reported that the functionalized CNT-polymer nanocomposites exhibited better mechanical material properties in both experimental and modeling research. To understand the mechanisms behind the improvement of interfacial strength, atomistic functionalized representative interface elements are built for both CNT-PE and CNT-Epoxy material system with variable functionalization densities. Normal mode separations are simulated at different temperatures to produce force-separation responses using MD techniques in order to evaluate the efficiency of the load transfer across the interface with variable numbers of functional groups at the nanoscale.

At the microscale, cohesive zone models are implemented in the composite cylinder method and in finite element analysis to estimate the effects of the interface between CNTs and the polymer on the macroscale effective material properties. Cohesive zone laws are developed

to describe the sliding and debonding of the interface in variable loading conditions based on continuum traction-separation laws which are obtained by averaging the force-separation response over the area of graphene sheet from MD simulations. In assessing the influence of the interface on the effective elastic material properties, the stiffness components of the CNT-polymer nanocomposites are calculated by solving the boundary value problems assuming perfect bonded interface or considering the interface by applying the developed cohesive zone laws.

This work is presented as follows. Chapter II provides a overview of MD simulation techniques and cohesive zone models. Chapter III provides the atomistic modeling of the non-functionalized thermoplastic graphene interface and continuum modeling of the CNT-PE nanocomposites using cohesive zone model embedded CCM and FEM . The nanoscale load transfer of the graphene-PE interface is characterized using MD simulations to develop the cohesive zone laws, which are transferred to the higher level micromechanics model to include the nanoscale interface information in the study of the effective mechanical properties of the nanocomposties. This contributes towards the understanding of the influence of the nanoscale interface effects on the macroscale effective mechanical properties of the CNT-PE nanocomposites with non-functionalized interface. Chapter IV provides the atomistic modeling of the functionalized thermoplastic graphene interface and continuum modeling of the functionalized CNT-PE nanocomposite using FEM combined with cohesive zone models. Results about the load transfer ability of the functionalized graphene-PE interface and the effective mechanical properties of the CNT-PE nanocomposites are provided to illustrate the

effects of functionalization at the nanoscale and microscale. Chapter V discussed the atomistic modeling of the non-functionalized and functionalized thermoset graphene interface. A dynamic crosslinking algorithm is provided to prepare the thermoset polymer material with different crosslink densities. Discussion about parameters impacting the nanoscale load transfer ability of the non-functionalized and functionalized thermoset graphene interface is provided, leading to observations on the influence of functionalization on the macroscale effective material performance of the CNT-epoxy nanocomposites.

Chapter 2

Modeling techniques

2.1 Molecular dynamics simulations

Molecular dynamics is a computer simulation technique for simulating the movements of atoms and molecules in the context of an N-body atomistic system. In most cases, the particles in molecular dynamics simulations are treated as point masses which interact through a set of force fields described by potential functions. Choosing a proper force potential for the given system is the critical first step for MD simulations. The choice depends on the type of material system and the process that is of interest. After the force field potential is chosen, the initial configuration of the simulation system needs to be established by assigning every particle spacial positions, a coordination and a velocity. Given the boundary conditions, the trajectories of atoms and molecules inside the simulation system can be calculated for a

period of time by numerically integrating Newton's equations of motion. Periodic boundary conditions are usually applied in certain dimensions, which allows the representative volume elements to be repeated in certain directions for representing large (infinite) systems.

2.1.1 Force Field Potentials

A force field potential is based on parameters determined by fitting the results from experiments or ab-initio calculations. There are classical and reactive force fields. Classical force fields are parameterized to describe the structures and energies close to equilibrium. No bond breaking nor creating are allowed in classic force fields.

The consistent Valence Force Field (CVFF) potential [60] employed in the present study is a classical force field that is properly calibrated for the carbon-carbon and carbon-hydrogen interactions. It consists of four energy components, bond stretching, angle bending, torsion and non-bonded potential.

To overcome the limitation of classical force fields, reactive force fields are developed which include bond breaking and creating during the simulation without performing computationally intensive quantum mechanics calculations. The Tersoff Brenner potential, the Reactive Empirical Bond Order (REBO) and the Adaptive Intermolecular REBO (AIREBO) potential proposed are commonly used reactive force fields [61, 62, 63]. AIREBO, proposed by Stuart and Harrison is a further development of the reactive empirical bond-order (REBO) potential of Brenner, which in turn is based on the Tersoff Brenner potential. As it is pa-

rameterized for modeling condensed-phase hydrocarbon systems and the breaking and the formation of chemical bonds, the AIREBO potential is adopted for some cases studied here. It includes three energy components, the REBO potential, a torsional interaction potential and an intermolecular interaction potential. The REBO potential uses a Tersoff-style potential to treat the covalent bonding interaction and depends not only on the distance between atoms, but also on their local atomic environment by using a parameterized bond order function. The AIREBO potential has been used in the current study for simulating the functionalized interfacial system with the thermoplastic PE matrix.

Optimized potentials for liquid simulations (OPLS) All-Atom(AA) force field, which was developed by Jorgensen and coworkers [64] based on the Assisted Model Building and Energy Refinement(AMBER) potential for the organic molecules, was used to simulate the intra and intermolecular forces in the interfacial system within the thermoset epoxy polymer and is a classical force field potential like CVFF. OPLS AA potential consists of four energy parts including bond stretching, angle bending, torsion and non-bonded interactions.

As the AIREBO potential is computational expensive to use, the CVFF and OPLS potentials are modified by including strain energy failure criteria to allow for bond breaking, and are then applied to characterize the load transfer ability of the functionalized graphene-polymer interface.

2.1.2 Ensembles

There are generally four types of simulation conditions considered in MD simulations referred to as ensembles.

The canonical ensemble (NVT ensemble) has the number of particles (N), temperature (T) and volume (V) conserved, and is known as constant temperature molecular dynamics. In this ensemble, the simulation system has thermal contact with a large heat bath, which allows for the addition and/or removal of energy from the MD simulation in an realistic way.

The isothermal-Isobaric ensemble (NPT ensemble) has the number of particles (N), pressure (P) and temperature (T) conserved in the simulation system. Both a thermostat and barostat are applied in this ensemble. The volume of the system is allowed to change freely with the change of temperature and pressure. This ensemble is widely used in MD simulations as most real experiments are carried out under conditions of controlled temperature and pressure.

The microcanonical ensemble (NVE ensemble) has the number of particles (N), volume (V) and energy (E) conserved. This ensemble simulates an isolated system where there is no heat exchange.

The isoenthalpic-Isobaric ensemble (NPH ensemble) has the number of particles (N), pressure (P) and enthalpy (H) conserved. Because $H = E+PV$, the internal energy E and the kinetic energy PV are allowed to change proportionally, thus indicating that the volume is also a dynamic variable.

NVT ensemble is used in this study to achieve temperature control in MD simulations.

NPT ensemble is used to prepare the polymer matrix with realistic densities under a certain temperature and atmosphere pressure.

2.2 Cohesive zone model

In the study of failure behavior, may engineering materials exhibit some ductility after reaching the strength limits. If the small zone in the front of the crack tip termed as the failure process zone where small-scale yielding, microcracking and void initiation, growth and coalescence are observed is not sufficiently small relative to the structural dimensions, the linear elastic fracture mechanics does not apply and the failure process zone is not negligible. As first introduced by Dugdale and Barenblatt [65, 66], cohesive zone model have been widely used to investigate the failure process in materials and structures [67, 68], such as imperfect interfaces and crack propagation, by having the basic idea to lift the limitation of small scale yielding beyond the crack tip and eliminate the singularity of stress in front of the crack tip usually associated with classical linear elastic fracture mechanics. Another reason for the widespread use of cohesive zone models is that it is easy to incorporate cohesive zone models in various computational methods.

In cohesive zone models, the assumed crack propagation path in front of the actual crack tip has the upper and lower surface idealized as cohesive zones with vanishing thickness which are assumed to support traction in both normal and tangential directions relative to the surface normal vector. The cohesive traction-displacement laws across the crack propaga-

tion plane are used to describe the mechanical behavior of the cohesive zones which relates the surface traction to the relative separation displacement of the crack surface. While the crack propagates through the material, the failure process zone in the front of the crack tip is degraded by following the cohesive traction-displacement relationship and has a different constitution from the material surrounding it. Therefore it is observed that the form of cohesive zone laws is critical in predicting the mechanical response of the material. Various cohesive traction-displacement laws have been developed and studied for ductile and brittle materials in the literature [69]. In this study, bilinear and non-linear cohesive zone laws are developed to describe the response of the non-functionalized and functionalized interface between CNTs and the polymer matrix. As discussed in detail in the following chapter, the cohesive zone models are embedded in CCM and FEA to investigate the macroscale effective elastic mechanical properties of the CNT-polymer nanocomposites under the nanoscale interface effects.

Chapter 3

The effects of the non-functionalized interface in the CNT-PE nanocomposites on the bulk effective material properties

3.1 CVFF potential

To model the CNT-PE interface at the nanoscale, CVFF potential is applied to simulate the interactions between atoms in the interfacial system. CVFF is properly calibrated for the carbon-carbon and carbon-hydrogen interactions and consists of four energy components

which are associated with bond stretching, angle bending, torsion and non-bonded potential associated with van der Waals interaction.

The total potential energy of the system associated with bond stretching is a two body potential which models the change of the distance between two covalently bonded atoms and is given by:

$$E_b = \sum_{i=1}^{n} K_b^i (r^i - r_0^i)^2 \tag{3.1}$$

where r^i represents the distance between two atoms in i^{th} covalent bond, r_0^i represents the equilibrium distance between the two atoms in i^{th} covalent bond, K_b^i is the stiffness of i^{th} covalent bond and n is the number of the covalent bonds in the system.

As certain covalently bonded molecular structures have preferred angles, e.g. the 120 degree angle in the hexagonal arrangement of graphene, the total potential energy of the system associated with the change of these angle is obtained from a three body is given by:

$$E_a = \sum_{i=1}^{n} K_\theta^i (\theta^i - \theta_0^i)^2 \tag{3.2}$$

where θ^i represents the angle for i^{th} pair of adjacent covalent bonds, θ_0^i represents the equilibrium angle for i^{th} pair of adjacent covalent bonds, K_θ^i is the angle stiffness of the angle for the i^{th} pair of the adjacent covalent bond and n is the number of the preferred bond angles in the system.

As different bonds, such as single and double bonds, possess different torsional barriers, the total potential energy associated with torsional interaction captures the energy of the angle formed by four atoms covalently bonded, which is also known as dihedrals, and is:

$$E_t = \sum_{i=1}^{n} K_\phi^i [1 + d^i \cos(m^i(\phi^i - \phi_0^i))] \tag{3.3}$$

Where ϕ^i represents the i^{th} dihedral between two planes formed by two adjacent covalent bonds, ϕ_0^i represents the equilibrium dihedral, K_ϕ^i is the torsional stiffness of the i^{th} dihedral, d^i and n^i are the defined parameters for special atomic system, and n is the number of the dihedrals in the system.

Finally, the non-bonded pair potential component of CVFF considers the energy between non-covalently-bonded atoms which is typically recognized as the van der Waals interaction and results in a total potential energy for non-bonded interactions in the system as given by:

$$E_p = 4 \sum_{i=1, j \neq i}^{n} \varepsilon_{ij} [(\frac{\sigma_{ij}}{r_{ij}})^{12} - (\frac{\sigma_{ij}}{r_{ij}})^6] \qquad r < r_c \tag{3.4}$$

where ε_{ij} is the energy well depth for between the i^{th} and j^{th} atoms, r_{ij} is the distance between the i^{th} and j^{th} atoms, σ_{ij} is the equilibrium distance between i_{th} and j_{th} atom, n is the total number of the atoms in the system and r_c is the cutoff distance beyond which the force between the i^{th} and j^{th} atoms is ignored.

The total potential energy for the system at a given time step in the MD simulation is thus

obtained by summing the four components together:

$$E_{total} = E_b + E_a + E_t + E_p \tag{3.5}$$

The exact parameters of CVFF used in the present work are shown in table A.1.

3.2 Nanoscale representative interface element Philosophy and Computational Construction

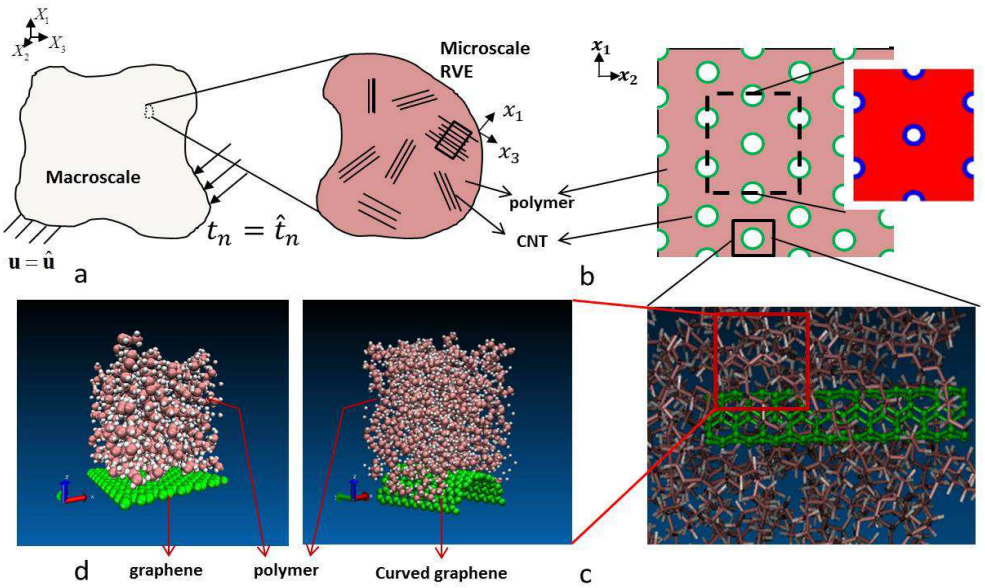

Figure 3.1: (a) shows the effective homogeneous nanocomposite material at the macroscale whose properties are based on key features of the nanocomposite microstructure such as dispersion of CNTs into randomly oriented bundles. (b) shows CNTs are aligned inside the bundle which is modeled using the microscale RVE with a hexagonal array of CNTs. (c) shows a CNT fully enveloped by the polymer matrix. (d) shows representative interface elements of equilibrated polymer-graphene with flat or curved graphene sheets.

The multiscale modeling strategy we proposed is described in figure 3.1 wherein the atomistic load transfer information at the interface of CNT-polymer nanocomposites is hierarchically transferred to continuum microscale RVEs. At the microscale, bundles of CNTs are dispersed into a polymer matrix randomly oriented as depicted in figure 3.1a. Inside the CNT bundles, locally aligned CNT segments([42]) are modeled using a microscale RVE with a hexagonal array of CNTs as in figure 3.1b. At the atomistic scale, it is expected that individual CNTs or a subset of the bundle along with the locally enveloping polymer can be modeled directly as shown in figure 3.1c. However, the size of the atomistic RVE is dependent on the computation resources available and is subject to atomistic time scales on the order of picoseconds. In our study, atomistic representative interface element in figure 3.1d are proposed which depicts the region inside the square in figure 3.1c, which enables us to study load transfer between CNT and the polymer matrix. The models as shown in figure 3.1d are comprised of a block of amorphous PE interacting with a graphene sheet to form a representative interface element for the CNT-PE nanocomposite system. The green sheets are graphene sheet above which is placed a film of amorphous PE represented by the pink carbon and white hydrogen atoms. The carbon-carbon and carbon-hydrogen interactions between carbon atoms and hydrogen atoms in the polymer and graphene sheet are all based on the same potential function, the consistent covalent force field (CVFF) ([60]), which is properly calibrated for the carbon-carbon, and carbon-hydrogen interactions. In figure 3.1d, flat and curved graphene sheets are adopted to represent the CNT for they have similar local morphology as CNTs are often viewed as graphene sheets rolled into a tube structure at certain chiral angles([70]

). Curvature effects were studied using the RVE in 3.1d with curved graphene sheets of variable radii in order to verify the use of flat graphene sheet representing CNTs of variable raduii. The interaction between the graphene and the polymer is captured using non-bonded potential as it has been assumed there are no bonds between the separate phases, i.e. the interface is not functionalized. To characterize the interface load transfer, the equilibrated representative interface element will be subjected to normal and sliding separation to obtain the force-separation responses.

3.2.1 Preparation of Amorphous Polymer

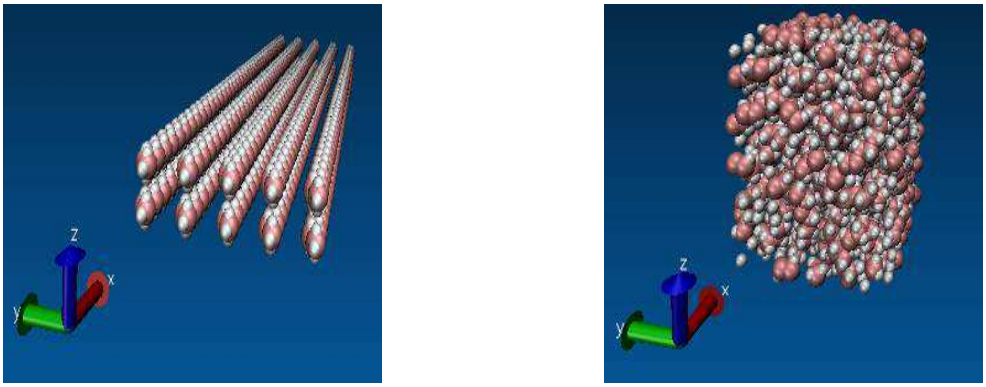

(a) Polymer Starting Structure (b) Polymer Final Configuration

Figure 3.2: Snapshots in the process of preparing amorphous PE structure with 10 polymer chains and 78 monomers in each chain(10c80c case): (a) starting structure in equilibration process for making amorphous polymer; (b) final configuration of amorphous polymer obtained from the equilibration process.

In order to capture the detailed information at the atomic scale, the fully atomistic structure of the polymer chain keeping information about the interactions between each single atoms was modeled in the present work, which is important for the load transfer study.

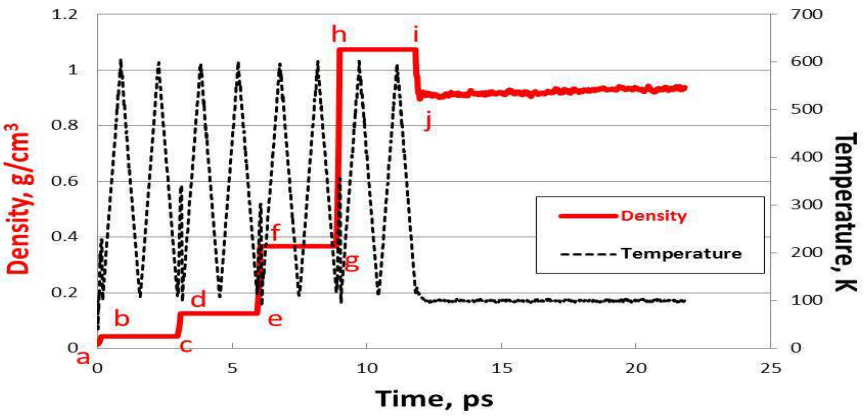

Figure 3.3: The change of the density of the amorphous polymer and the temperature of the simulation system with respect to time during the process used to obtain an equilibrated structure for the 10C80C system at 100K. a through j denote key steps in the procedure.

The monomer of PE has three atoms, one sp^3 hybridized carbon atom and two hydrogen atoms and is represented as $-CH_2-$. A long polymer chain is comprised of repeated $-CH_2-$ units which is capped by a $-CH_3$ unit at each of the two ends so that the PE chain can be expressed as $CH_3-(CH_2)_n-CH_3$. In the present work, the amorphous polymer models including differing numbers of polymer chains, m, with variable numbers of monomers, n, in each chain are constructed through an in-house FORTRAN code and explored in the interface model.

To obtain an equilibrium amorphous polymer structure at a given temperature and pressure, the methodology in the work of [71] has been adopted. Temperature annealing cycles and volume shrinkage steps are alternately applied to the MD polymer system causing the polymer model to undergo structural transitions. Dynamic equilibration of the model at the required temperature and pressure conditions is conducted for a sufficient amount of time

to obtain the equilibrated sample with stable density.

For the case with 10 polymer chains and 78 monomers (80 carbon atoms) in each chain, $CH_3 - (CH_2)_8 - CH_3$, the pictures of the starting structure and the final amorphous PE obtained are shown in figure 3.2 with the corresponding changes of density and temperature of the simulation system during the equilibration process in figure 3.3. A simple structure was produced as the initial configuration as seen in figure 3.2(a), which consists of aligned straight chains in the simulation box at fairly low density. The volume shrinkage of the simulation box is done four times under NVT ensemble keeping the temperature at required temperature(in this case 100 K) with the corresponding shrinkage segments denoted as a-b, c-d, e-f and g-h of the density curve in figure 3.3. The volume of the simulation box is reduced by shrinking all sides of the rectangular periodic box at constant rate. Between the volume shrinkage steps, two cycles of constant volume annealing are done by raising the temperature to 600K, which is far above the glass transition temperature (250K in [72]) for PE , and then back to the required temperature. The temperature annealing cycles are also shown in figure 3.3 where it is noted that no density changes are allowed to transpire during these annealing segments denoted as b-c, d-e, f-g and h-i . The annealing process is used to put energy into the simulation box associated with the increase in temperature in order to overcome any barriers associated with local energy minima so that the global energy minima of the amorphous polymer is achieved. After the volume shrinkage and temperature annealing cycles have completed under the NVT ensemble, the system is switched to an NPT ensemble for final dynamic equilibration in order to obtain a final amorphous structure at

the desired temperature and pressure (1 atm). It is noted from figure 3.3 that the final NVT volume shrinkage step raises the density to a value which is a little greater than 1 g/cm^3, and that the subsequent switch to the NPT ensemble relaxes the structure to a final density of 0.94 g/cm^3 which is within the range of experimental values 0.88 to 1.6 g/cm^3 for PE density.

3.2.2 Equilibration of Non-functionalized Interface Model

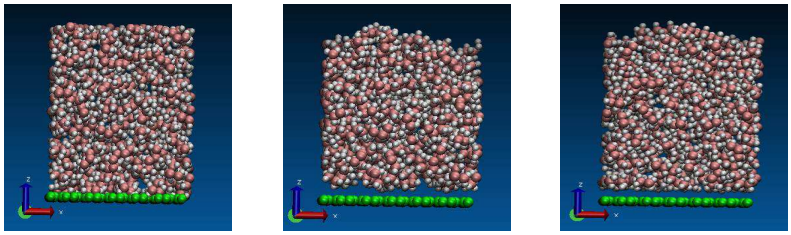

(a) Interface Introduction (b) 0K Minimized Interface (c) 100K Equilibrium Interface

Figure 3.4: Snapshots of interface models in the equilibrium process at 100 K

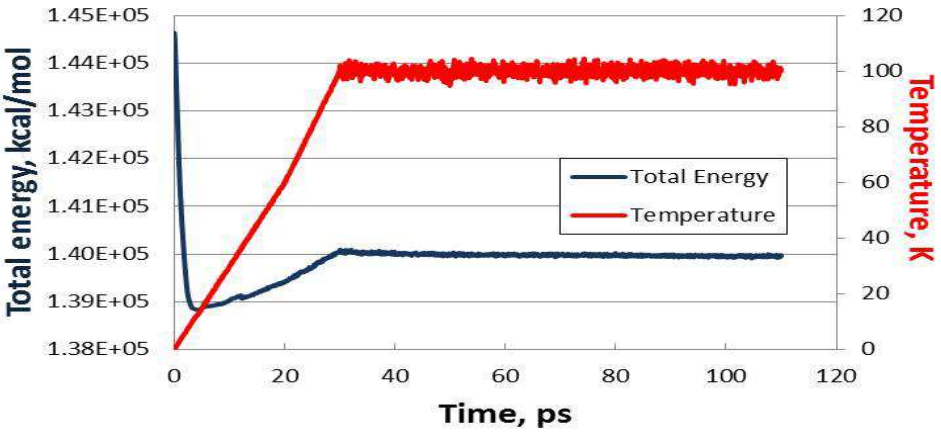

Figure 3.5: The change of total energy and temperature of the 10c80c interface model with respect to time(the time step is 0.01 femtosecond(fs).)

A graphene sheet is constructed to be 24Å by 23Å and has 240 sp^3 hybridized carbon atoms located at their equilibrium positions using an in-house Fortran code. The same graphene sheet has been used for all cases in the present work. In order to obtain the non-functionalized interface model for a CNT-PE nanocomposite, the flat sheet of graphene was introduced to polymer model oriented in x-y plane at z=0 with some prescribed distance prior to minimization as in figure 3.4(a). The interface was then minimized at 0K which allowed the PE to adjust to the interactions with the graphene sheet as in figure 3.4(b). Following the energy minimization at 0K, dynamic equilibration was completed at the required temperature under NVT ensemble for a sufficient amount of time. The Van der Waals interactions between the graphene and the PE attracted the PE to the graphene and established the equilibrium distance between them as in figure 3.4(c). Through all of the equilibration steps, the graphene was constrained to remain flat to simulate the local configuration of CNT in the interface model. In figure 3.5, it can be observed that the total energy has come to a steady stable level after about 3M time steps for the model with 10 polymer chains and 80 carbon atoms per chain(i.e. the 10c80c case), which indicates the achievement of equilibrium status of the interface model. It is noted that different time steps are required to equilibrate the interface models with variable number and length of polymer chains. Different boundary conditions are applied to the interface model based on the separation simulations which are going to run after the equilibration.

3.3 Characterization of the nonfunctionalized interface at the nanoscale

The behavior of the interface in CNT/PE nanocomposites is elaborated by the force-separation responses in normal opening and sliding mode separations. Curvature effect is explored to justify the use of the flat graphene sheet. Parametric studies are conducted to determine suitable size of the representative interface elements in terms of the number of polymer chains, the length of polymer chains and the 'grip' position which is defined here as r. Another important parameter, the influence of temperature on the characteristics of the interface, is also investigated at the nanoscale.

3.3.1 Opening Mode Separation

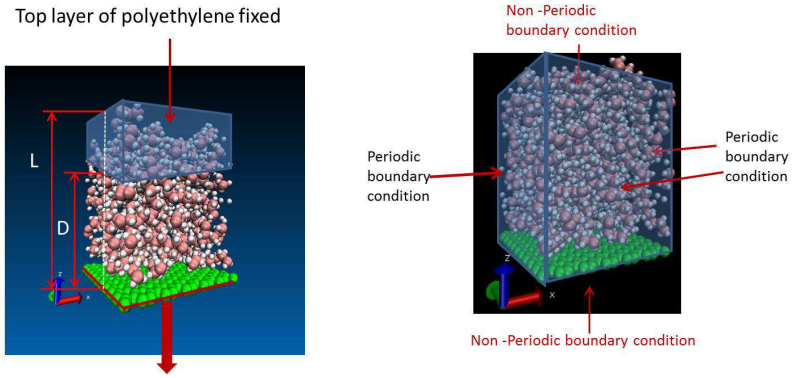

(a) (b)

Figure 3.6: Constraints with the arrow indicating the direction of the velocity on graphene sheet(a) and boundary conditions(b) for representative interface element(10c80c case) in normal mode separation. r in parametric study is defined in (a) as $r = \frac{D}{L}$.

In order to conduct separation mode load transfer studies on the representative interface

element, a region of the polymer at the top has been frozen, i.e. is fully constrained to simulate a grip as shown in figure 5.7(a), while the graphene sheet was displaced in the -z direction through a uniform application of a velocity of 2.5 m/s. Periodic boundary conditions were applied in the x and y directions such that the interface can be effectively taken to be repeated (i.e. infinite) in the x and y directions as shown in figure 5.7(b). Throughout the simulation, which was continued until full separation was achieved, the temperature was fixed at a specified value under a NVT ensemble. The force on each carbon atoms in the graphene sheet (240 carbon atoms) over 4 ps is averaged and combined with the displacement of the graphene sheet in order to obtain the force-separation response. Figure 3.7 provides a typical force-separation response for the normal opening separation mode along with observations of some of the key structural transitions in the MD simulation in the top.

Force-separation response in normal opening separation is observed to have three regions. The first is the loading region which corresponds to a rapid increase to peak force in a nearly linear fashion with the increase of the displacement between the graphene sheet and the polymer. The second is an unloading region which begins after the peak force is attained and corresponds to a gradually decreasing force with increasing displacement. Relative to the loading region, the unloading region is a far more lengthy process which initiates with voids forming in the polymer matrix (figure 3.7(b)) and continues through complete polymer disentanglement (figure 3.7(c)) as individual chains slip past one another. The third region begins upon complete separation of the gripped portion of the polymer from the graphene

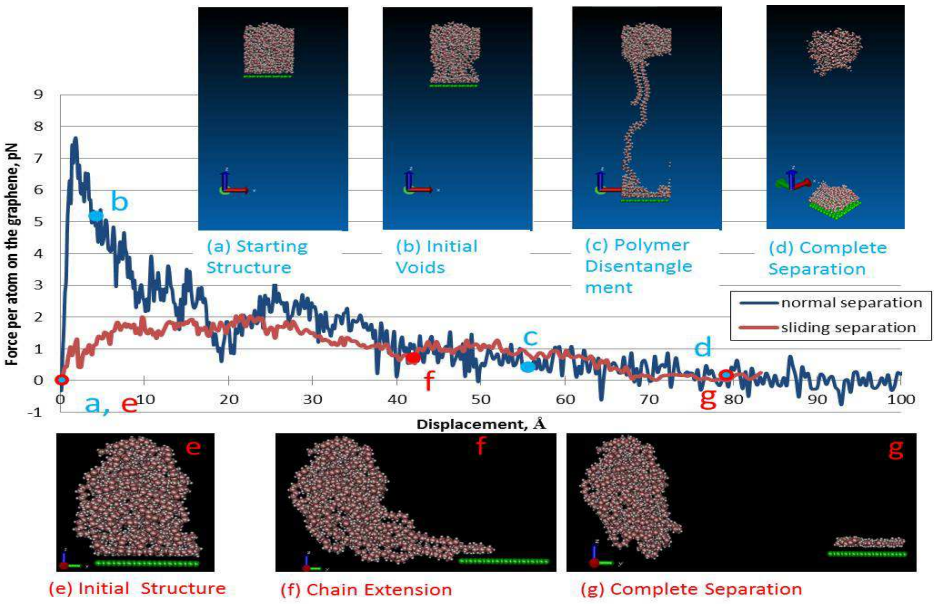

Figure 3.7: Force-separation responses in the normal opening mode and sliding mode separation with snapshots of the separation processes for 10c80c case

sheet (figure 3.7(d)) and is denoted by the force either approaching zero or achieving a steady value depending on whether or not a portion of polymer chains remains attracted to the graphene sheet upon full separation.

3.3.2 Sliding Mode Separation

As with the normal mode separation, a region of polymer at the top of the representative interface element is frozen to simulate a grip while the graphene sheet is displaced at constant velocity until full separation occurs, only here this velocity is in the y-direction as opposed to the z. In order to simulate sliding, periodic boundary conditions are retained in the x-direction while non-periodic boundary conditions are applied in the y- and z-directions as

shown in figure 5.9(b). During the separation process, the averaged force on graphene sheet has been monitored in y direction.

A typical sliding mode force-separation response is provided in figure 3.7 where it is observed that the force initially increases rapidly and then plateaus for a significant period before beginning to decay to zero or a stable small value depending on whether or not any polymer remains attracted to the graphene surface upon full separation. The peak force is around 1.8 pN which is fairly low compared with the peak force of normal separation. It is believed that the plateau may depend on the length of movable polymer chains such that when there are much longer movable polymer chains, they can be stretched out in y direction while remaining in contact with the graphene sheet. It is noted that following the plateau region, the force decreases to 0.5 pN at 43 angstroms of displacement and then begins to increase again to 1 pN before finally resuming its decay. This behavior is believed to be associated with a configuration transition whereby an entangled set of polymer chains began to carry more load before achieving disentanglement and subsequent chain sliding until full separation was achieved. Reductions in polymer chain length and/or increases in the size of the region of frozen polymer in the grip can therefore lead to a shorter plateau region and a sharper decrease in force at the conclusion of the plateau. Three snapshots of sliding mode separation are shown in the bottom of figure 3.7 and corresponds to the points labeled e),f) and g) in the force-separation response.[1]

[1]It is noted that the sliding representative interface element shown in Figures 3.7 and 5.10 is selected to be consistent with the normal mode representative interface element. However, for sliding mode, it would be preferable to use a longer graphene sheet in order to demonstrate sustained sliding in the absence of edge effects. Though not provided herein, the results obtained for such representative interface elements yielded a peak force approximately equal to that of the sliding mode representative interface element reported here.

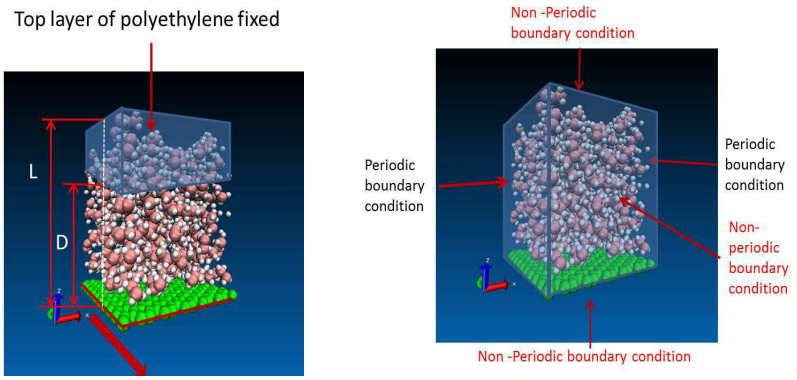

(a) (b)

Figure 3.8: Constraints with the arrow indicating the direction of the velocity on graphene sheet(a) and boundary conditions(b) for representative interface element(10c80c case) in sliding mode separation. r in parametric study is defined in (a) as $r = \frac{D}{L}$.

3.3.3 Curvature Study

In order to investigate the significance of curvature on the force-separation response, curved graphene sheets corresponding to CNTs with differing radii were studied. The graphene sheets with 240 sp^3 hybridized carbon atoms were rearranged to form the curvature of a cylinder of radius 6Å(R6), 8Å(R8), 12Å(R12) and 16Å(R16) as shown in Figure 3.9 corresponding to CNTs of armchair (9,9), (12,12), (18,18) and (24,24), respectively. The amorphous polymer in the representative interface elements includes 10 polymer chains and 80 carbon atoms per chains(10c80c). The amorphous polymer was introduced to the curved graphene segments and equilibrated in the same manner as the flat graphene sheets. The averaged force recorded on the graphene sheet is in the z-direction as opposed to the radial direction of the curved graphene sheet.

Force-separation responses are shown in Figure 3.9 for the interface models with the flat

Table 3.1: Peak force and separation energy for all cases in curvature study.

Cases	Peak force (pN)	Separation energy (mJ/m^2)
flat graphene sheet	7.65	560.25
(24,24)	6.58	474.68
(18,18)	7.03	385.24
(12,12)	6.82	372.04
(9,9)	6.08	314.89

graphene sheet and curved graphene sheets, all of which depict the same trend of initial sharp rising and then gradually decreasing after the peak force. The similarity observed in force-separation responses demonstrates that the representative interface elements with the flat graphene sheet is a good representation for the CNT-PE interface system. From the inset in the Figure 3.9 and Table 3.1 it is observed that the curved graphene representative interface elements yield a smaller peak force as the curvature increases. This observation is believed to be linked to the increasing normal and sliding mode mixing as the curvature increases. As the sliding mode was observed to have a significantly lower peak force (Figure 3.7), increasing curvature corresponds to increasing portions of the graphene surface being loaded in sliding mode as opposed to normal mode. The result is taken as an indication that the normal and sliding modes are sufficiently characterized on the flat graphene sheet and the corresponding cohesive zones can be applied to CNTs demonstrating a range of radii. As such, only the flat graphene sheet will be considered in the parametric study and cohesive formulations which follow.

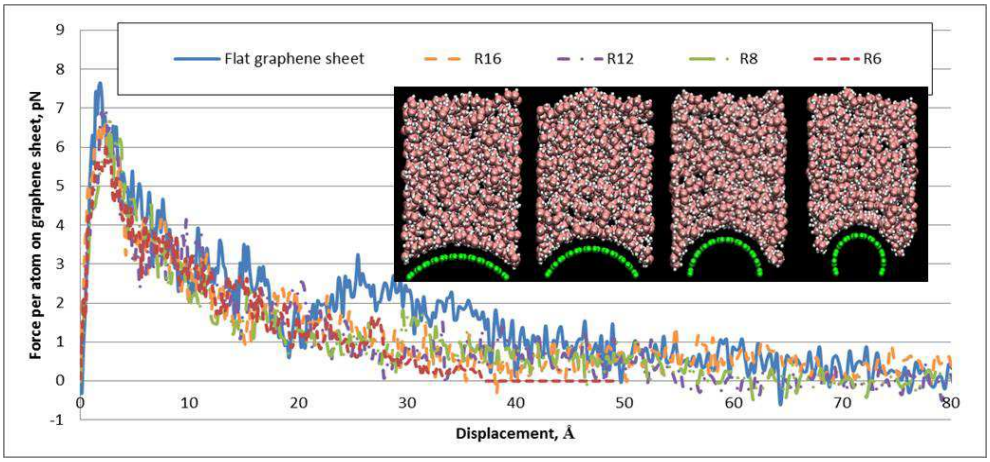

Figure 3.9: The comparison of the force-separation responses in the opening mode separations between the interface models with the flat graphene sheet and the curved graphene sheets. The insets are the representative interface elements with curved graphene sheets corresponding to CNTs of armchair (9,9), (12,12), (18,18) and (24,24) from the left to the right.

3.3.4 Assessing Representative Character of Interface Element

A parametric study was undertaken in order to establish a suitable size of representative interface elements for the interface model. Sensitivity tests in terms of three important parameters which determine the size of representative interface elements, namely, the number of the polymer chains, the length of the polymer chains and the distance between the graphene sheet and 'grips' were performed to discern their influence on the peak force and separation energy in establishing converged force-separation response of the interface. A total of 36 cases were parametrically studied and designated according to the three parameters of interest as mCnCrN where m refers to the number of polymer chains (between 6 and 30), n denotes the length of polymer chains in terms of number of carbon atoms (between

60 and 300)[2], and r denotes the relative influence of the 'grip' as measured by the ratio $r = \frac{D}{L}$ as denoted in Figure 5.7(a). It is noted that as the number and length of polymer chains increases, the area of the graphene sheet remains fixed. As such, higher m and n correspond to larger dimensions in the z-direction so that r is more appropriately thought of as the percentage of polymer column height which is unconstrained by the 'grip', i.e. is outside of the frozen region. Values for this parameter span from approximately 58% to 77% unconstrained. It is further noted that polymer chains may be fully, partially or not at all contained within the frozen 'grip' region, and therefore extend the 'grip' interaction through subsequent entanglements with chains in the unconstrained region. The specific cases and the corresponding number of atoms in each case are provided in Table 3.2. For each case identified, three different configurations are selected from the range of dynamic equilibrium of the interface model and are used to establish initial estimates of the average response and standard deviation for the case.

In order to insure that there are not residual biases from starting with straight polymer chains in the amorphous polymer construction and to explore the potential degree of entanglements within the final amorphous polymer configurations selected for parametric study, the average tortuosity(τ_{or}) for each case is measured and reported in Table 3.3 by using Equation 3.6. By definition, lower average τ_{or} means polymer chains in the model prefer to entangle with itself or other polymer chains, and higher average τ_{or} means polymer chains in the model

[2]It is noted that all of our simulations involve polymer chains which are of a rather short length as compared to real-life polymer chains. To simulate real-life polymer chains would be significantly more computationally expensive, and may necessitate coarse graining. However, with increasing chain length and number of chains, a convergent behavior was observed in our present results which we believe provides a reasonable alternative to larger coarse graining in assessing interface load transfer.

are more straight. In Table 3.3, as the number of the polymer chains increases from 6 to 30 with 100 carbon atoms per chain, τ_{or} increases from 0.29 to 0.4 which correlates with the increase of the density of the amorphous chains. In contrast, as the length of the chains are increased, in this case by a factor of 3 in going from the 10c100c case to the 10c300c case, average tortuosity decreases from 0.32 to 0.22 as the longer chains have greater possibility to form entanglements than do shorter chains.

$$\tau_{or} = \frac{\sum_{i=1}^{m}\sum_{j=2}^{n-1}\frac{a_j^i}{(j-1)l}}{(n-1)m} \tag{3.6}$$

where a_j^i stands for the distance between carbon atom j and carbon atom 1 in the i^{th} polymer chain with atom 1 at one end. l is the equilibrium length of one carbon-carbon bond.

The peak traction(T), the separation distance(S) and the separation energy(E) are obtained for all the cases by averaging over the three simulations(as shown in Table 3.4 for r1 cases, Table 3.5 for r2 cases, Table 3.6 for r3 cases). Table 3.7 provides averaged T, E and S over r1, r2 and r3 for each case. The peak traction is calculated by averaging the peak force on the graphene sheet over its area. Similar trends are observed for the force-separation responses in the normal mode separations for all of the cases in the sensitivity study.

It is observed that upon the full separation, there are either polymer chains remaining with the graphene sheet (Figure 3.7) or there are no polymer chains on the graphene sheet, resulting in different third regions of force-separation relations, e.g. the force hovering just above zero when there is residual polymer continuing to interact with the graphene sheet

versus hovering about zero when there is no residual polymer. Only for a few cases (6c60c, 15c200c and 10c300c) do all of the realizations yield normal separations at the interface, and only for the 30c100c case do all of the realizations yield separation within the polymer. As there is no clear and direct measure of entanglement, effort has been made to correlate tortuosity with the presence of residual polymer on the graphene interface at full separation for a few of these cases. For example, with strong entanglement within polymer as indicated by a small tortuosity value (like in 10c300c case), separations happened at the interface. This is believed to be the result of a large number of entanglements which hinder the movement and disentanglement of the polymer chains. For 30c100c case, tortuosity is fairly large implying fewer entanglements between polymer chains, and resulting in failure in all normal separation realizations occurring within the polymer. For the remaining cases (6c80c, 6c100c, 8c60c, 8c80c, 8c100c, 10c60c, 10c80c, and 10c100c), the different realizations for each case yield separations that are observed at either the interface or within the polymer, and therefore do not provide very clear correlations with length or number of polymer chains. It is noted that cases such as these (e.g. 6c100c, 8c100, 10c100c) have a tortuosity (0.3) which is directly in between those of the cases which consistently failed at the interface (0.2) and which consistently failed in the polymer (0.4).

As was noted, a higher tortuosity (0.4 for the 30c100c realizations) corresponded to less entanglements and therefore separation within the polymer while lower tortuosity (0.22 for the 10c300c realizations) was associated with more entanglements and therefore separation at the interface. Similarly, less entanglements allow for the polymer to more easily disentangle

and extend the separation over the length of the polymer chains resulting in larger separation distance and separation energy, whereas more entanglements hinder movement of the polymer chains preventing disentanglement and resulting in shorter separation distance, and hence smaller separation energy as indicated most clearly in Table 3.6. However, there does not appear to be a clear correlation of tortuosity with peak traction as most peak traction values for the various realizations of the all cases appear to fluctuate about some mean value (e.g. 0.34 GPa).

In terms of identifying acceptable interface parameters for construction of continuum scale cohesive zones, it is noted in Figure 3.10 that with increasing length of the polymer chains at a fixed number of chains, the cases with 10 polymer chains (10cxxc) demonstrate a peak traction which looks fairly converged. However, further increases in the number of chains results in a slight reduction in peak traction. In contrast, increasing the number of polymer chains at fixed length as shown for the xxc100c cases in Figure 3.11 results in a fairly converged average separation energy, though as noted above, increasing in length beyond 200c result in a sharp decrease in separation energy due to increased entanglement. In order to reflect the overall behavior of the interface, the average peak force and separation energy was selected as the initial input parameters for the cohesive zone law at the interface in the microscale simulations presented below. As the values of peak traction and separation energy for the 10c80c case (0.32 GPa, 503 mJ/m^2) are close to the average values of peak traction and separation energy obtained from all of the cases (0.32 GPa, 537 mJ/m^2), the 10c80c case input parameters were used to develop cohesive zone laws for describing the

Table 3.2: Sensitivity tests

Parameters for sensitivity tests			
Number of polymer chains	Number of monomers	Number of atoms	r *
6	60 (6c60c)	1,332	r1 r2 r3
	80 (6c80c)	1,692	r1 r2 r3
	100 (6c100c)	2,052	r1 r2 r3
8	60 (8c60c)	1,696	r1 r2 r3
	80 (8c80c)	2,176	r1 r2 r3
	100 (8c100c)	2,656	r1 r2 r3
10	60 (10c60c)	2,060	r1 r2 r3
	80 (10c80c)	2,660	r1 r2 r3
	100 (10c100c)	3,260	r1 r2 r3
30	100 (30c100c)	9,300	r1 r2 r3
15	200 (15c200c)	9,270	r1 r2 r3
10	300 (10c300c)	9,260	r1 r2 r3

* r1=57.6% unconstrained; r2=69.2% unconstrained; r3=76.9% unconstrained.

behavior of the interface in the micromechanics models.

3.3.5 Temperature study

In addition to the 100K results presented in figure 3.7, opening mode separation simulation has been conducted at 300K in order to investigate the influence of temperature on the force-separation response for the non-functionalized CNT-PE interface. The opening mode force vs displacement curves at 100K and 300K for 10c80c case are provided in figure 5.14. The 100K and 300K force-separation responses show similar trends, beginning with a rapid increase to peak force (peaking on the 5-10 angstroms of displacement), and followed by a gradual decrease in force with increasing graphene separation to full separation. However, it

Table 3.3: Tortuosity as measured according to equation 3.6 for the three initial configurations for a subset of the cases in the parametric study.

Cases with density(g/cm^3)	Average Tortuosity	Average over three initial configurations
6c100c(0.92)	0.2987±0.0520 0.2969±0.0525 0.3006±0.0507	0.30± 0.002
8c100c(0.94)	0.3489±0.0603 0.3479±0.0620 0.3334±0.0585	0.34±0.009
10c100c(0.93)	0.3262±0.0779 0.3311±0.0754 0.3093±0.0626	0.32±0.011
30c100c(0.96)	0.4133±0.1298 0.4155±0.1297 0.4125±0.1242	0.4±0.02
10c300c(0.97)	0.2234±0.0512 0.2215±0.0519 0.2221±0.0520	0.22 ±0.001

Table 3.4: Peak traction (GPa), separation energy(mJ/m^2) and separation distance ($\mathring{A}$) for r1 cases

	Peak traction	Energy	Separation Distance
6c60c	0.44 ± 0.0329	357.19 ± 11.32	39.65 ± 2.07
6c80c	0.41 ± 0.0083	384.24 ± 43.48	50.20 ± 3.74
6c100c	0.28 ± 0.0157	384.92 ± 45.79	52.89 ± 18.45
8c60c	0.27 ± 0.0058	347.65 ± 22.56	34.09 ± 4.32
8c80c	0.24 ± 0.0183	438.88 ± 33.45	68.23 ± 11.76
8c100c	0.23 ± 0.0240	596.87 ± 72.93	82.60 ± 4.85
10c60c	0.37 ± 0.0243	282.71 ± 13.70	29.87 ± 1.51
10c80c	0.28 ± 0.0183	395.78 ± 31.73	62.80 ± 5.98
10c100c	0.33 ± 0.0428	493.08 ± 21.79	46.30 ± 4.69
30c100c	0.24 ± 0.0086	582.11 ± 6.55	95.10 ± 12.26
15c200c	0.26 ± 0.0181	723.99 ± 20.28	87.97 ± 3.17
10c300c	0.30 ± 0.0141	512.78 ± 87.50	65.83 ± 24.32

Table 3.5: Peak traction (GPa) ,separation energy(mJ/m^2) and separation distance ($\mathring{A}$) for r2 cases

	Peak traction	Energy	Separation Distance
6c60c	0.46 ± 0.0375	364.82 ± 23.92	39.46 ± 1.45
6c80c	0.39 ± 0.0314	457.82 ± 30.86	57.10 ± 7.40
6c100c	0.29 ± 0.0129	665.36 ± 107.55	90.30 ± 20.88
8c60c	0.30 ± 0.0114	388.18 ± 32.74	52.50 ± 5.02
8c80c	0.22 ± 0.0105	557.11 ± 39.76	74.90 ± 2.97
8c100c	0.27 ± 0.0267	758.30 ± 73.27	91.50 ± 10.15
10c60c	0.41 ± 0.0393	361.09 ± 41.37	31.27 ± 0.50
10c80c	0.33 ± 0.0248	538.01 ± 39.68	84.30 ± 3.73
10c100c	0.34 ± 0.0377	613.45 ± 106.92	58.03 ± 16.87
30c100c	0.27 ± 0.0125	719.05 ± 26.47	93.33 ± 11.55
15c200c	0.29 ± 0.0110	623.86 ± 43.47	74.70 ± 22.71
10c300c	0.35 ± 0.0268	393.12 ± 61.30	39.28 ± 2.41

Table 3.6: Peak traction (GPa), separation energy(mJ/m^2) and separation distance ($\mathring{A}$) for r3 cases

	Peak traction	Energy	Separation Distance
6c60c	0.42 ± 0.0268	409.75 ± 13.82	38.70 ± 0.76
6c80c	0.39 ± 0.0130	506.83 ± 57.68	62.16 ± 6.44
6c100c	0.29 ± 0.0041	909.49 ± 81.48	119.63 ± 14.95
8c60c	0.27 ± 0.0068	484.57 ± 3.62	72.07 ± 3.18
8c80c	0.24 ± 0.0058	662.05 ± 40.76	79.50 ± 8.72
8c100c	0.29 ± 0.0198	603.26 ± 75.40	80.23 ± 10.84
10c60c	0.40 ± 0.0142	359.01 ± 22.83	31.73 ± 0.50
10c80c	0.34 ± 0.0370	576.92 ± 72.53	81.83 ± 2.45
10c100c	0.37 ± 0.0338	767.66 ± 191.32	102.33 ± 23.35
30c100c	0.30 ± 0.0211	866.46 ± 79.82	105.67 ± 9.81
15c200c	0.29 ± 0.0050	861.35 ± 181.39	100.83 ± 14.22
10c300c	0.39 ± 0.0303	400.30 ± 34.85	39.00 ± 2.55

Table 3.7: Averaged peak traction (Gpa) and averaged separation energy(mJ/m^2) for each case over r1, r2 and r3.

	Peak traction	Energy	Separation Distance
6c60c	0.44 ± 0.0133	377.25 ± 23.19	39.27 ± 0.41
6c80c	0.40 ± 0.0126	449.63 ± 50.38	56.49 ± 4.90
6c100c	0.29 ± 0.0021	653.26 ± 214.33	87.61 ± 27.31
8c60c	0.28 ± 0.0119	406.80 ± 57.43	52.89 ± 15.50
8c80c	0.23 ± 0.0096	552.68 ± 91.16	74.21 ± 4.63
8c100c	0.26 ± 0.0230	652.81 ± 74.64	84.78 ± 4.85
10c60c	0.39 ± 0.0152	334.27 ± 36.47	30.96 ± 0.79
10c80c	0.32 ± 0.0257	503.57 ± 77.86	76.31 ± 9.61
10c100c	0.35 ± 0.0151	624.73 ± 112.38	68.89 ± 24.13
30c100c	0.27 ± 0.0259	722.54 ± 116.11	98.03 ± 5.45
15c200c	0.28 ± 0.0166	736.40 ± 97.35	87.83 ± 10.67
10c300c	0.35 ± 0.0359	435.40 ± 54.79	48.04 ± 12.58

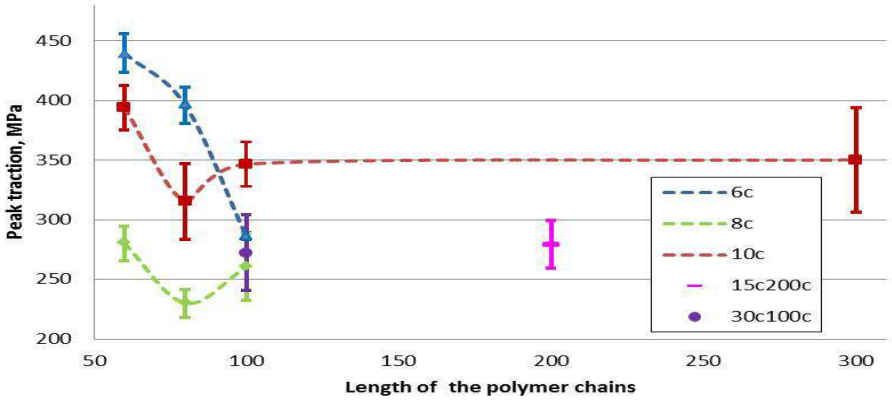

Figure 3.10: Peak traction for all r1 cases in parametric study as shown in table 3.4

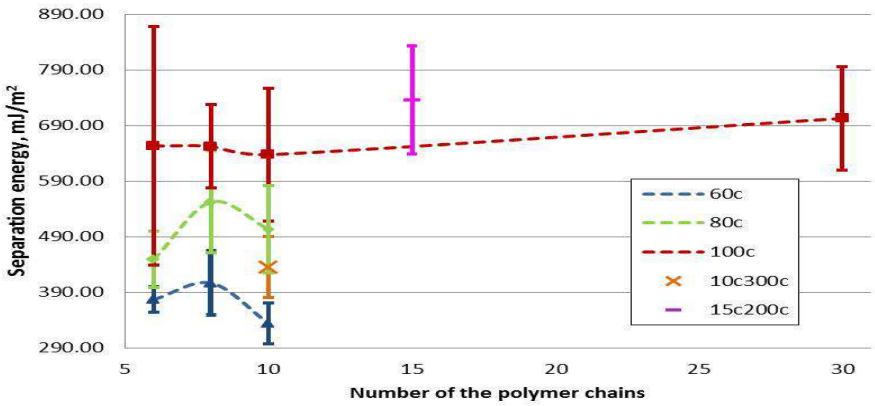

Figure 3.11: Separation energy for all r1 cases in parametric study as shown in table 3.4

is observed that both the peak force and the separation distance of the 300K case are much smaller (69.5% and 41.9%, respectively) than the 100K case, therefore resulting in a much smaller separation energy for the 300K case (73.0% smaller). It implies that the interface becomes weaker with the increase of the temperature at the nanoscale , and hence indicates the macroscale effective properties will likewise display temperature dependence.

3.4 Macroscale effective elastic properties of CNT-PE nanocomposites with molecular representative interface element derived cohesive zone models

Effective macroscale elastic material properties of CNT-PE nanocomposites can be calculated using analytic micromechanics. In general, many micromechanics models do not directly

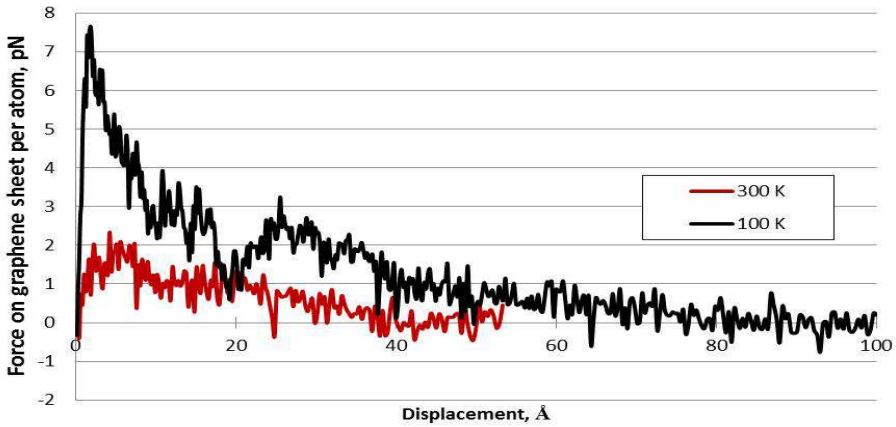

Figure 3.12: Force-separation responses in the opening mode separation at 100K and 300K. It is noted that the value of force reported is the average value obtained over all carbon atoms in the graphene sheet (240 atoms), and over 4 to 8 ps (40000 to 80000 time steps) so as to reduce and smooth the data.

consider interface effects and assume a perfectly bonded interface between constituent phases (e.g. fiber and matrix) in which continuity of displacements and traction are instead enforced [73]. In the present work, the assumption of continuity of displacements is relaxed through the use of cohesive zone models at the CNT-PE interface in both analytic and computational micromechanics approaches. Cohesive zone traction-displacement laws are developed based on the force-separation responses obtained from MD simulations at the nanoscale.

3.4.1 Cohesive Zone Law

The cohesive zone traction-displacement law is obtained by averaging the force-separation response from the MD over the area of the graphene sheet to describe the behavior of the interface between CNTs and matrix in the nanocomposites. In the normal (separation)

direction, a bilinear cohesive zone law is developed as shown in Figure 3.13 by using the averaged peak traction, separation energy and separation distance for 10c80c case from normal opening separation at 100K and 300K. As the direct conversion of the force-separation response would yield a cohesive zone law which deviates from a strict bilinear interpretation, it is not possible to enforce all three parameters simultaneously. Hence, two different fitting strategies were applied, one with the peak traction and separation energy enforced as in Figure 5.17(a) and the other with the peak traction and separation distance enforced as in Figure 5.17(b).

For both bilinear cohesive law fittings, the same peak traction is used resulting in identical loading portions and initial failure points for both cohesive laws. For the bilinear cohesive zone law fit based on the separation energy, total failure of the interface is obtained when the total separation energy is expended, corresponding to a separation distance which is less than that obtained from the nanoscale representative interface element (42.5 % less for the 10c80c case shown in Figure 5.17(a)). For the fitting where the separation distance is kept, total failure of the interface is achieved when the distance between the CNT and the matrix at the interface reaches the separation distance, corresponding to a separation energy which is more than that obtained from the nanoscale representative interface element (74.1 % more for the 10c80c case shown in Figure 5.17(b)). As a small difference (up to 0.3%) was observed in the effective elastic properties of the nanocompsite between the two bilinear representations of a given interface, the peak traction/separation energy bilinear cohesive zone is chosen for use in the remainder of the present work.

The form of cohesive zone laws is provided shown in the Equations 3.7 , 3.8 , 3.9 , 3.10 and 3.11.

$$t_{n1} = k_{n1}\Delta u_n + b_1 \qquad if\ \Delta u_n \leq \Delta u_{npeak} \tag{3.7}$$

$$t_{n2} = k_{n2}\Delta u_n + b_2 \qquad if\ \Delta u_n > \Delta u_{npeak} \tag{3.8}$$

$$t_{n3} = 0 \qquad if\ A > A_{tot} \tag{3.9}$$

where t_{n1}, t_{n2} and t_{n3} are the traction, k_{n1} and k_{n2} are the stiffness for the loading and unloading portion, Δu_n is the relative normal displacement of the interface, Δu_{npeak} is the relative normal displacement of the interface at which the peak traction is reached and A is the separation energy. The area under the bilinear cohesive zone law, A_{tot}, is the total separation energy which is the sum of A_1, the energy for the loading portion of the cohesive zone law, and A_2, the energy for the unloading portion of the cohesive zone law, and used to calculate the fitting parameters of the traction-displacement law as follows:

$$k_{n1} = \frac{t_{npeak}}{\Delta u_{npeak}} \qquad\qquad b_1 = 0 \tag{3.10}$$

$$k_{n2} = -\frac{t_{npeak}}{\Delta \overline{u}} = -\frac{t_{npeak}^2}{2A_2} \qquad\qquad b_2 = -k_{n2}\frac{2A_{tot}}{t_{npeak}} \tag{3.11}$$

where t_{npeak} is the peak traction and $\Delta\overline{u}$ is the difference between Δu_{npeak} and Δu_{sep}, which

denotes the relative normal displacement of the interface upon full separation.

For sliding mode separation, the traction should remain constant after it reaches the peak value as in pure sliding (i.e. no normal separation), the polymer and CNT remains in contact. The MD simulations show a subsequent decrease in traction after some time and this is the product of the necessity to use a finite area and non-periodic boundary conditions in the sliding mode simulations such that the polymer can slide off of the graphene shelf. The cohesive zone laws for sliding are developed based on the force-separation response of the 10c80c RVE as depicted in Figure 3.14, which is fit to traction-displacement laws given by Equations 3.12 and 3.13.

$$t_{s1} = k_{s1}\Delta u_s \qquad if\ \Delta u_s \leq \Delta u_{speak} \qquad\qquad k_{s1} = \frac{t_{speak}}{\Delta u_{speak}} \tag{3.12}$$

$$t_{s2} = t_{speak} \qquad if\ \Delta u_s \leq \Delta u_{speak} \tag{3.13}$$

where t_{s1} and t_{s2} are the traction, k_{s1} is the stiffness for the loading portion and t_{speak} is the peak traction in sliding. Δu_s is the relative displacement of the interface in sliding and Δu_{speak} is the relative displacement of the interface at the peak traction.

The bilinear cohesive zone law for normal mode separation only retains information regarding peak traction, separation energy and the displacement at the peak traction information from the MD simulations, while the sliding cohesive zone law only retains information regarding

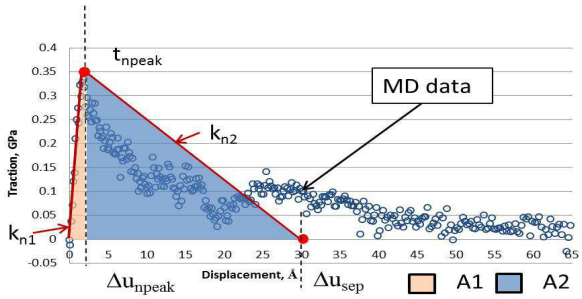

(a) cohesive zone law matching the peak traction and separation energy obtained from the MD traction-separation response

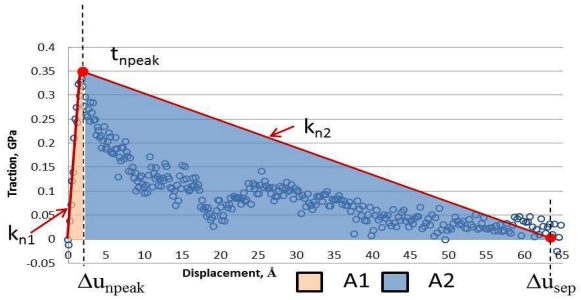

(b) cohesive zone law matching the peak traction and separation distance obtained from the MD traction-separation response

Figure 3.13: MD cohesive zone traction-displacement laws and corresponding bilinear cohesive zones laws for 10c80c case in normal mode separation at 100K

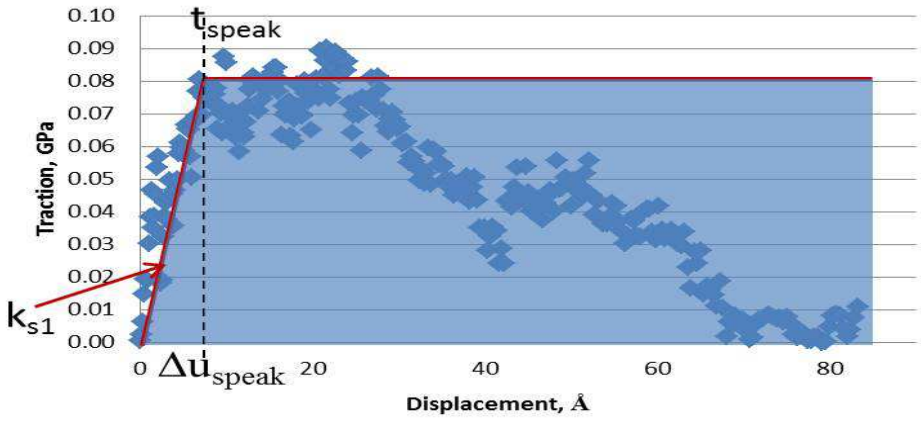

Figure 3.14: Cohesive zones law for 10c80c case in sliding mode separation at 100K

peak traction and the displacement at the peak traction information. Therefore only through these retained values does the influence of atomistic details such number and length of polymer chains, tortuosity, and temperature get transferred to the higher continuum scales. All other atomistic details, e.g. which polymer chain was closest to the graphene interface and how entangled it was with other polymer chains, is not directly retained, though they contribute to the error bars on the retained parameters. The big advantage in transferring a reduced set of MD information to the continuum scale through the cohesive zones is that the continuum simulations do not become restricted to atomistic time scales.

3.4.2 Application of Bilinear Cohesive Zone Law in Analytic Micromechanics Approach

A composite cylinder model (CCM) ([42, 43]) with an innermost layer corresponding to the hollow CNT and outermost layer consisting of the matrix material is used to obtain the effective elastic properties for CNT-PE nanocomposites with aligned, high aspect ration CNTs. Between the CNT and PE layers the traction-displacement law for the fit cohesive zone is applied. Here we summarize the application of the model towards obtaining the macroscale effective in-plane bulk modulus (K_{23}). For this case, the i^{th} layer displacement field is given by:

$$u_r^{(i)} = D_1^{(i)} r + \frac{D_2^{(i)}}{r} \tag{3.14}$$

$$u_\theta^{(i)} = 0 \tag{3.15}$$

$$u_z^{(i)} = 0 \tag{3.16}$$

where $D_1^{(i)}$ and $D_2^{(i)}$ are constants determined from the boundary and matching conditions. The boundary conditions are given by:

$$u_r^{(N)}(r = r_N) = \epsilon_0 r_N \tag{3.17}$$

$$\sigma_{rr}^{(1)}(r = r_0) = 0 \tag{3.18}$$

where r_0 is the CNT inner radius, N and 1 denote the matrix layer and CNT layer of the N=2 composite cylinder assemblage as in Figure 3.15, respectively, and where r_N is obtained in terms of CNT outer radius and volume fraction, v_f, from:

$$r_N = \sqrt{\frac{(r_1)^2}{v_f}} \tag{3.19}$$

These boundary conditions correspond to a uniform radial strain at the outer boundary and a traction-free condition within the hollow of the CNT. For the perfect bonding case, the matching conditions are given by:

$$u_r^{(j)}(r = r_i) = u_r^{(j+1)}(r = r_i) \tag{3.20}$$

$$\sigma_{rr}^{(j)}(r = r_i) = \sigma_{rr}^{(j+1)}(r = r_i) \tag{3.21}$$

where j ranges from 1 to N-1. These matching conditions correspond to continuity of displacements and tractions at the CNT-PE interface. In the present work, the continuity of displacement condition is relaxed such that the interface condition becomes

$$u_r^{(1)}(r = r_1) = u_r^{(2)}(r = r_1) - \Delta u \tag{3.22}$$

where the relative displacement (Δu) of the interface is given by the auxiliary equation describing the bilinear cohesive zone as:

$$\sigma_{rr}^{(1)}(r = r_1) = \sigma_{rr}^{(2)}(r = r_1) = t_{nm} = k_{nm}\Delta u_n + b_m \tag{3.23}$$

where m takes a value of 1 or 2 depending on the cohesive zone in the loading or unloading region of the bilinear cohesive zone law for normal mode separation. It is noted that the axisymmetric nature of the assemblage geometry and boundary conditions result in the interface only being subject to normal separation so that the sliding mode need not be considered. In both the perfectly bonded and cohesive zone interfaces, the effective in-plane bulk modulus can be obtained from the strain energy equivalency between the composite cylinder assemblage and an effective homogeneous cylinder. It can be expressed in terms of the radial stress and displacement at the outer boundary of the matrix as:

$$K_{23}^{(eff)} = \frac{\sigma_{rr}^{(N)}}{2u_r^{(N)}(r = r_N)/r_N} \tag{3.24}$$

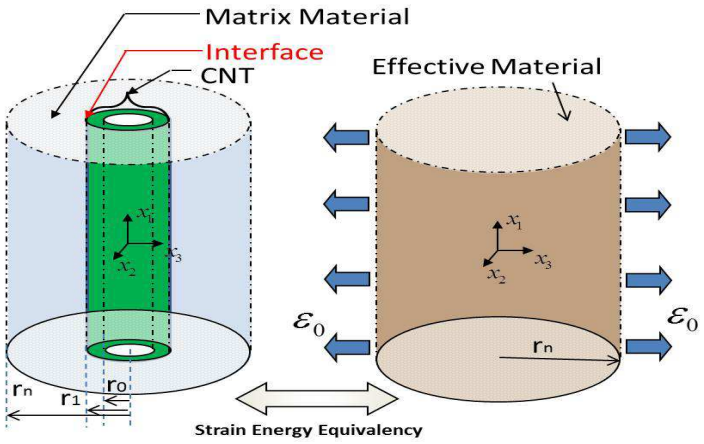

Figure 3.15: Schematic representation of the composite cylinder model with a cohesive interface for CNTs-polymer nanocomposite.

Figure 3.16 depicts the macroscale effective in-plane bulk modulus K_{23} for perfectly bonded and discontinuous interfaces as a function of applied strain for a CNT volume fraction (vf) of 1% at both 100K and 300K. For the perfect bonding case, K_{23} is observed to be independent of the applied macroscale strain and temperature effect. For the cohesive zone cases, K_{23} are initially constant in the loading region of the cohesive law, however, at a lower value than for the perfect bonding cases by 2.4% at 100K and 4.2% at 300K, respectively. Once the bilinear cohesive zone model transitions to the unloading regime, K_{23} is observed to nonlinearly decrease with increasing applied strain up to a 4.6% decrease (at both 100K and 300K) in K_{23} relative to the perfect bonding case. Table 3.8 provides the percentage reduction in K_{23} relative to the perfect bonding case for the 100K and 300K cohesive zones

Table 3.8: Reduction of K_{23} in analytic (CCM) and computational micromechanics (FEA) for cohesive zone model with respect to the perfect bonding model for 0.01, 0.1, and 0.5 volume fraction. Values are reported in terms of loading/unloading stages.

CNT vf	percentage reduction at 100 K		percentage reduction at 300 K	
	CCM	FEA	CCM	FEA
1%	2.4% -4.6%		4.2 % -4.7%	
10%	21% -37%	27% -39%	34% -37%	35% -39%
50%	73% -90%	81.3% -92.9%	88% -90%	89.2% -93.6%

cases at CNT volume fractions of 0.01, 0.1, and 0.5. It is observed that as the CNT volume fraction increases, the interface influence increases significantly from 4% up to 30% and 90%, respectively, indicating that load transfer within a bundle of CNTs (i.e. corresponding to high local volume fractions) may be a critical concern.

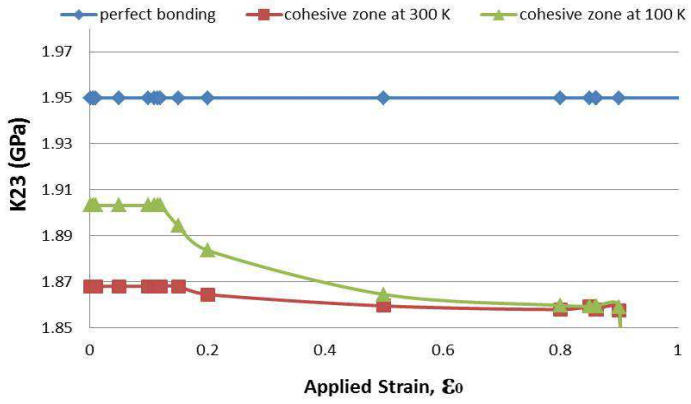

Figure 3.16: Macroscale effective in-plan bulk modulus K_{23} for a 0.01 volume fraction CNT-PE nanocomposite from composite cylinder models with a perfectly bonded interface and with cohesive zones at 100K and 300K.

3.4.3 Application of Bilinear Cohesive Zone Law in Finite Element Analysis

Aside from K_{23}, it is difficult to calculate the effective material properties of CNT-PE nanocomposites analytically using CCM for the cases with a cohesive zone model interface as there is a loss of axisymmetry with both the normal and sliding modes of the cohesive law engaged. In order to estimate other effective material properties of the CNT-PE nanocomposites with cohesive zone interfaces, computational micromechanics approaches ([43]) are applied within a finite element framework. Here a 2-D RVE consisting of a regular hexagonal array of aligned CNTs with cohesive zone elements corresponding to both normal (Equation 3.7, 3.8 and 3.9) and sliding (Equation 3.12 and 3.13) modes placed at the CNT-PE interface is used to obtain additional in-plane properties(e.g. stiffness components C_{22} and C_{66}) of the transversely isotropic effective nanocomposite based on the volume averaged stresses and strains.

An RVE at a CNT vf of 0.1 is shown in Figures 3.17 and 3.18 in both the undeformed and deformed configurations corresponding to the boundary conditions associated with determining C_{22} and C_{66} , respectively. For determining effective C_{22}, the boundary conditions are such that the bottom of the RVE was fixed in both the x- and y-directions and the left and right boundary of the RVE fixed in the x-direction, while the top boundary of the RVE was displaced in y-direction by $u_y = \varepsilon_0 L_0$ where L_0 is the undeformed length of the RVE in the y-direction. For determining effective C_{66}, the boundary conditions are such that the

left and right boundary of the RVE was fixed in y-direction with the bottom still fixed in both direction and a displacement boundary condition of $u_x = 2\varepsilon_0 L_0$ in x-direction along the top boundary.

From the deformed configurations in Figure 3.17(a) and 3.18(a) corresponding to the C_{22} and C_{66} boundary conditions, respectively, at a applied strain level of 0.75 one can note the influence of the cohesive zones on the interface separation and stress distribution in the polymer matrix and CNT. It is noted that some of the cohesive zones in the interface regions have achieved complete failure, i.e. have fully separated. Table 3.9 provides the percentage reduction of C_{22} and C_{66} relative to perfect bonding case for the 100K and 300K cohesive zone cases at CNT volume fraction of 0.1 and 0.5 in FEA. Effective C_{22} and C_{66} at 100K and 300K are provided in Figure3.19 with applied strain for CNT-PE nanocomposites with a CNT volume fraction of 0.1. For small range of strain, constant C_{22} and C_{66} are given for perfect bonding cases at both 100K and 300K. For cohesive zone models, C_{22} is constant in the strain range of 0-0.12 and then begins to nonlinearly decrease with further increasing of the applied load in an analogous manner as was observed for the composite cylinder K_{23} results. This transition corresponds to the loading and unloading regimes of the normal opening cohesive zone law and therefore indicates that normal separation of the cohesive zones dominates the effective property response for C_{22}. In contrast to C_{22} , the effective C_{66} results do not demonstrate a clear loading region. Instead, the effective C_{66} begins with an increasing region which reaches a maximum near the transition strain level observed in the C_{22} results and subsequently decays. This markedly different behavior is believed to be

Table 3.9: Reduction of C_{22} and C_{66} in computational micromechanics (FEA) for cohesive zone model with respect to the perfect bonding model for 0.1, and 0.5 volume fraction. Values are reported in terms of loading/unloading stages.

CNT vf	percentage reduction at 100 K		percentage reduction at 300 K	
	C_{22}	C_{66}	C_{22}	C_{66}
10%	24% -34%	16% -23%	34% -35%	24% -25%
50%	79% -88%	66% -77%	88.8% -89.4%	79.7% -80.6%

the result of two factors: (1) that the sliding mode peak traction is significantly lower than that of the normal mode leading to (2) a transition from the cohesive zones being primarily loaded in sliding mode initially to being loaded in normal mode with increasing macroscale shear strain.

In order to compare the computational micromechanics results with those obtained from the analytic composite cylinder model, the macroscale effective nanocomposite in-plane (plane-strain) bulk modulus, K_{23}, for the CNT-PE nanocomposites is calculated based on C_{22} and C_{66} stiffness components by using the relation $K_{23} = C_{22} - C_{66}$. Table 3.8 provides the percentage reduction in K_{23} relative to the perfect bonding case for the 100K and 300K cohesive zones at CNT volume fractions of 0.1, and 0.5 in FEA. In Figure 3.20, for CNT-PE nanocomposites with a volume fraction of 0.1, K_{23} from the computational micromechanics is compared to the analytical composite cylinder model results for perfect bonding and cohesive interfaces at both 100K and 300K. In a small range of strain (< 0.1), K_{23} compares well ($<$ 0.6% difference) for the perfect bonding cases, i.e. without temperature effect. For cohesive zone cases, K_{23} obtained from computational micromechanics demonstrates a lower value than the composite cylinder model results at both 100K (8% and 6% lower in the loading

and unloading regimes, respectively) and 300K (3% and 5% lower). This is attributed to the differences in RVEs such that in the composite cylinder model case, only the normal separation mode is active in calculating K_{23} whereas in the FEA case, both normal and sliding modes are active, with the sliding mode having a significantly lower stiffness. This observation points to the significance of mode mixity in the determination of the effective elastic properties, and hence, indicates that computational micromechanics approaches may be preferred.

Thus, in both the computational micromechanics and analytic composite cylinder method, lower K_{23} is observed for the cohesive zone case compared with perfect bonding case, and K_{23} 's dependence on applied load, temperature and volume fraction is observed. Based on the results, it is concluded that the interface load-transfer at room temperature may be much of the source of the over-prediction of the effective elastic material properties of CNT-polymer nanocomposites typically reported from micromechanics analysis.

3.5 Conclusions

Atomistic non-functionalized graphene-PE interface models have been constructed to characterize the load transfer capability at the interface between CNTs and a PE matrix in CNT-PE nanocomposites in terms of the force-separation response with respect to both normal and sliding modes using MD simulations. Bilinear cohesive zone laws were developed based on traction-separation interface responses for normal opening and sliding mode sepa-

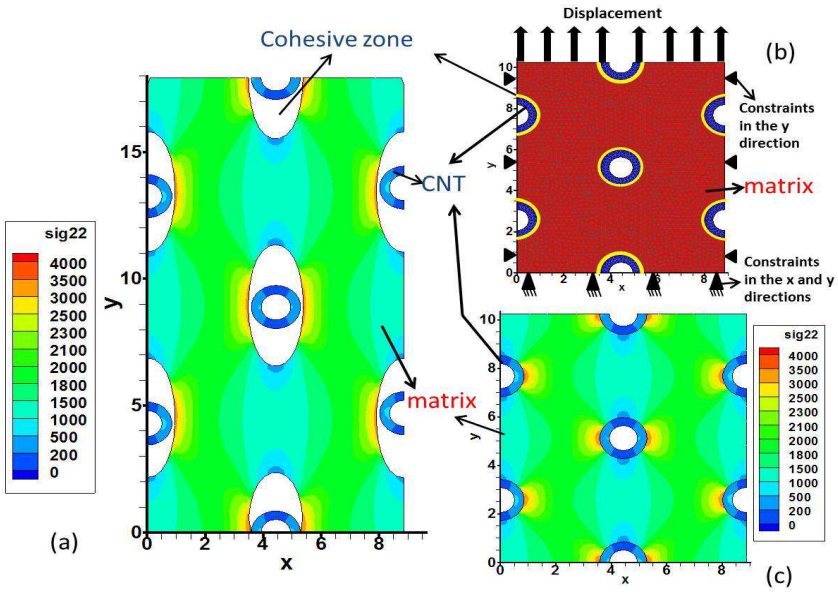

Figure 3.17: (a) shows deformation of computational RVE with the stress contour σ_{yy}(MPa) for Vf 0.1 CNT-PE nanocomposites under 0.75 strain loading and (c) the undeformed stress contour of σ_{yy} (MPa). (b) shows displacement loading condition and the boundary conditions used for C_{22} stiffness components caculation.

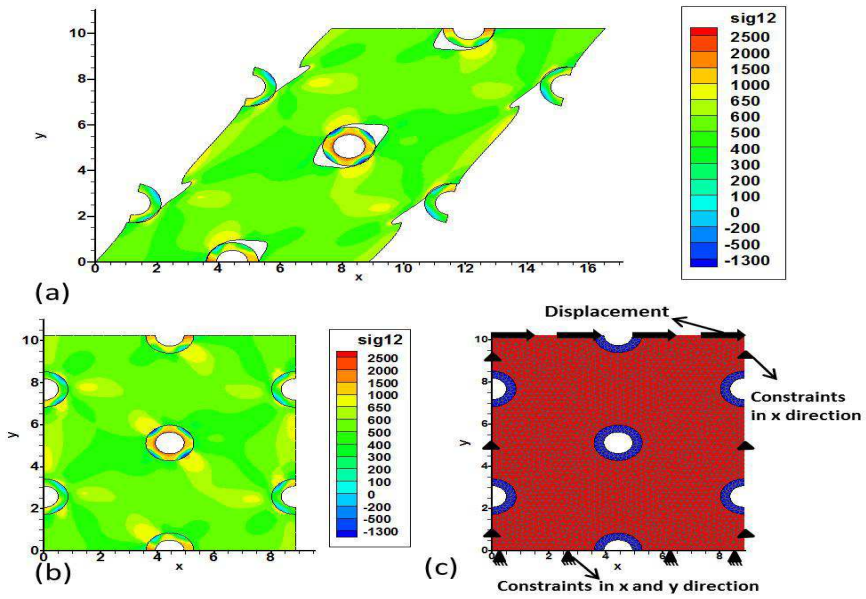

Figure 3.18: (a) shows deformation of computational RVE with the stress contour σ_{xy} (MPa) for Vf 0.1 CNT-PE nanocomposites under 0.75 strain loading and (c) the undeformed stress contour σ_{xy} (MPa). (b) shows displacement loading condition and the boundary conditions used for C_{66} stiffness components caculation.

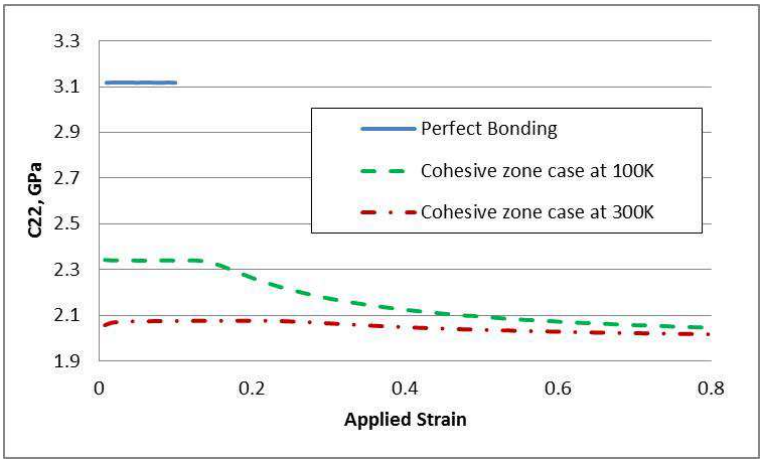

(a) C_{22}

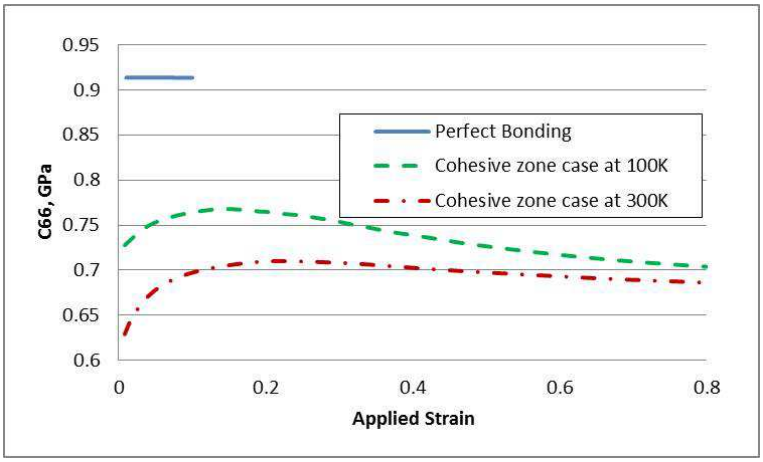

(b) C_{66}

Figure 3.19: Macroscale effective C_{22} and C_{66} stiffness components at 100K and 300K for 0.1 vf CNT-PE nanocomposites for perfect bonding and cohesive zone cases obtained from FEA-based computational micromechanics approach

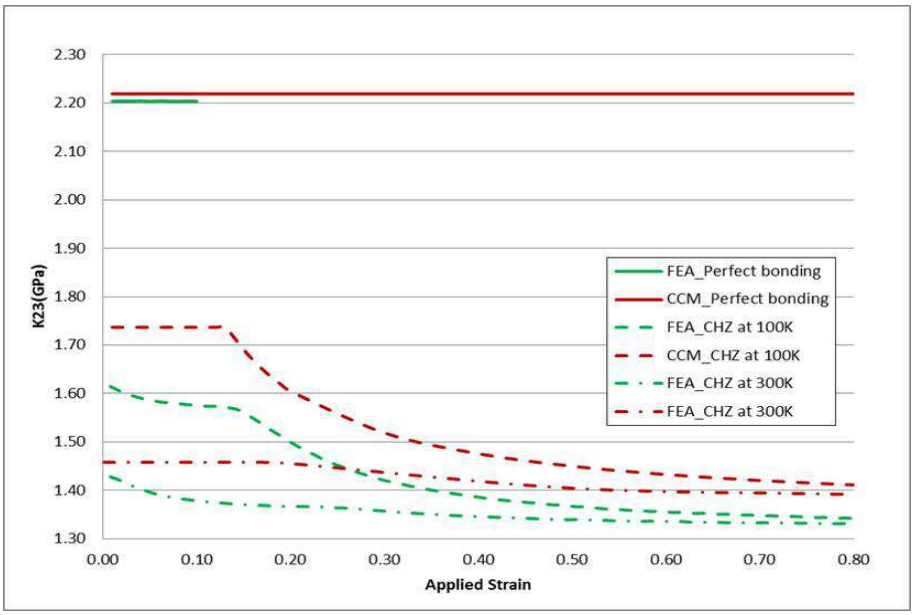

Figure 3.20: Macroscale effective K_{23} for CNT-PE nanocomposites with a CNT volume fraction of 0.1 for perfect bonding and cohesive zone cases from composite cylinder method and from FEA-based computational micromechanics approach

rations at the nanoscale. The cohesive zones were applied in the analytic and computational micromechanics approaches to assess the effect of the interface on the macroscale effective elastic properties.

The use of the graphene sheet in constructing a representative interface element has been explored in terms of sensitivity to parameters such as the length of the polymer chains, the number of polymer chains, and relative position of the MD 'grip' to the interface, as well as the influences of curvature of the graphene sheet and temperature. Based on the analysis, representative interface elements consisting of a flat graphene sheet and 10 polymer chains of 78 repeat unit chain length (i.e. the 10C80C) on the order of 2660 atoms provides acceptable results as the variances in key parameters such as the the peak force, separation energy, and

separation distance at given temperature did not lead to significant variance in the effective elastic property calculations. It was also observed that in general, the sliding mode peak force at 100K is much smaller (73% lower) than that of normal opening mode separation. It is observed that the peak force and separation energy decreased at 300K compared with 100K by as much as 69.5% and 73.0%, respectively, which indicates a weaker stiffness of interface for CNT-PE nanocomposites at higher temperature.

It was observed that the macroscale effective properties determined from the micromechanics approaches experienced significant depreciation compared to the perfect bonding cases when the interface model was included. This was observed to be the case both before and after the peak traction was obtained, with the latter also demonstrating strain dependent effective properties. The temperature sensitivity of the interface was observed to directly transfer to the effective property calculations, which were also observed to be highly sensitive to the CNT volume fraction. In short, the results show that the interface may be the source of overprediction of the material properties of CNT based nanocomposites.

Chapter 4

Characterization of nanoscale load transfer at the functionalized CNT-polyethylene interface using molecular dynamic simulation

4.1 Introduction

The covalent functionalization of CNTs is considered to be one of the most promising options for improving the load-transfer properties of the interface, as it can bind CNTs to the polymer chains during the polymerization [74]. Experimental results demonstrate significant

improvement of the performance of the CNT-polymer nanocomposites with functionalized interfaces with respect to the nanocomposites with pristine CNTs [75, 33]. Experimental efforts have sought to characterize the interface in CNTs-based nanocomposites [36, 31, 37]. Given the challenges associated with directly probing CNTs with extremely small size, only few experiments directly exploring the load transfer at the CNT-polymer interface in nanocomposites have been reported and the results exhibit wide variations [37]. In addition, it is extremely hard to investigate the bonding information of the interface between the CNTs and the polymer matrix experimentally. Hence, there is growing interest in and reliance on computational materials science techniques to study the interface between the CNTs and polymer matrix using atomistic simulation and/or continuum models [53, 54, 55]. However, limited studies has been conducted to characterize the functionalized interface between CNTs and the polymer matrix, which has covalent bonding interactions in addition to vdW interactions, in both sliding and normal mode separation. More work is needed to fully understand the mechanism behind the improvement of the mechanical properties of the nanocomposites due to the functionalization of the interface in order to help develop techniques for tailoring the interface aiming at producing the nanocomposites with required properties.

In this chapter, the functionalized CNT-PE interface is assessed in terms of both normal and sliding mode separations at the nanoscale by conducting classic atomistic MD simulations. A simple side chain with two PE monomers is adopted as functional groups. Special emphasis is placed on assessing the load transfer of the functionalized interface with various

functionalization densities in terms of force-separation responses of the graphene-PE interface in normal and sliding modes at a given temperature. Two force field potentials, CVFF and AIREBO potential, are applied to simulate the interactions between the atoms in the polymer matrix and the functional groups. CVFF potential is modified to allow the bond breaking and hence damage of the interface for the damage of the interface by introducing a strain energy criteria. Comparison of the two potentials is conducted by comparing the MD simulation results where it is found that two potentials give different force-separation responses, but that in both cases, there is significant increase in load transfer capability and toughness of the interface with increasing degree of functionalization of the interface. By including longer polymer chains in the amorphous polymer matrix, it is noted that the entanglements between the polymer chains can improve the efficiency of load transfer to the functional groups and the graphene sheet. It is anticipated that, as in [76], the force-separation responses of the functionalized nanoscale interfaces can be transferred to higher level continuum model for obtaining better prediction of the effective material properties of the functionalized CNT-polymer nanocomposites, which in turn may contribute to develop techniques of engineering the interface for producing the CNT-reinforced nanocomposites with better mechanical performance.

4.2 Description of Atomistic Potentials

The two potentials used in this paper for comparison purposes are the CVFF potential [60] and the adaptive intermolecular reactive empirical bond order(AIREBO) potential [63]. CVFF is properly calibrated for the carbon-carbon and carbon-hydrogen interactions and consists of four energy components which are associated with bond stretching, angle bending, torsion and non-bonded pairwise potential associated with van der Waals interaction as introduced above.

CVFF potential has been introduced in detail in Chapter III. The specific parameters of CVFF used in the present work are given in Table A.1. It is noted that the classical force field CVFF does not account for dissipation effects such as bond breaking. As it was anticipated that bond breaking would be a significant factor governing the ultimate load transfer capabilities of the functionalized interface, a strain energy based failure criteria for covalent carbon-carbon bonds was introduced to the CVFF potential in the present work, i.e.

$$E_b^i = K_b^i(r^i - r_0^i)^2 >= E_{criteria} \tag{4.1}$$

The strain energy criteria are draw from reference [77] and are applied to the potential energy of the covalent carbon-carbon bonds calculated by Equation 3.1. The stiffness of the covalent bonds is held constant, which means no degradation of the bonds before the bond breaking. The i^{th} covalent bond and the associating angles and dihedrals are broken once

Equation 4.1 is satisfied.

As an alternative to modifying the CVFF potential, one can make use of reactive force fields which have been developed to account for both bond breaking and bond formation during the MD simulation without having to concurrently consult computationally intensive quantum mechanics calculations. As it is parameterized for modeling condensed-phase hydrocarbon systems as well as the breaking and the formation of chemical bonds, the AIREBO potential is also considered herein in assessing the load transfer capabilities of the functionalized graphene-PE interface, the results of which are compared to the modified CVFF simulations. The AIREBO potential includes three energy components, the REBO potential, a torsional interaction potential and an intermolecular interaction potential. The function form for the REBO portion of the potential is given in Equation 4.2 as bellows, which involves repulsive $V_{r_{ij}}^{R}$ and attractive $V_{r_{ij}}^{A}$ pairwise parts as well as many-body terms b_{ij} which control the relative contribution of the two parts. The repulsive $V_{r_{ij}}^{R}$ and attractive $V_{r_{ij}}^{A}$ potentials depend on the atom types of the i^{th} and j^{th} atoms and the distance r_{ij} between them. The total REBO potential energy also depends on the local atomistic environment, i.e. the positions and types of atoms surrounding the $i-j$ bond, by introducing the bond-order term b_{ij}, which accounts for the chemical effects affecting the strength of covalent bonds.

$$E_{ij}^{REBO} = V_{ij}^{R}(r_{ij}) + b_{ij}V_{ij}^{A}(r_{ij}) \tag{4.2}$$

The torsional interaction potential of the AIREBO potential depends on the dihedral angles

formed by sets of four covalently bonded atoms and is given by,

$$E_{ijkl}^{tors} = w_{ij}(r_{ij})w_{jk}(r_{jk})w_{kl}(r_{kl})\epsilon[\frac{256}{405}cos^{10}(\frac{\phi}{2}) - 0.1] \tag{4.3}$$

where ϵ is barrier height, $w_{mn}(r_{mn})$ is a bond weight term between 0 and 1, which is based on the distance between m_{th} and n_{th} atoms.

The intermolecular interaction potential between two atoms are modeled with a weighted Lennard-Jones 12-6 potential given by Equation 4.4.

$$E_{ij}^{LJ}(r_{ij}) = S(t_r(r_{ij}))S(t_b(b_{ij}))C_{ij}V_{ij}^{LJ}(r_{ij}) + [1 - S(t_r(r_{ij}))]C_{ij}V_{ij}^{LJ}(r_{ij}) \tag{4.4}$$

where $S(t)$ is a universal switching function, $t_r(r_{ij})$ and $t_b(b_{ij})$ are scaling functions, C_{ij} is a connectivity switch function and $V_{ij}^{LJ}(r_{ij})$ has the same form as Equation 3.4.

Adaptive decisions about whether two atoms are experiencing the LJ interaction are made by using switching functions which generally dictate that two atoms have a LJ interaction when (1) there is no chemical bond between them and (2) they are not part of a dihedral(torsional) bond.

The total potential energy of the system is the summation of the three parts, the REBO, torsion and Lennard-Jones contribution in Equations 4.2, 4.3 and 4.4. It is noted that the individual contributions to the sum carry with them information regarding the local atomistic environment thereby allowing for changes in bond stiffness to simulate bond breaking and

forming in chemical reactions. All the specific parameters of AIREBO are from LAMMPS.

$$E = \frac{1}{2}\sum_{i}\sum_{j\neq i}[E_{ij}^{REBO} + E_{ij}^{LJ}(r_{ij}) + \sum_{k\neq i,j}\sum_{l\neq i,j,k} E_{ijkl}^{tors}] \tag{4.5}$$

Both the modified CVFF and AIREBO potentials are attempting to capture the interaction associated with bond stretching, angle bending, torsion rotation and non-bonded vdW potentials. However, different functional forms and parameterizations are developed for the two potentials, which can lead to differences in the assessment of the load transfer across the graphene-PE interface. No reformation of the broken bonds is allowed in the modified CVFF, which is different from the AIREBO potential.

4.3 Molecular model

In order to capture the detailed information at the atomic scale, the fully atomistic structure of the polymer chain, i.e. keeping information about the interactions between each single atom, was modeled in the present work. PE monomer, which has one sp^3 hybridized carbon atom and two hydrogen atoms, is used to construct long polymer chains comprised of several $-CH_2-$ repeat units and capped at each end with a $-CH_3$ unit such that the PE chain can be expressed as $CH_3-(CH_2)_n-CH_3$. In this research, the amorphous PE structure consists of 10 polymer chains with 78 monomers per chain($CH_3-(CH_2)_{78}-CH_3$) for a total of 2660 polymer atoms in the system. The interactions between all atoms in the chains are modeled

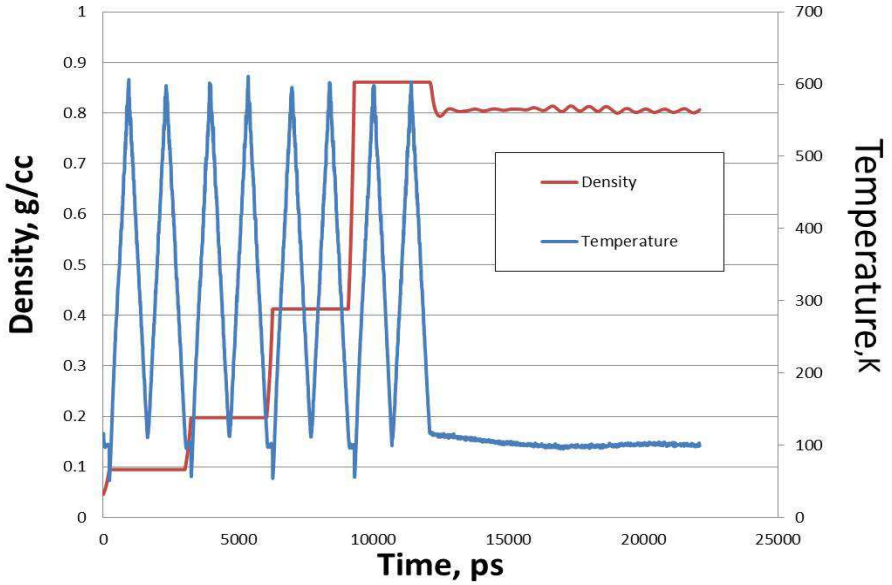

Figure 4.1: The change of density of the amorphous PE matrix and temperature of the simulation system in the preparation process of the amorphous PE polymer using the AIREBO potential

using either only the CVFF or only the AIREBO potential with parameters corresponding to specific bond, angle and dihedral types, see for example the parameters provied in Table A.1. All MD simulations were performed using LAMMPS. MD simulations are first conducted to prepare the equilibrium amorphous polymer structure at the desired temperature by following the same procedure described in [76] wherein an initial chain arrangement is put through a sequence of volume reduction and temperature annealing processes before being allowed to relax to the final amorphous structure. The final density of the amorphous PE is around 0.93 g/cm^3 for using CVFF potential and 0.81 g/cm^3 for using AIREBO potential as shown in Figure 4.1 with nominal values for PE obtained from experiments reported in the range of 0.88 to 0.94 g/cm^3. A flat graphene sheet was constructed to be 24Å by 23Å

in planar dimensions and is composed of 240 sp^3 hybridized carbon atoms located at their equilibrium positions within the hexagonal structure, with the interaction between atoms in the graphene sheet described by CVFF potential regardless of whether the polymer is modeled with CVFF or AIREBO.

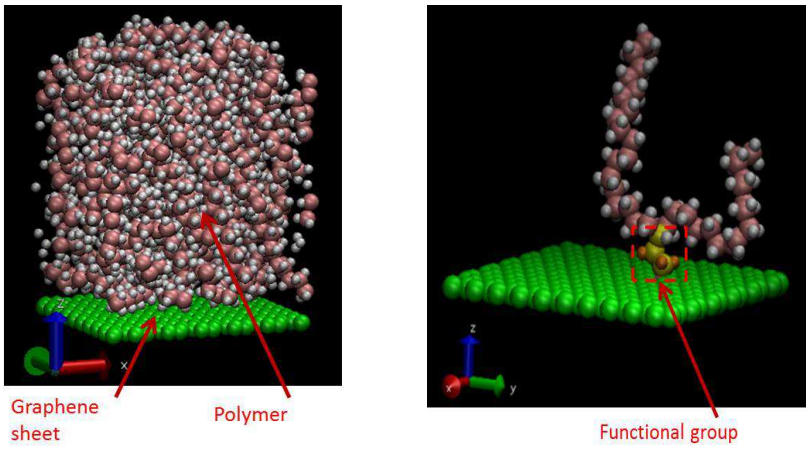

(a) (b)

Figure 4.2: (a)The non-functionalized representative interface element for the graphene-PE interface. (b)The functionalization of the graphene-PE interface by grafting the functional group between the graphene and the polymer chain through covalent carbon-carbon bonds indicated by the red rectangle. Non-functionalized polymer chains are made transparent to highlight the functionalized chain.

A non-functionalized interface model for the CNT-PE nanocomposite was constructed by introducing the flat sheet of graphene to the amorphous PE structure oriented in x-y plane at z=0 with some prescribed distance prior to minimization as shown in Figure 4.2(a). The flat graphene is considered to possess similar local morphology as CNTs, and is adopted to represent the normal and sliding mode force-separation response of the CNT-PE interface for CNTs having variable radii as discussed in [76]. With periodic boundary conditions in the x- and y-directions and non-periodic conditions in the z-directions, energy minimization

at 0K and subsequent dynamic equilibration at 100K were conducted to allow the perfect wetting of the polymer to the graphene sheet and establish the equilibrium distance between them in the non-functionalized graphene-PE interface model as discussed in [76].

One of the major approaches to improve the load transfer in CNT-polymer nanocomposites is to form covalent bonds between the polymer matrix and the sidewalls or end caps of nanotubes [74]. Side chains with two CH_2 monomers are usually adopted as functional group [54, 52] for CNT-PE nanocomposites, which are also used here and are grafted between PE chains and the graphene sheet through carbon-carbon covalent bonds as shown in Figure 4.2(b). The functionalization process used the prepared equilibrated nonfunctionalized graphene-PE interface models as the initial configurations and have all atoms in the interface model frozen in their spacial position during the process of adding functional groups. The location of the functional group, i.e. which pair of carbon atoms (having one in the graphene sheet and the other in the polymer chains) are grafted to form the functional groups, is largely governed by the distance of the paired carbon atoms. The functional group is added and grafted between the paired carbon atoms having the minimum distance, with subsequent functional groups also constrained to be at least 2Å away from the already grafted functional groups. With the desired number of functional groups grafted, further dynamic equilibration under NVT ensemble (constant volume and constant temperature) is conducted for about 100 ps in order to establish equilibrium distance between the graphene sheet and the amorphous polymer with the addition of functional groups. The resulting atomistic structures produced are thus taken as the representative interface elements for

further simulations studying the normal and sliding mode load transfer.

4.4 Characterization of the functionalized representative interface element at the nanoscale

4.4.1 Normal Opening Mode Separation

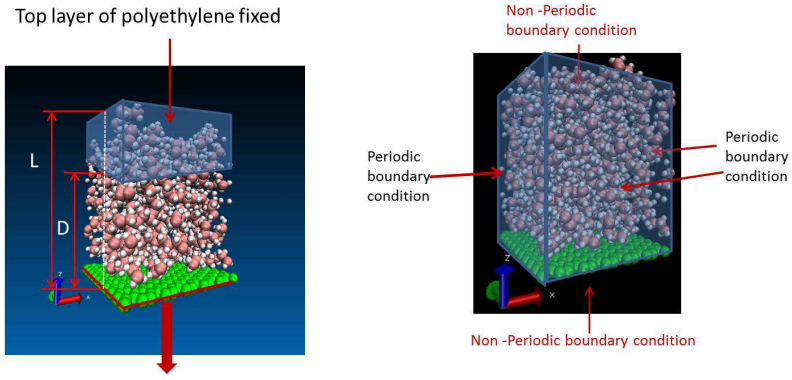

(a) (b)

Figure 4.3: (a) shows constraints with the arrow indicating the direction of the velocity on graphene sheet. (b) shows boundary conditions for representative interface element (10c80c case) in normal mode separation.

In order to conduct force-separation studies for normal mode load transfer using the representative interface element, a region of the polymer at the top has been frozen, i.e. is fully constrained to simulate a grip as shown in figure 5.7(a), while the graphene sheet was displaced in the z-direction through a uniform application of a displacement of 0.000025 nm per time step (typically 0.1 fs) until full separation was achieved. Periodic boundary conditions were applied in the x- and y-directions such that the interface can be effectively taken to be

repeated (i.e. infinite) in the x- and y-directions as shown in figure 5.7(b). Throughout the simulation, the temperature was fixed at 100K under a NVT ensemble. The normal force on each carbon atom in the graphene sheet (240 carbon atoms) over 4 ps (which corresponds to 40,000 time steps) is averaged and combined with the displacement of the graphene sheet in order to obtain the force-separation response as discussed in [76]. The bond energy E_b of the breakable carbon-carbon covalent bonds in the polymer and functional groups, which is calculated by Equation 3.1, is checked every 17,000 simulation time steps. When the bond stretching energy of one carbon-carbon covalent bond reaches the value of the strain energy failure criterion as in Equation 4.1, this bond is disconnected and the associated angles and dihedral are deleted. After the deleting of the broken bonds, angles and dihedrals is done, the interfacial system is equilibrated for a short time (typically 700fs) under a NVT ensemble. No reforming (i.e. rebonding) is allowed for the broken bonds, which mean no reconnection of the atoms in the broken bonds if by chance they come back to be within close proximity.

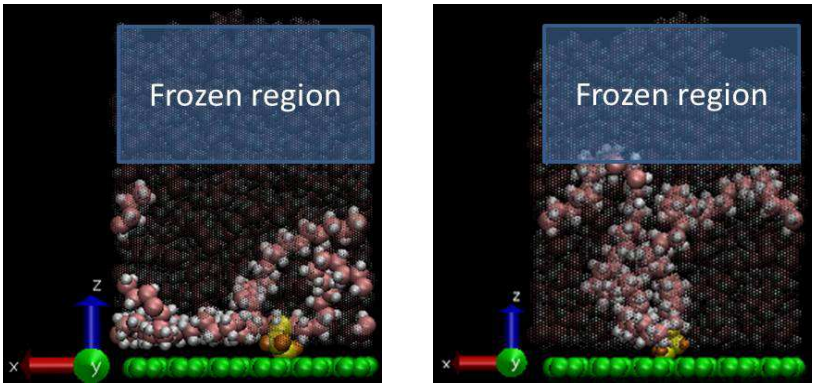

(a) (b)

Figure 4.4: Two representative interface elements with one functional group having different gripping conditions. (a) shows the case with the free functionalized polymer chain. (b) shows the case with the gripped functionalized polymer chain

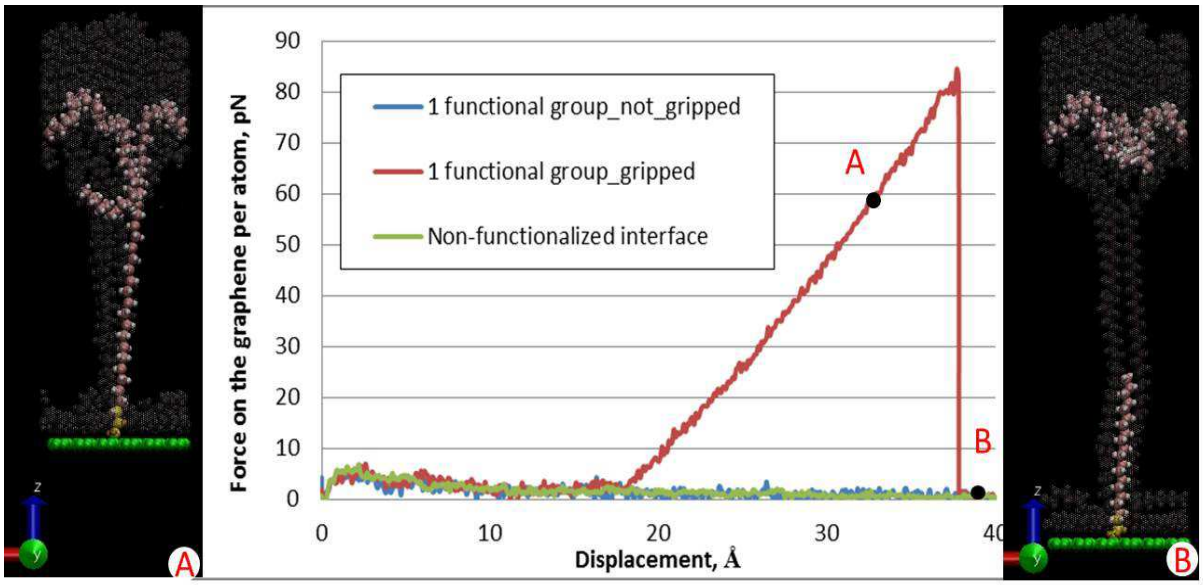

(a)

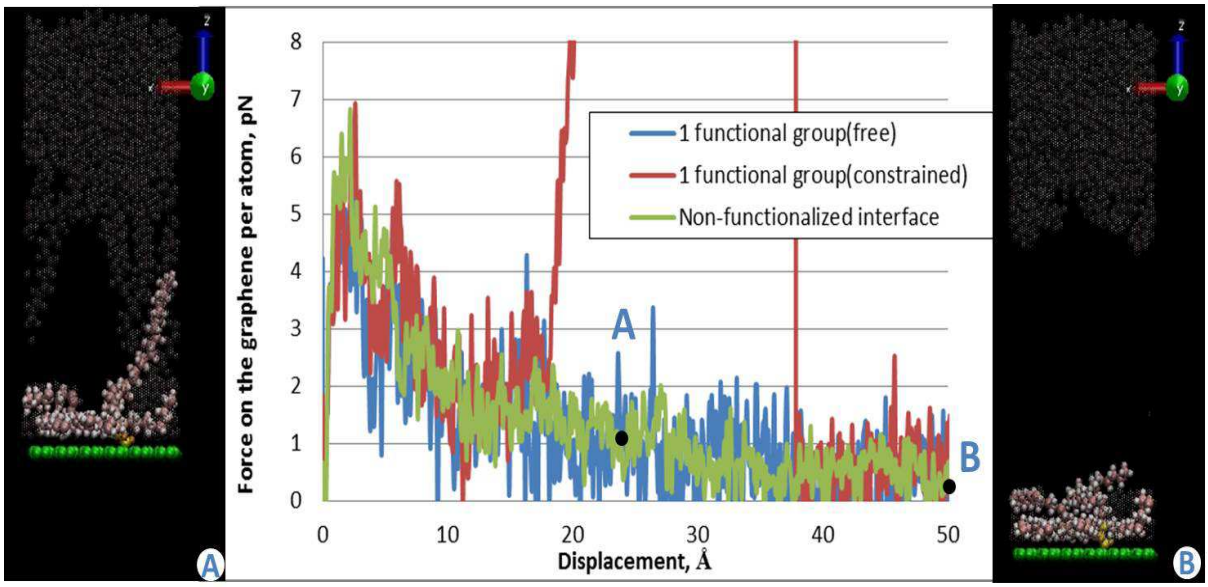

(b)

Figure 4.5: (a) gives the comparison of the force-separation responses in normal opening separation for the non-functionalized interface to that of the functionalized interfaces with 1 functional group case (one has the functionalized polymer chain gripped and the other does not). (b) shows the zoom in picture of (a). The inserts in (a) show the snapshots of the functionalized interface model with 1 functional group on a gripped functionalized polymer chain during the normal mode separation corresponding to the points labeled in the force-separation response. The inserts in (b) give the snapshots of the functionalized interface model with 1 functional group on a free functionalized polymer chain during the separation.

It is noted that the process of generating the functionalized representative interface elements can lead to functional groups which are grafted to polymer chains whose tortuosity places the majority of the chain in close proximity to graphene interface or can just as easily result in grafting to polymer chains who extend long distances away from the graphene interface. Figure 4.4 shows the representative interface elements for the two cases with different gripping conditions. One has local tortuosity such that the functionalized polymer chain totally free from the frozen region(4.4(a)). The other has the functionalized polymer chain with more diffuse tortuosity such that part of the chain is captured in the frozen region as shown in Figure (4.4(b)). Figure 4.5(a) shows normal mode force-separation responses for the representative interface elements with 1 functional group using the modified CVFF with the failure criteria demonstrating the two different gripping conditions in comparison to the non-functionalized representative interface element. It is noted that the force-separation response for the case with free functionalized polymer chain is almost identical to that for the non-funcitonalized representative interface element in Figure 4.5(b), which means there is little or no increase in efficiency of load transfer attributed to the functional group taking place before the disentanglement of the polymer chains. With the funcitonalized polymer chain actually "gripped" in the frozen region, huge increases are observed in the peak force (increased about 10 times) and separation energy (increased about 55 times) of the force-separation response of the functionalized representative interface element relative to the nonfunctionalized representative interface element. An immediate drop of the force is also observed for the case with the gripped functionalized polymer chain denoting a huge

and sudden degradation of the load transfer ability of the interface which can be seen to correspond to the bond breaking in the functionalized polymer chain during the separation as shown in the inserts in Figure 4.5(a).

4.4.2 Normal Mode Force-Separation Studies

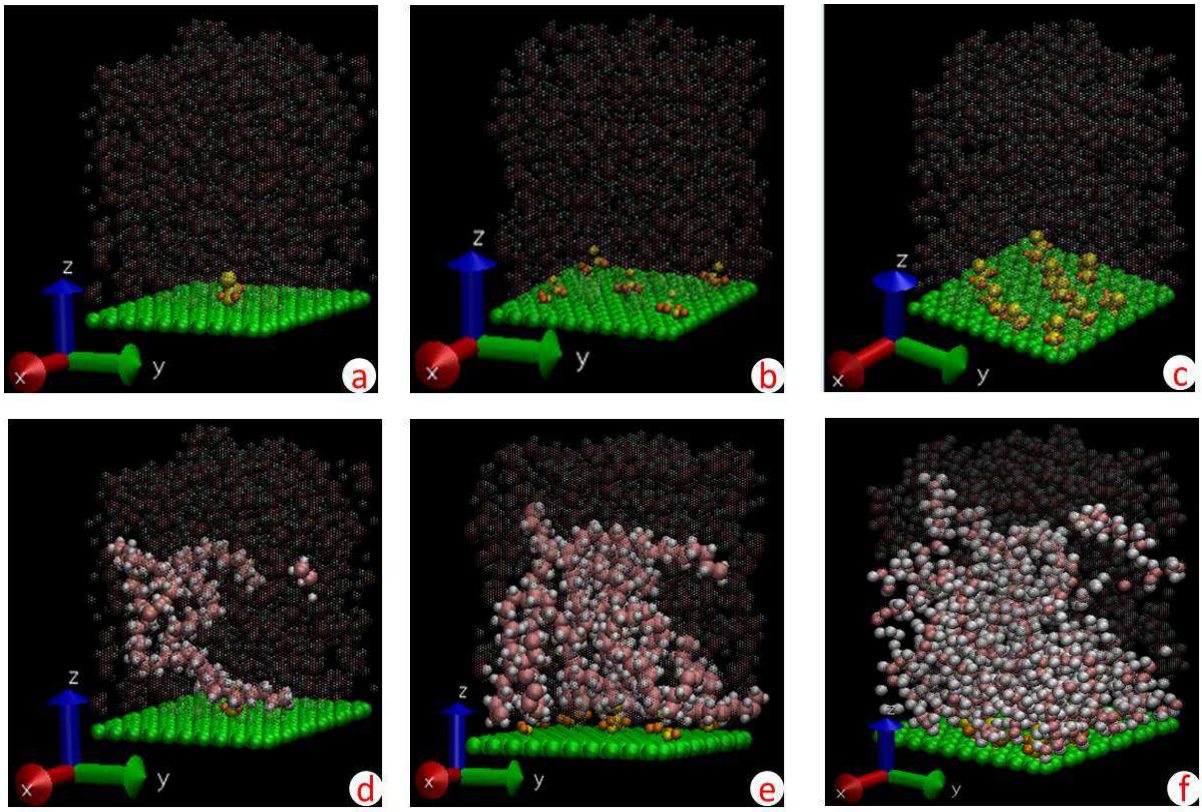

Figure 4.6: The functionalized representative interface elements with 1, 5 and 10 functional groups for the normal separations using modified CVFF. (a) to (c) show the location of the functional groups. (d) to (f) show the functionalized polymer chains where the functional groups are grafted.

Two sets of functionalized graphene-PE representative interface elements with 1, 5 or 10 functional groups are shown in Figures 4.6 and 4.7 for normal opening separation simula-

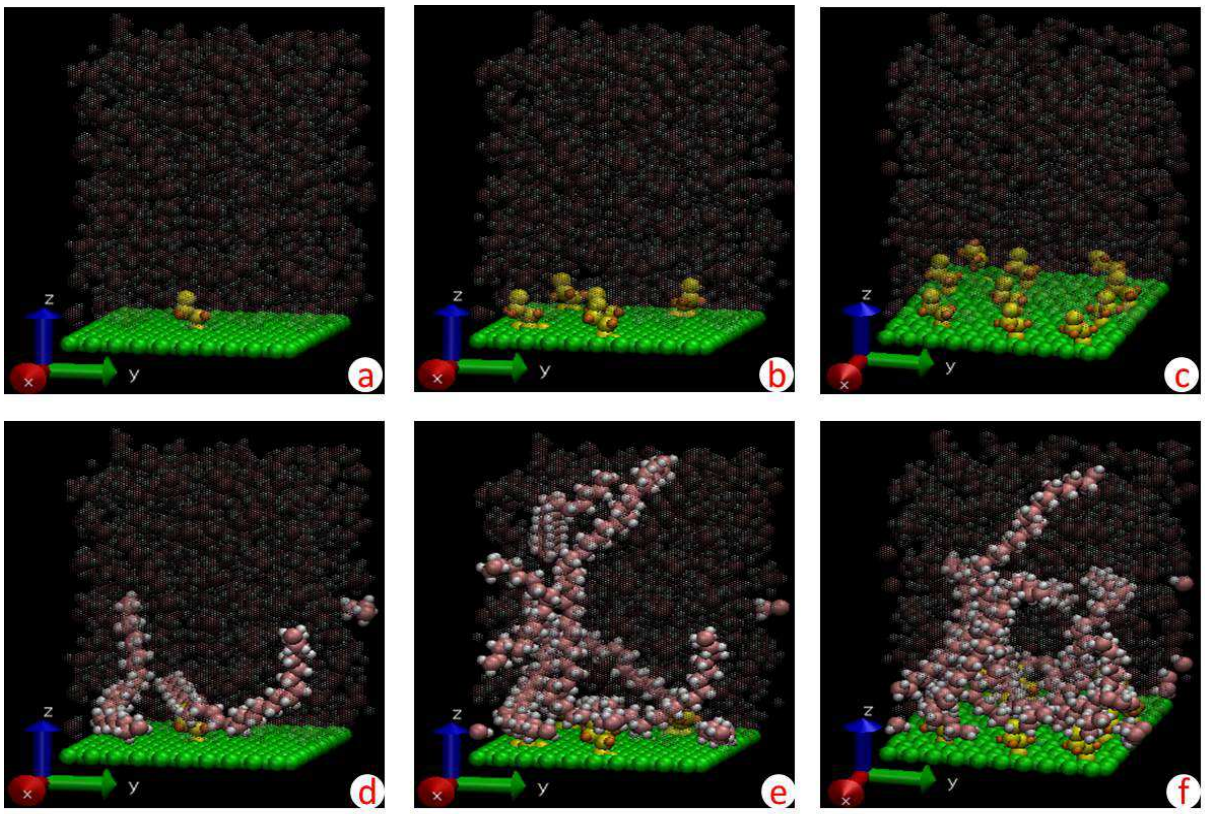

Figure 4.7: The functionalized representative interface elements with 1, 5 and 10 functional groups for the normal separations using AIREBO. (a) to (c) show the location of the functional groups. (d) to (f) show the functionalized polymer chains where the functional groups are grafted.

tions obtained using the modified CVFF and AIREBO potentials, respectively. In order to observe the sensitivity of the force-separation response to the location(s) of the functional group(s), equilibrium non-functionalized graphene-polymer interface models with different initial configurations are used for preparing the functionalized representative interface elements of the modified CVFF and AIREBO cases. Each set of functionalized representative interface elements with 1, 5 or 10 functional groups is prepared by adding functional groups consistently to the same initial non-functionalized interface model following the functionalization process described above. For example, to create Set 1, one functional group is added to an equilibrium non-functionalized interface model followed by four more functional groups to generate the 5 functional groups case for Set 1, followed by an additional 5 functional groups to sequentially generate the 10 functional group case of Set 1. The sequential addition of functional groups is applied to two different initial non-functionalized interface models to create Sets 2 and 3, for a total of 18 functionallized interface model realizations(9 for modified CVFF and 9 for AIREBO). In Figure 4.6 and 4.7, (a)-(c) show the locations of functional groups on the graphene sheet for Set 1 while (d)-(f) also highlight the polymer chains wherein the functional groups are grafted.

Typical force-separation responses for a 5-functional-group modified CVFF and 5-functional-group AIREBO Set 1 interface models are provided in Figure 4.8 along with their respective non-functionalized interface responses. Generally, the force-separation responses are observed to have three regions for most of the functionalized representative interface elements as labeled in Figure 4.8. In the first region, an initial monotonically increasing loading of the

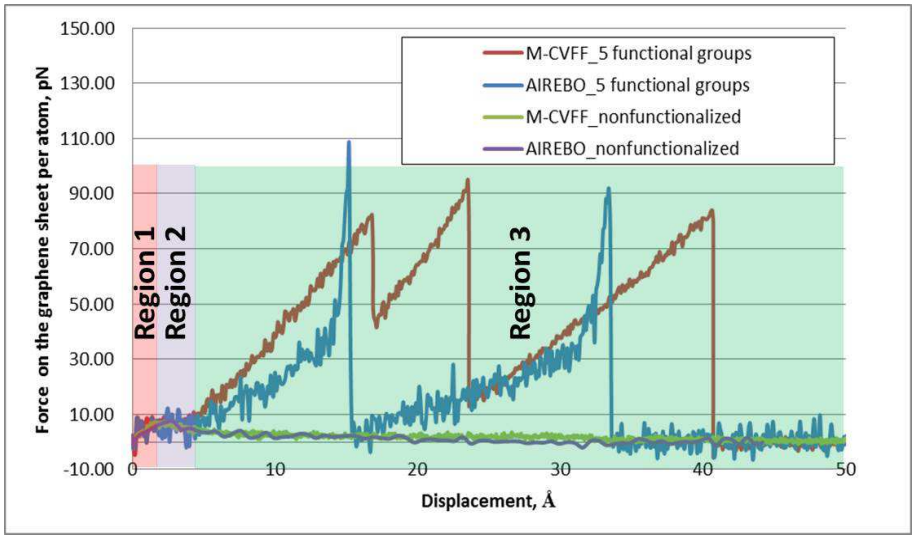

(a)

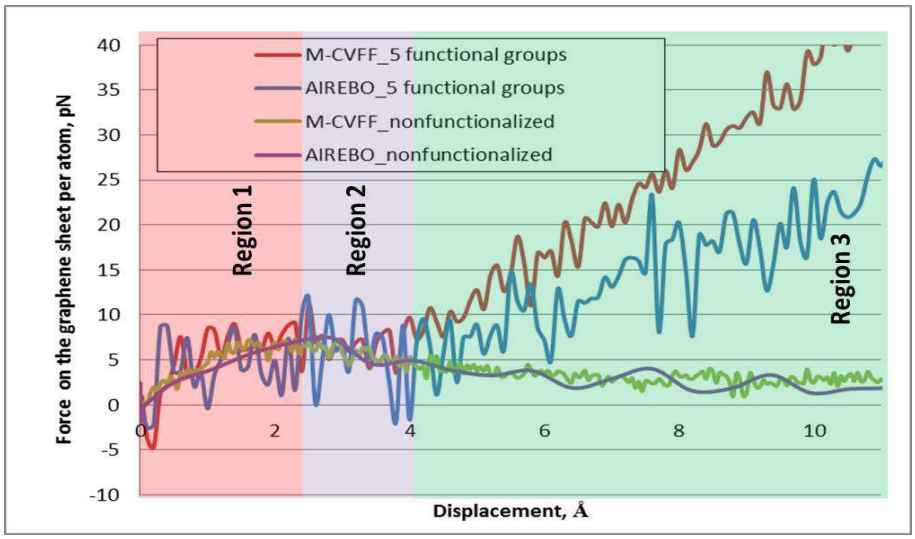

(b)

Figure 4.8: The force-separation responses for the functionalized interface models with 5 functional groups in the normal mode separations using different potentials, M-CVFF vs AIREBO. The three regions of the force-separation responses are labeled in (a) and (b) corresponding to the initial elastic monotonically increasing loading in Region 1, the stable loading in Region 2 and the saw-toothed loading and unloading segments in Region 3. The first regions are zoomed in to compare with the loading region of the force-separation response for the non-functionalized interface model.

interface is observed which is similar to the load build up observed in the non-functionalized representative interface elements. This loading region is believed to be associated with initial polymer chain stretching and is dependent on both the entanglement and the strength of the non-bonded van der Waals interactions more than the covalently bonded functional group. In the second region, the loading stabilizes for a brief period where the force plateaus or even slightly decreases. It is believed this region of the force-separation response is associated with disentanglement of the polymer chains as again it closely mirrors the response of the non-functionalized interface. Region 3 of the force-separation response is denoted by sharp and steady increases in the loading relative to region 2. This region's behavior is believed to be directly attributed to the covalent bonding of the functional groups in combination with the long range chain interactions, i.e. sliding, locking, and disentangling of the functionalized chain(s), and is further characterized by large peak forces followed by sharp drops denoting the failure of covalent bonds associated with the functional groups or functional chains (recall that both the functional group and the polymer chains are modeled with the same potential so that bond breaking can and does occur in either location). Such an assessment is based on the observation that the non-functionalized interface demonstrates a steady decrease in the force-separation response until complete interface separation and that following the peak load drops, the functionalized response returns to force values similar to those of the non-functionalized interface until sufficient additional disentanglement takes place so as to engage other functional groups (if there are any remaining), yielding a saw-toothed pattern commonly associated with stick-slip phenomena observed in mode-I, e.g. double cantilever

beam and compact tension, fracture toughness testing [78, 79, 80].

Though the general behavior of the functionalized interfaces are consistent, there is a large degree of variation in specific behavior and quantifiable metrics between interfaces having differing number of functional groups and even between realizations with the same number of functional groups. For example, for the modified CVFF interface force-separation responses provided in Figure 4.9, some cases (1 functional group case in set 2 and set 3, the 5 functional groups case in set 1 and 2 and the 10 functional groups case in set 2) have what would be identified as a much broader region 2 response (extending to as much as 35 Å) before transitioning to region 3 as in these cases the entanglements of the functionalized chains are such that a significant level of sliding and disentanglement must occur before the functional group begins to carry load. In contrast, with less entangled functionalized polymer chains, some cases (5 functional groups case in set 3 and 10 functional groups case in set 1 and set 3) have the force consistently increase after the peak force of the initial loading region. For the 1 functional group case in set 1, the functionalized polymer chain is virtually straight in the initial configuration and has essentially no entanglement for the segment of the polymer chain which is not contained within the frozen region. As a result, the functional group is almost immediately engaged as a load carrying segment such that regions 1 and 2 are hardly discernible.

For the AIREBO interface force-separation responses in Figure 4.10, similar behaviors are observed in the three regions. The first and second regions are hardly discernible in the cases of set 1 as the functional groups tended to carry load immediately with little entangled

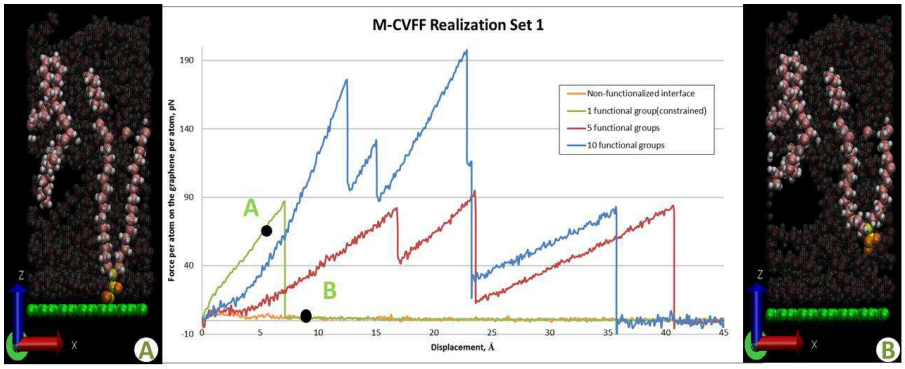

(a)

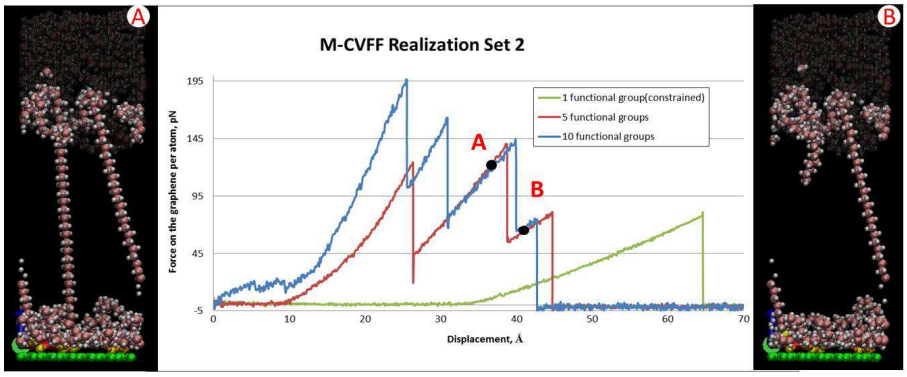

(b)

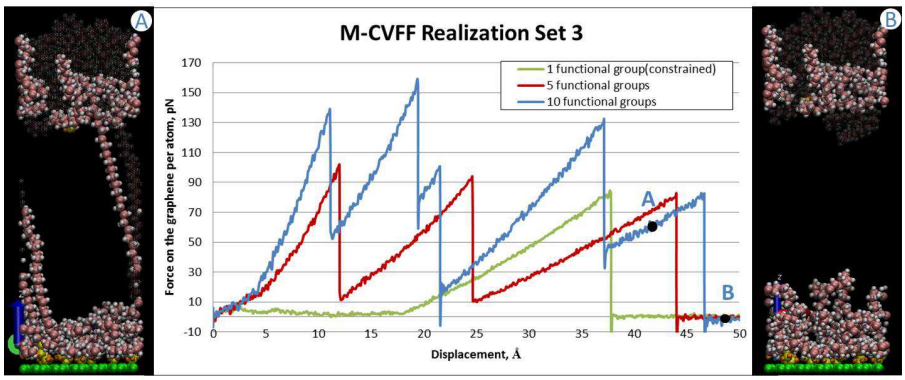

(c)

Figure 4.9: Bond breaking CVFF force-separation responses for the functionalized representative interface elements with 1, 5 and 10 functional groups. Snapshots are shown for the normal mode separations, which are corresponding to the points labeled in the force-separation responses.

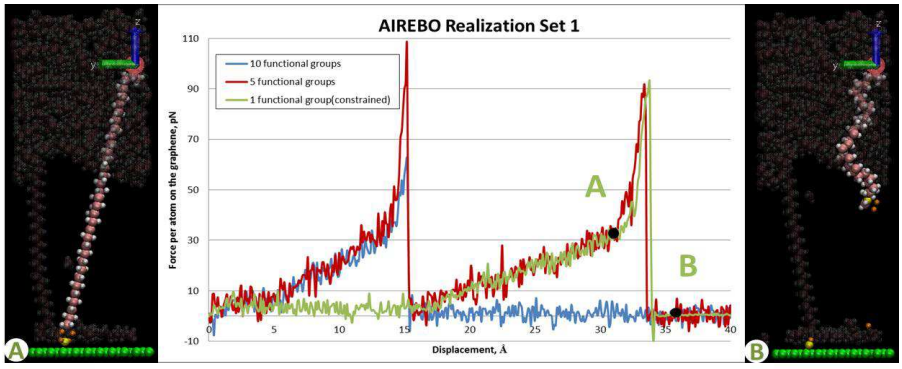

(a)

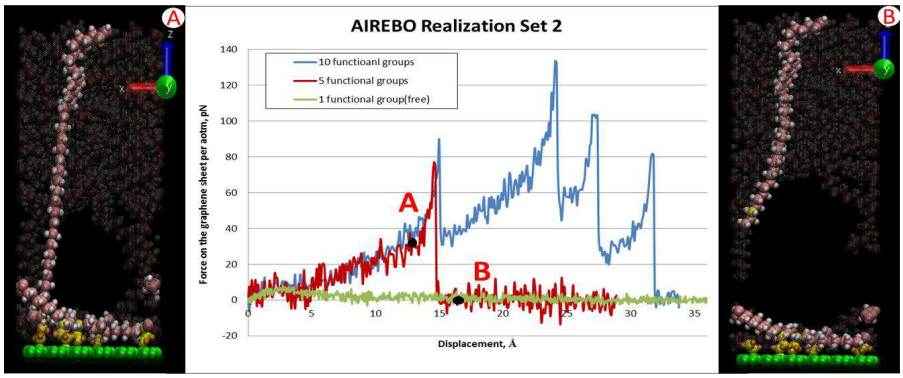

(b)

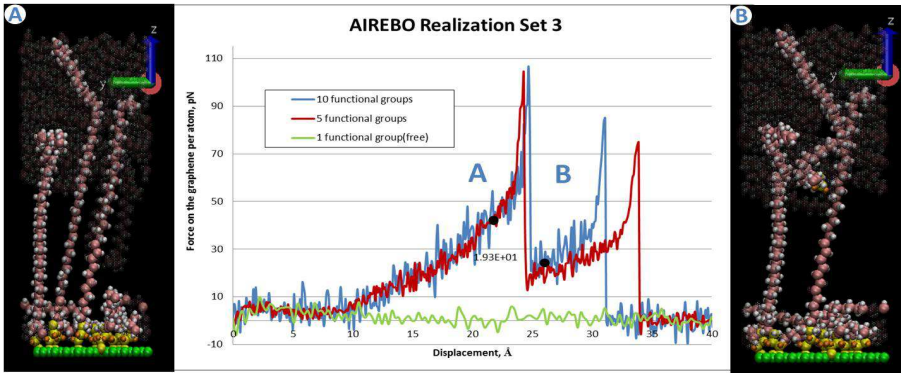

(c)

Figure 4.10: AIREBO force-separation responses for the functionalized representative interface elements with 1, 5 and 10 functional groups. Snapshots are shown for the normal mode separations, which are corresponding to the points labeled in the force-separation responses.

functionalized polymer chains. For the cases in set 2 and 3, the first regions demonstrate an similar initial loading region as observed for the non-functionalized representative interface elements. The second regions in the cases of set 2 are noted to be much narrower than these in the cases of set 3 (4Å vs 7.5Å), which indicates more efficient load transfer from the polymer to the functional groups because of less entanglements of the functionalized polymer chains in set 2 cases.

It is noted that in the third regions of both the modified CVFF and AIREBO interfaces, the force-separation responses demonstrate saw-toothed shapes with a sequence of loading and unloading segments which correspond to the breakage of bonds in the functionalized polymer chains and the subsequent load redistribution during the separation. As was demonstrated for single functional group cases, the grafted chain may be completely outside of the grip region (free) or may be partially contained within it (constrained). For interfaces having multiple functional groups, it is similarly observed that some of the grafted chains are free and others are constrained resulting in a mixture of the two responses observed in Figure 4.5(a) in Figures 4.9 and 4.10. The normal opening mode separation simulation for the non-functionalized representative interface element has been conducted with breakable covalent carbon-carbon bonds in the polymer matrix. No bond is found to break during the normal mode separation of the non-functionalized interface model, i.e. though bonds can break, disentanglement is preferred. It is noted that bond breaking has only been observed for the carbon-carbon bonds in the constrained functionalized polymer chains, which implies only disentanglements of the PE chain does not lead to bond breaking. Therefore the number

of local peak forces in the third region does not necessarily equal the number of functional groups in the interface model, but does equal the number of broken bonds and equal or less than the number of functionalized polymer chains which are constrained (as in the 1 functional group case in set 1). For the cases having additional local peak forces in their force-separation response, the area under the curve which corresponds to the separation energy is greatly increasing. From the energy point of view, it implies that the interface becomes stronger with more functional groups grafted between the graphene sheet and the amorphous polymer implying greater possibility of efficient load transfer at the interface.

While saw-toothed shape has been observed in the third region of the force-separation responses for the modified CVFF case and for the AIREBO case, the M-CVFF case exhibits a nearly linear response in its loading regions while the AIREBO case exhibits more of an exponential response in its loading region. As shown in Table 4.1, comparing with the AIREBO cases, the modified CVFF cases demonstrate comparable but higher averaged peak force in the normal mode separation. As for the separation energy in Table 4.2, which is the area under the force-separation responses, the modified CVFF cases demonstrate much higher average values relative to the AIREBO cases (4, 3.5 and 4.2 times for 1-, 5-and 10-functional-group case, respectively). From the energy point of view, it implies that the interface model simulated using the M-CVFF potential with the strain energy failure criteria appears to be stronger than that simulated using the AIREBO potential.

Generally, each peak force and subsequent reloading in the third region of the force-separation responses is associated with the breaking of one functionalized polymer chain as shown in

the insets of Figure 4.9 and 4.10. As the constrained functionalized polymer chains can be considered as springs with varying stiffness connecting two rigid plates in parallel as shown in Figure 4.11, given the use of displacement control in normal opening mode separation, the effective stiffness $k_{eff} = k_1 + k_2 + k_3$. As seen in Figure 4.9 for the M-CVFF cases, the slope of each loading segment in the third regions is noted to be reducing relative to the previous loading segment. As the slope of the loading segments in the third regions can be seen as the stiffness of the functionalized interface, it indicates that the stiffness of the interface decreases with the increase in broken functionalized polymer chains as k_{eff} decreases with the elimination of k_n where n could be 1, 2 or 3. With the exception of the 1 functional group case in Set 1, it is observed that first loading segments of the third regions are the steepest for the 10 functional group case, with the 5 functional group case the second steepest and the 1 functional group case the third. This indicates that adding increasing number of functional groups at the interface helps to increase the initial stiffness of the functionalized interface when using the modified CVFF. One exception is the 1 functional group modified CVFF case in set 1 as shown in Figure 4.9(a) with one functional group grafted to the middle of one constrained polymer chains by the grip on its two ends, which leads to the obtained peak force corresponding to the simultaneous breaking of two functionalized polymer chains. Along with increases in peak forces and slopes of the force-separation response, in Table 4.2 it is noted that the separation energy has been significantly increased (more than an order of magnitude) with the addition of increasing numbers of functional groups when using the modified CVFF force field. Therefore, as for the modified CVFF cases, it can be concluded

that with more functional groups, the interface tends to be stronger in both stiffness and strength as indicated by the sharper initial loading segment in the third region of the force-separation responses and the separation energy.

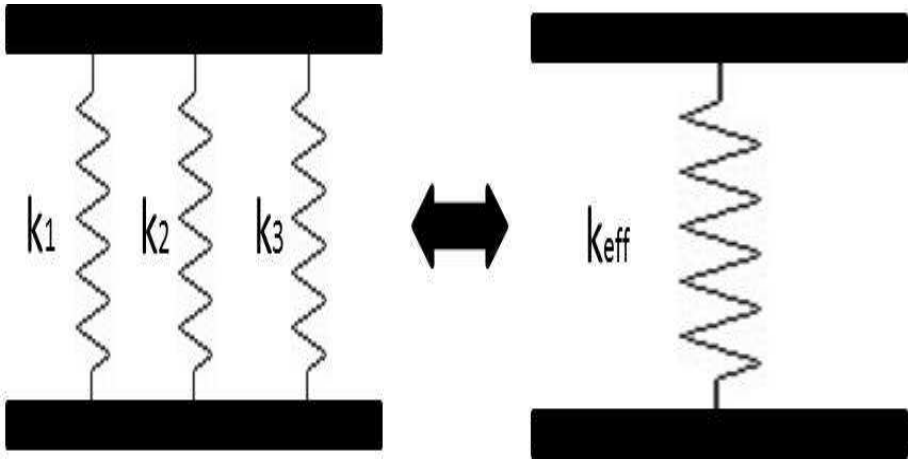

Figure 4.11: The schematic pictures for calculating the effective stiffness of the functionalized interface

As for the AIREBO cases in Figure 4.10, for the cases with multiple peak forces in the force-separation responses, the slopes of the loading segments in the third region does not have been observed to decrease with the increasing number of broken functionalized polymer chains. With increasing number of functional groups, an increasing of averaged separation energy and averaged peak force have been observed. However, the increasing is much lower than that observed in the modified CVFF cases. This is believed to be attributed to several reasons. One reason may be that as the density of the amorphous PE prepared using the AIREBO potential is much lower than that prepared using the modified CVFF potential (0.81 g/cm^3 vs 0.93 g/cm^3), the denser polymer matrix results in more atoms interacting between the graphene sheet and the polymer matrix. As different initial equi-

Table 4.1: Overall Peak force (pN) during the normal mode separation for 10c80c and 10c300c cases. N indicates the number of functional groups in the representative interface elements.

Potential	N	10c80c Set 1	Set 2	Set 3	Average	SD	10c300c Set 1
CVFF	0	5.4	-	-	-	-	7.5
	1	87.1	77.5	82.6	82.4	4.80	10.0
	5	90.0	139	100	109.67	25.89	95.6
	10	197	196	159	184	21.66	226
AIREBO	0	4.2	-	-	-	-	-
	1	101	6.9	6.3	38.0	54.50	-
	5	107	81.9	110	99.6	15.43	-
	10	80.0	134	110	108	27.06	-

librium non-functionalized graphene-polymer interface models have been used for preparing the functionalized representative interface elements, the spacial configurations of resulting representative interface elements are quite different in terms of the location of the functional groups and the length and tortuosity of the functionalized polymer chains as shown in Figure 4.9 and Figure 4.10. It is observed that the AIREBO potential cases have much fewer polymer chains involved in the functionalization. In addition, the strain energy failure criteria defined for bond breaking in the modified version of the classical force potential CVFF is only dependent on the distance of two direct covalently bonded atoms, while for the AIREBO potential out of equilibrium angles or dihedrals can also result in the breaking of associating covalent bonds, which implies that it is easier to break functionalized polymer chains in AIREBO potential cases.

The relative small size of 10c80c case leads to the question as to whether there are too few strong entanglements to result in the bond breaking without constrained functionalized poly-

Table 4.2: Separation energy (mJ/m^2) for 10c80c and 10c300c cases. N indicates the number of functional groups in the representative interface elements

Potential	N	10c80c Set 1	Set 2	Set 3	Average	SD	10c300c Set 1
CVFF	0	277	-	-	-	-	416
	1	1,580	4,740	3,610	3,310	1,601	2,760
	5	7,560	9,840	7,930	8,443	1,224	21,400
	10	12,200	14,300	13,500	13,300	1,015	42,100
AIREBO	0	121	-	-	-	-	-
	1	1,980	205	293	826	1,000	-
	5	3,030	1,110	3,100	2,413	1,129	-
	10	1,200	5,340	3,030	3,190	2,075	-

mer chains. To answer this question, functionalized representative interface elements with 10 polymer chains and 298 monomers per chains (10c300c) having larger dimension in the z-direction are adopted to reduce the influence of frozen boundary condition and introduce more entanglements as indicated by the increase in tortuosity reported in [76]. The resulting normal mode force-separation responses are shown in Figure 4.12. Without the functionalization, a clear graphene sheet as shown in inset (C) in Figure 4.12 is observed after the separation as the strong entanglements inside the amorphous polymer prevents the polymer chains from readily slipping past one another. Having one functional group attached to an unconstrained (free) functionalized polymer chain is observed to have the initial loading and unloading response mirroring the force-separation response of the non-functionalized interface and yield a similar overall peak force, which indicates that the entanglements in the polymer matrix of 1 functional group case do not ensure sufficient load transfer to the functional groups before the disentanglement of the free functionalized polymer chain. Although

there is no large improvement of the peak force in the 1 functional group case comparing with the non-functionalzied interface, a reloading near 73.6Å is observed to plateau around 10Å for a while, which is believed to be attributed to the functional group getting engaged in taking load. However, as the free functionalized polymer chain easily slip off of the rest of the polymer chains, the peak force of the reloading is low compared to the 5 and 10 functional groups cases. But the reloading of the 1 functional group case does lead to an increase in separation energy relative to the non-functionalized interface and therefore a interface with improved strength. For the 5 and 10 functional groups cases, there is no discernable region 2 observed in the force-separation responses as there is no decrease or plateau in the force following the initial loading segment. Instead, the force immediately continues to significantly increase indicating the engagement of functional groups in the load transfer. Such enhancement of the load transfer efficiency is believed to reflect the larger degree of entanglement and therefore load transfer to the functional group. For the 10 functional groups case, it is noted that the peak force and subsequent dropping labeled in the saw-toothed third region correspond to the bond breaking in one constrained non-functionalized polymer chain locked with one of the functionalized polymer chains as shown in the inset (A) and (B) in Figure 4.12, which demonstrates that strong entanglements such as knots in the polymer matrix can lead to sufficient load transfer to the functional groups. For both 5 and 10 functional groups cases, a significant long plateau region is observed before the complete failure of the interface indicated by the force dropping to zero, which demonstrates the moderate load transfer to the functional groups through the random network of disentangling entanglements prior to

the complete disentanglement of functionalized polymer chains from the constrained polymer chains. As shown in Table 4.2 and 4.1, 10c300c cases demonstrate comparable overall peak force and larger separation energy compared with the corresponding 10c80c cases with same number of functional groups. The increasing in separation energy derives from the longer polymer chains in 10c300c cases which introduce much stronger entanglements in the polymer matrix and lead to much longer separation distance. Recognizing that 300 repeat units in a polymer chain, which is computational large, is till very short compared with realistic polymer chain lengths, it is anticipated that the realistic entanglements are much stronger in the polymer matrix of the nanocomposites, which can improve the load transfer of the functionalized interface.

4.4.3 Sliding Mode Separation

In addition to the normal mode separation, the sliding mode separation is simulated to characterize the load transfer at the functionalized interface in the sliding direction. The sliding mode separation simulations are performed using modified CVFF or AIREBO potentials for the functionalized graphene-PE interface with 5 functional groups. As with the normal mode separation, a region of polymer at the top of the representative interface element is frozen to simulate a grip while the graphene sheet is displaced at constant velocity until full separation occurs, only here this velocity is in the y-direction as opposed to the z. In order to simulate sliding, periodic boundary conditions are retained in the x-direction while non-periodic boundary conditions are applied in the y-and z-directions as shown in Figure

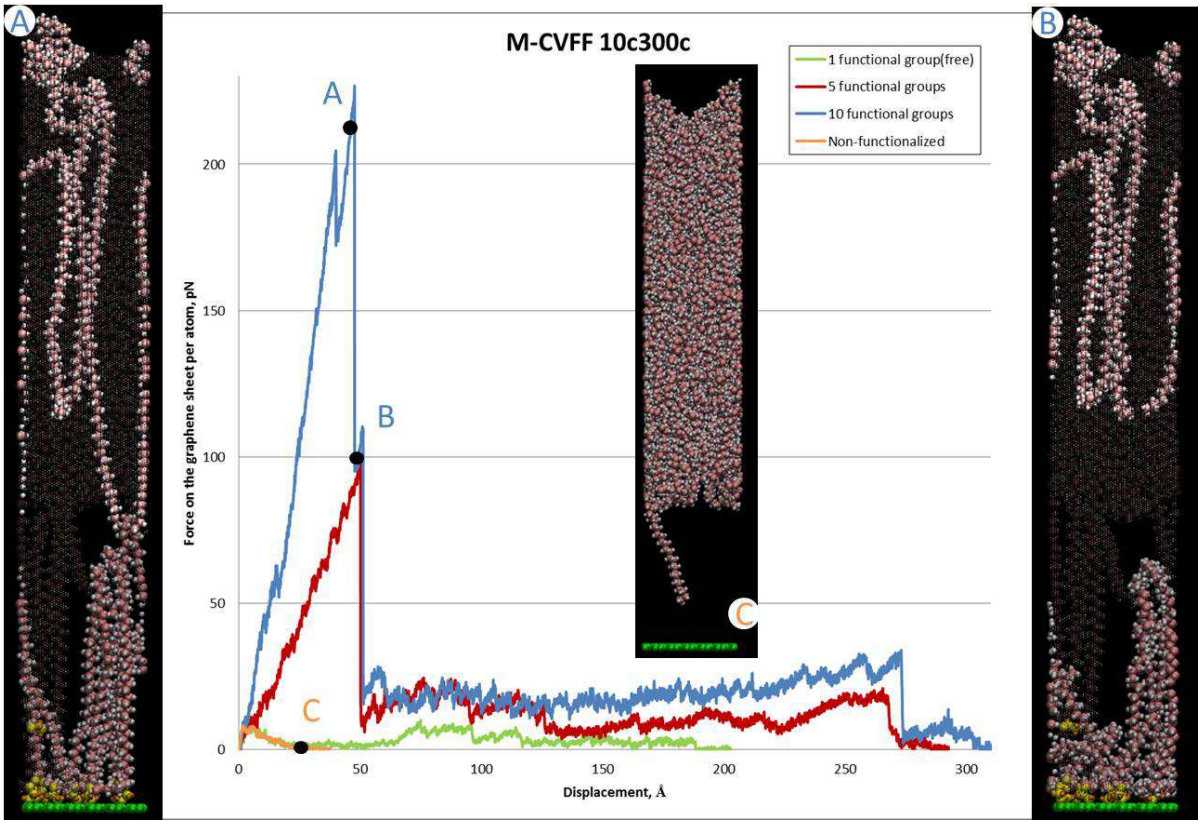

Figure 4.12: The force-separation responses for the functionalized 10c300c interfacial representative elements with 1, 5 and 10 functional groups along with three snapshots corresponding to points labeled in the force-separation responses. Insets (A) and (B) highlight the lock between the unconstrained non-functionalized polymer chain and the free functionalized polymer chain. Inset (C) gives the final configuration in the normal mode separation of the non-functionalized interface.

4.13(a) and 4.13(b). During the separation process, the averaged force on graphene sheet has been monitored in y direction.

The typical sliding mode force-separation responses are provided in Figure 4.14(a), along with three snapshots highlighting functionalized polymer chain response in the Figure 4.14 corresponding to the points labeled A)(the starting configuration), B)(a loading segment) and C)(an unloading segment) in the force-separation response for the modified CVFF case. It is noted that similar profiles as the normal mode force-separation responses are observed, i.e. there are discernible regions 1,2 and 3 as well as an observable saw-toothed pattern in region 3 associated with functionalized polymer chains loading and then breaking resulting in load redistribution. The initial increasing of the force in region 1 corresponds to the disentanglements of the polymer chains surrounding the graphene sheet. Then as the functionalized polymer chains begin to participate in the load transfer, the force greatly increases in a linear way for the modified CVFF case and in a more exponential manner for the AIREBO case. This response is believed to be mostly associated with the stretching of the covalent bonds in the functionalized polymer chains as shown in the snapshot in Figure 4.14(b). The peak force and the separation energy are approximately 88.8 pN and 8,250 mJ/m^2 (increased of 43 and 99.6 times relative to the non-functionalized interface) for the modified CVFF case and approximately 40.0 pN and 1,040 mJ/m^2 (increases of 4.87 and 10.4 times relative to the non-functionalized interface) for the AIREBO case. In fact, the functionalized interface models have the peak force and separation energy in the sliding mode separation comparable with those of normal separations, thus leading to a nearly equal load carrying capability

in both normal and sliding modes that was not present in the non-functionalized interface which was largely governed by the normal mode response [76]. This implies a significant improvement of the overall load transfer ability of the interface through functionalization as much of the load expected to be experienced by the CNT will be associated with shear load transfer and therefore the sliding mode.

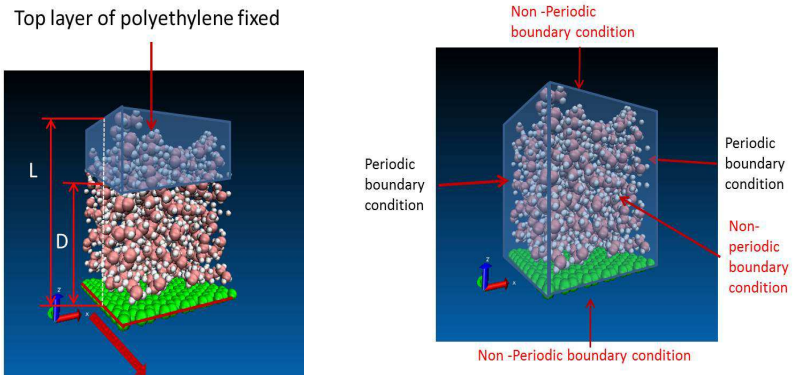

Figure 4.13: Constraints with the arrow indicating the direction of the velocity on graphene sheet(a) and boundary conditions(b) for representative interface element(10c80c case) in sliding mode separation. r in parametric study is defined in (a) as $r = \frac{D}{L}$.

4.5 Macroscale effective elastic properties of CNT-Epoxy nanocomposites with molecular representative interface element derived cohesive zone models

The cohesive zone traction-displacement laws in both normal and sliding directions having multiple peaks are developed to keep the multiple peak traction and the displacements at

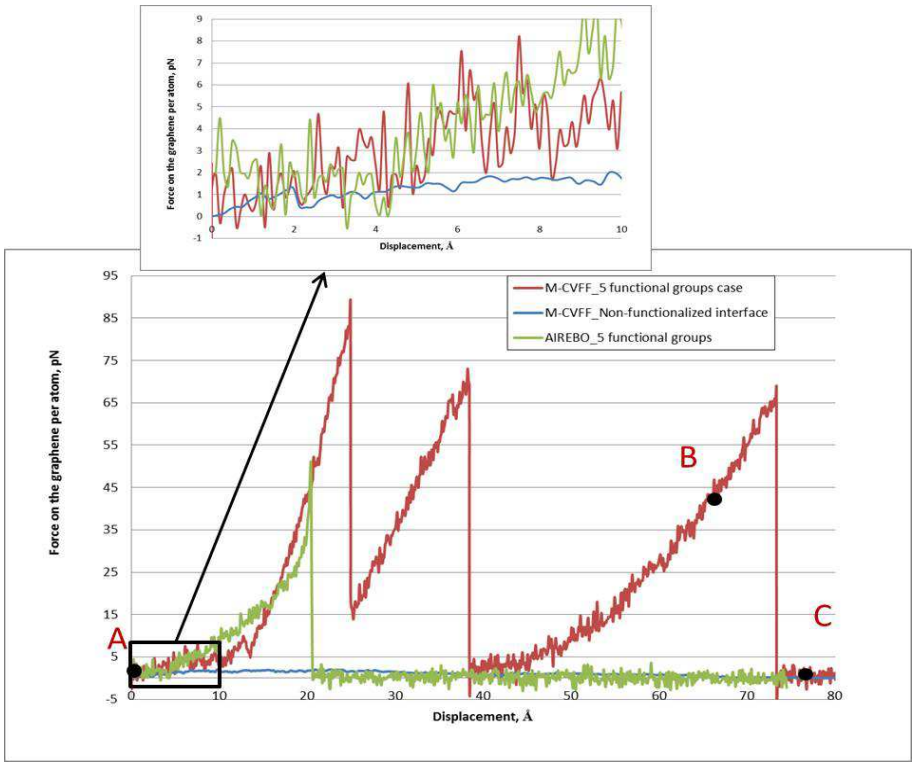

(a)

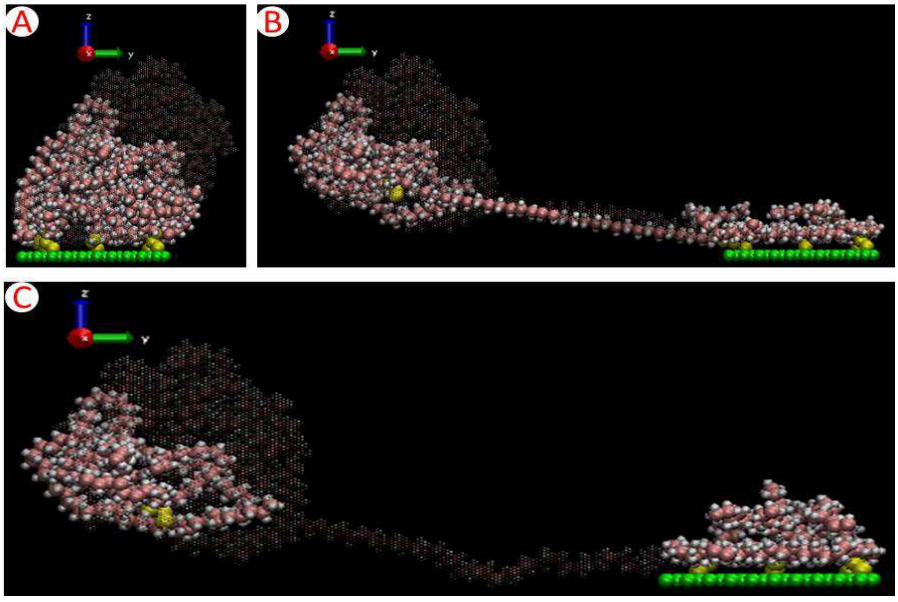

(b)

Figure 4.14: Comparison of force-separation responses in the sliding mode separation simulated using the modified CVFF or the AIREBO potentials for functionalized graphene-PE interface models and simulated using the modified CVFF potential for the non-functionalized interface. b) gives three snapshots presenting the configurations of the functionalized graphene-PE interface models in the sliding mode separation.

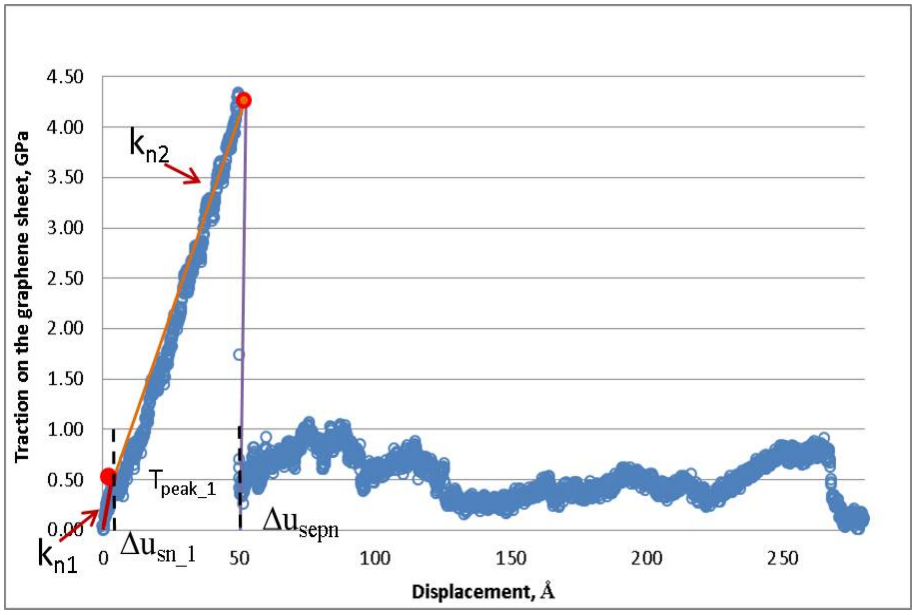

(a)

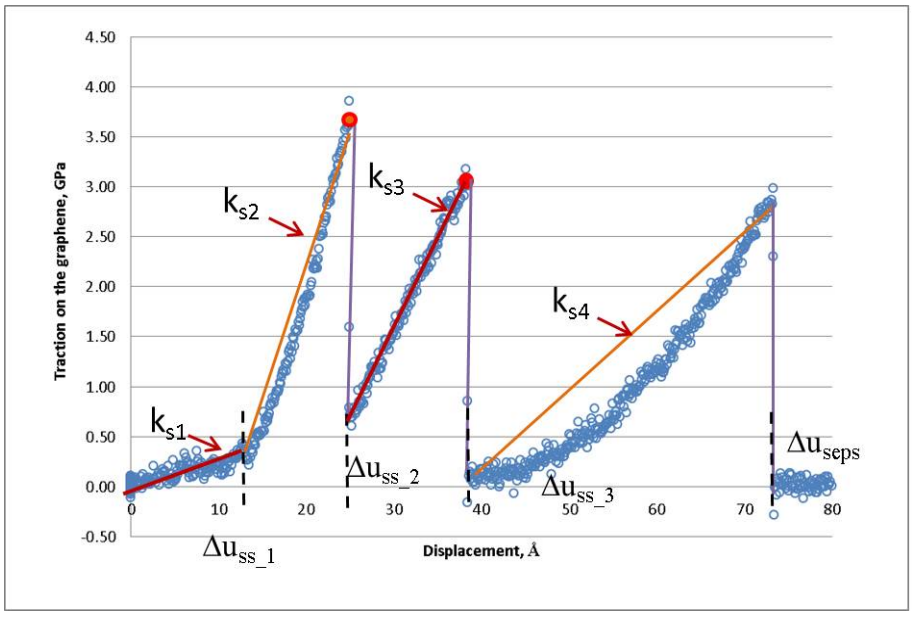

(b)

Figure 4.15: Cohesive zone laws in normal ((a)) and sliding (b) directions developed based on the force-separation response of the functionalized graphene-PE interface in MD simulations.

the peak traction observed in the MD simulations as shown in Figure 4.15. The cohesive zone laws are simply fitted to the traction-separation relations and have linear forms in the loading regions. It is also noted that for the simplification reasons the separation distance for the normal mode indicated by the cohesive zone laws is not the relative normal displacement where the interface reaches the total failure.

The form of cohesive zone laws in the normal mode for the functionalized graphene-PE interface is provided in the Equations 4.6 , 4.7 , 4.8.

$$t_{n1} = k_{n1}\Delta u_n + bn_1 \qquad if\ \Delta u_n < \Delta u_{sn_1} \tag{4.6}$$

$$t_{n2} = k_{n2}\Delta u_n + bn_2 \qquad if\ \Delta u_{sn_1} < \Delta u_n < \Delta u_{sepn} \tag{4.7}$$

$$t_{n3} = 0 \qquad if\ \Delta u > \Delta u_{sepn} \tag{4.8}$$

where t_{n1}, t_{n2} and t_{n3} are the traction, k_{n1} and k_{n2} are the stiffness for the loading portions, Δu_n is the relative normal displacement of the interface, Δu_{sn_1} is the relative normal displacement of the interface at which the first local peak traction is reached. Δu_{sepn} is considered as the relative normal displacement of the interface at which the complete separation of the interface is reached.

Cohesive zone laws in the sliding mode has the similar form as that in the normal mode as shown in Equations 4.9 , 4.10 , 4.11 , 4.12 and 4.13.

$$t_{s1} = k_{s1}\Delta u_s + bs_1 \qquad if\ \Delta u_s < \Delta u_{ss_1} \tag{4.9}$$

$$t_{s2} = k_{s2}\Delta u_s + bs_2 \qquad if\ \Delta u_{ss_1} < \Delta u_s < \Delta u_{ss_2} \tag{4.10}$$

$$t_{s3} = k_{s3}\Delta u_s + bs_2 \qquad if\ \Delta u_{ss_2} < \Delta u_s < \Delta u_{ss_3} \tag{4.11}$$

$$t_{s4} = k_{s4}\Delta u_s + bs_2 \qquad if\ \Delta u_{ss_3} < \Delta u_s < \Delta u_{sep} \tag{4.12}$$

$$t_{s5} = 0 \qquad if\ \Delta u > \Delta u_{sep} \tag{4.13}$$

where t_{s1}, t_{s2}, t_{s3} , t_{s4} and t_{s5} are the traction, k_{s1}, k_{s2} , k_{s3} and k_{s4} are the stiffness for the loading portions, Δu_s is the relative sliding displacement of the interface, Δu_{ss_1} , Δu_{ss_2} and Δu_{ss_3} is the relative normal displacement of the interface at which the local peak traction is reached. Δu_{seps} is considered as the relative normal displacement of the interface at which the complete separation of the interface is reached.

A 2-D RVE consisting of a regular hexagonal array of aligned CNTs with cohesive zone elements corresponding to both normal and sliding modes placed at the CNT-PE interface is used to obtain in-plane property, the stiffness component C_{22}, of the transversely isotropic effective nanocomposite based on the volume averaged stresses and strains.

An RVE at a CNT vf of 0.1 is shown in Figure 4.16 in the deformed configurations corresponding to the boundary conditions associated with determining C_{22}. The boundary conditions to determine effective C_{22} are such that the bottom of the RVE was fixed in both

the x- and y-directions and the left and right boundary of the RVE fixed in the x-direction, while the top boundary of the RVE was displaced in y-direction by $u_y = \varepsilon_0 L_0$ where L_0 is the undeformed length of the RVE in the y-direction.

The stress contour and deformed configuration of the nanocomposites at a CNT vf of 0.1 are shown in Figure 4.16 corresponding to the C_{22}. It is observed that the cohesive zones in the interface regions are experiencing different loading conditions, i.e some are in the initial loading region with the stiffness K_{n1} and some are in the loading region with the stiffness K_{n2}. Effective C_{22} at 100K is provided in Figure 4.17 with applied strain for CNT-epoxy nanocomposites with a CNT vf of 0.1. It is observed C_{22} at 100K is enhanced by 2%-12% for the CNT-PE nanocomposites through functionalized in the strain range of 0-0.8. For the perfect bonding case, C_{22} calculated for a small strain range of 0-0.1 are constant without the temperature and applied load dependency. For cohesive zone models, C_{22} of the CNT-PE nanocomposites with the functionalized interface decreases slightly with the increasing applied load and does not exhibit the transition as observed for those of the nanocomposites with the non-functionalized interface which has a constant value in a small strain range of 0-0.15 and then decrease nonlinearly with the further increasing of the applied load. It is believed that this is due to two reasons. First, the functionalized interface has almost equal load transfer ability in the normal and sliding separation mode which is remarkable different from the behavior of the non-functionalized interface being much weaker in the sliding mode than in the normal mode. Therefore no dominating mode is observed for the behavior of C_{22} of nanocomposites with the functionalized interface. Second, the separation distances in

both normal and sliding mode have been significantly improved for the interface through the functionalization. Therefore in the strain range of 0-0.8 all of the cohesive zone elements are still in the loading regions but having varying stiffness which is decreasing with the increasing of the applied load, i.e. very few of the cohesive zone elements achieved complete failure.

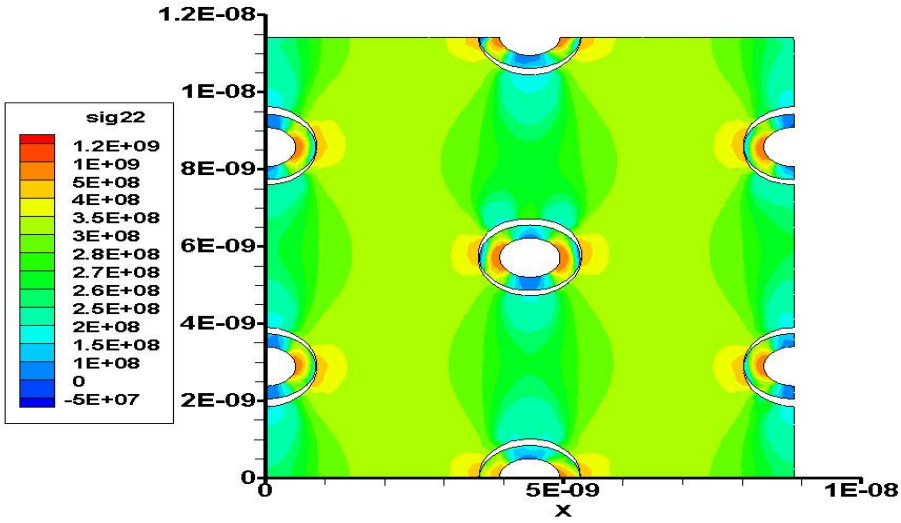

Figure 4.16: The deformation of computational RVE with the stress contour σ_{yy}(Pa) for Vf 0.1 CNT-PE nanocomposites under strain loading and.

4.6 Conclusions

In the present work, atomistic functionalized graphene-PE interface models have been constructed to characterize the ability of transferring load at the interface between CNTs and a PE matrix in functionalized CNT-PE nanocomposite in terms of the force-separation response with respect to both normal using MD simulations. Two potentials, a modified CVFF

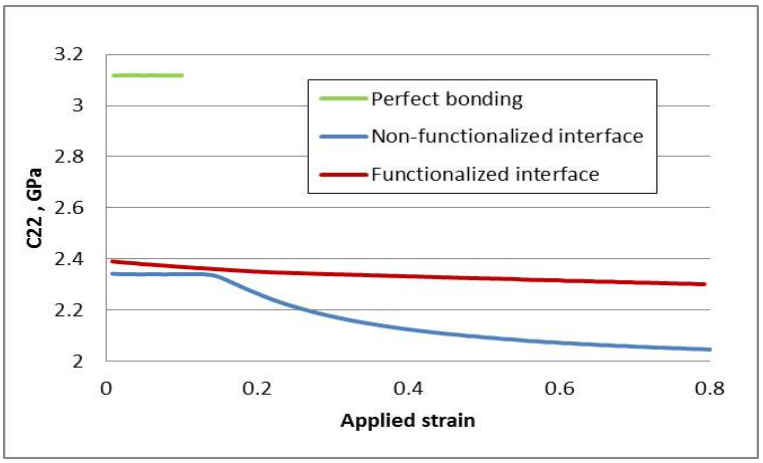

Figure 4.17: Macroscale effective C_{22} stiffness component at 100K for 0.1 vf CNT-PE nanocomposites for perfect bonding and cohesive zone cases with non-functionalized or functionalized interface obtained from FEA-based computational micromechanics approach

and AIREBO, have been used to simulate the interactions between atoms in the simulation system in order to compare the two commonly used potentials in polymer based nanocomposites research. The influence of the functionalization density on the load transfer ability is investigated by conducting normal mode separation simulations of functionalized representative interface elements with variable number of functional groups between the polymer chains in the matrix and the graphene sheet that represents CNTs surface.

Gripping conditions in which the functional groups are grafted to free polymer chains versus when they are grafted to constrained polymer chains demonstrate the importance of having long range entanglements of polymer chains in order to have good load transfer through the functional group to the graphene sheet. For normal opening mode separations using modified CVFF and AIREBO potentials, the force-separation responses are observed to exhibit similar trends generally denoted by three regions. For most of the cases, the first

regions are associated with initial disentanglement of the amorphous PE chains as observed in the normal opening force-separation responses for the non-functionalized graphene-PE interface models. In the third regions saw-toothed patterns are observed and it is noted that the peak force is increased by 15.3-21.6 times for the CVFF cases and 9.06-25.7 times for the AIREBO cases as compared to the non-functionalized graphene-PE interface model, both of which indicate an large improvements in the load transfer ability of the funcitonalized interface. Larger separation energy has also been observed for the interface with more functional groups in the normal mode separation which demonstrates higher functionlaization density can lead to the better load transfer ability of the functionalized interface. For the sliding mode separations, 5 functional groups cases demonstrates increased overall peak force and separation energy (43 and 99.6 times for the modified CVFF case and 4.87 and 10.4 times for the AIREBO case). It shows that the functionalized interface model has a nearly equal load carrying capability in both normal and sliding modes, which indicates the significant improved overall load transfer ability of the interface through the functionalization. For the functionalized interface in the 10c300c cases, the strong entanglements resulting from the long polymer chains in the matrix is observed to have significant contribution on the enhanced strength of the functionalized interface, which indicates the functionalization is able to significantly improve the load transfer of the interface in the nanocomposites.

While the enhancement of the load transfer has been observed for the functionalized interface simulated using both the modified CVFF and the AIREBO potentials, it is noted that due to differences in the formulation of the potentials as well as the resulting amorphous structure

derived from it, the modified CVFF cases obtained higher peak force, longer separation distance and therefore larger separation energy in the normal opening and sliding mode separation relative to the AIREBO cases. For the normal mode separation using the modified CVFF cases, in the third region, it is noted that the slope of first loading segment varies with the number of broken bonds in the separation, which is less observable for the AIREBO cases. As another parameter describing the properties of the interface, a sharper slope of the loading region should correspond to a stiffer interface, which is consistent to the observation for the modified CVFF cases with multiple functional groups. Therefore for the modified CVFF cases, the interface is stronger while a sharper slope and a larger separation energy are observed in the force-separation responses. The modified CVFF demonstrates that the load transfer ability of the functionalized interface is sensitive to the number of the functional groups. Therefore it is more meaningful to characterize the load transfer capability of the functionalized interface using the modified CVFF. Considering the expensive computational cost of the AIREBO potential as it is sensitive to the size of time step, it is also more efficient to use the modified CVFF potential.

It has been shown ([76]) that due to the present of a weak non-functionalized interface between CNTs and the polymer matrix, the macroscale effective properties of the CNT-PE nanocomposites experienced significant depreciation compared to the micromechanics predictions with perfect bonding assumptions. As observed for CNT pull-out in the work of [54], this study shows that functionalization can greatly enhance the load transfer at the CNT-polymer interface. Observing herein that the normal and sliding modes both

yield significantly improved interfacial load transfer, the latter more so relative to its non-functionalized counterpart, it is expected that all effective elastic properties, especially those relying on shear load transfer, will be enhanced along with their durability under load. The finite element implementation of cohesive zone model is applied to calculate macroscale effective mechanical property of the CNT-PE nanocomposites with the functionalized interface, which demonstrates improved $C_(22)$ relative to the CNT-PE nanocomposites with the non-functionalized interface. It indicates that the functionalization of the interface helps to improve the effective mechanical properties of the CNT-reinforced polymer nanocomposites.

Chapter 5

Characterization of nanoscale load transfer at the CNT-epoxy interface using molecular dynamic simulation

5.1 Introduction

Epoxy is an important engineering resin as it is easy to process and has excellent mechanical properties. Epoxy is widely used as the matrix material in the fabrication of carbon and glass fiber composites for the aerospace industry. As such, CNT reinforced epoxy polymer composites have attracted great interest for supplementing the existing matrix material for increased stiffness with minimal if any weight penalty and the potential for multi-functionalization.

Many attempts have been made to develop surface treatments techniques to enhance the adhesion between CNTs and the polymer matrix through improved dispersion of the CNTs in the polymer matrix and/or through bonding of the CNT-polymer interface. For example, in [30] authors applied amino-functionalization to CNTs and observed a better dispersion and integration of CNTs in the polymer matrix and the resulting remarkable improvement in mechanical properties, 24.6% increases for the elastic modulus with only 0.5 wt% addition of functionalized CNTs in contrast to only 3.2% increases of non-functionalized CNT reinforced nanocomposites. In [35] authors fabricated epoxy-based nanocomposites reinforced by CNTs with covalently attached amino groups which can react with the resin monomers in the matrix and lead to a fully integrated nanocomposites structure. They reported 30-70% increase in ultimate strength and modulus of the nanocomposites with 1-4 wt% functionalized SWNTs and an increased strain to failure. Although the experimental results provide strong evidence that the reinforcement efficiency of CNTs in the epoxy polymer nanocomposites is affected by the interfacial interactions and can be largely enhanced by the application of the functionalization, the interfacial mechanism behind these is still not fully understood. The improved fabrication of CNT-reinforced epoxy polymer nanocomposites possessing enhanced mechanical performance can benefit from better understanding of the interface properties and their effects on the macroscale effective material properties.

In the present work, a graphene-epoxy interface model is adopted to investigate the load transfer properties of the non-functionalized and functionalized interface in the CNT-epoxy nanocomposites by conducting the atomistic MD simulations. A dynamic crosslinking al-

gorithm is developed to construct the atomistic structure of croslinked epoxy matrices with various crosslink densities. The functionalized graphene-epoxy interface is modeled by grafting functional groups to the graphene sheet, which enable the direct covalent interaction of the graphene sheet with the crosslinked network of the epoxy polymer matrix by crosslinking with the Epon resin. Separations in normal and sliding directions are simulated to assess the interfacial load transfer characteristics for the non-functionalized and functionalized interface models at specified temperatures. Parametric study is applied towards investigating the influence of the temperature and the crosslinking density on the load transfer ability of the interface. The effective material properties of CNT-epoxy nanocomposites were calculated using finite element analysis embedded with cohesive zone models, which behaviors following cohesive zone laws developed based on traction-separation responses from MD simulations. It is anticipated that the results of the parametric study can provide possible reasons behind the low experimental values of effective material properties of the CNT-reinforced polymer nanocomposites and the improvement in mechanical properties obtained through functionalization. This in turn may offer insights has to how to improve the design of nanocomposites.

5.2 Description of Potential Energy

The OPLS All-Atom(AA) force field, which was developed by Jorgensen and coworkers [64] based on the Assisted Model Building and Energy Refinement(AMBER) potential for organic molecules, was used to simulate the intra and intermolecular forces in the epoxy matrix of

interfacial system. The OPLS AA potential consists of four energy parts which include bond stretching, angle bending, torsion and non-bonded interactions.

The bond stretching potential is a two body potential which models the change of the distance between two covalently bonded atoms and is given by:

$$E_b = \sum_{i=1}^{nb} K_b^i (r^i - r_0^i)^2 \tag{5.1}$$

where r^i represents the distance between two atoms in the i^{th} covalent bond, r_0^i represents the equilibrium distance between two atoms in the i^{th} covalent bond, K_b^i is the stiffness of the i^{th} covalent bond, nb is the number of the bonds in the system.

The angle bending potential is a three body potential which captures the change of the energy with the change of the angle between two covalent bonds and is given by:

$$E_a = \sum_{i=1}^{na} K_\theta^i (\theta^i - \theta_0^i)^2 \tag{5.2}$$

where θ^i represents the angle formed between the i^{th} pair of adjacent covalent bonds, θ_0^i represents the equilibrium angle for the i^{th} pair of adjacent covalent bonds, K_θ^i is the angle stiffness of the angle for the i^{th} pair of the adjacent covalent bond, and na is the number of the angles in the system.

Torsion potential is a four body potential which captures the energy of the angle formed by

four atoms covalently bonded and is given by:

$$E_t = \sum_{i=1}^{nd} \frac{1}{2}V_1^i[1+\cos(\phi^i)] + \frac{1}{2}V_2^i[1-\cos(\phi^i)] + \frac{1}{2}V_3^i[1+\cos(\phi^i)] + \frac{1}{2}V_4^i[1-\cos(\phi^i)] \quad (5.3)$$

where V_1^i, V_2^i, V_3^i and V_4^i are coefficients for the i^{th} dihedral angle in the Fourier series, and ϕ is the i^{th} dihedral angle.

Finally, the non-bonded pair potential considers the energy between non-covalently-bonded atoms which is typically recognized as the van der Waals interaction, and is given by:

$$E_p = 4\sum_{i=1,j\neq i}^{n} \varepsilon_{ij}[(\frac{\sigma_{ij}}{r_{ij}})^{12} - (\frac{\sigma_{ij}}{r_{ij}})^{6}] \qquad r < r_c \quad (5.4)$$

where ε_{ij} is the energy well depth for the interaction between i^{th} and j^{th} atoms, r_{ij} is the distance between the i^{th} and j^{th} atoms, σ_{ij} is the equilibrium distance between the i^{th} and j^{th} atoms, n is the total number of atoms in the system and r_c is the cutoff distance beyond which the force between the i^{th} and j^{th} atoms is ignored.

The complete potential is represented by summing the four components together:

$$E_{total} = E_b + E_a + E_t + E_p \quad (5.5)$$

The forces acting on each atom in the system are obtained by taking the negative of the gradient of the potential energy, and are subsequently applied in Newton's second law to

Table 5.1: Atom types in EPON 862 and DETDA.

Type ID	Atom types	Color code in pictures
1	carbonyl sp^2 carbon	Pink
2	aromatic sp^2 carbon	Mauve
3	sp^3 carbon	Purple
4	sp^3 oxygen in ethers	Cyan
5	sp^3 oxygen in alcohols	Lime
6	hydrogen in $-NH_2$	Ochre
7	Nitrogen	Iceblue
8	Hydrogen in $-OH$	Black

obtain the net acceleration of the atom at a given time step. For each time step, the position and velocity of each atom is obtained by integrating the acceleration using Verlet algorithm. Given the initial positions and velocities, the future positions and velocities of all atoms can be obtained. All parameters for the potential components identified above are draw from [64].

5.3 Molecular model

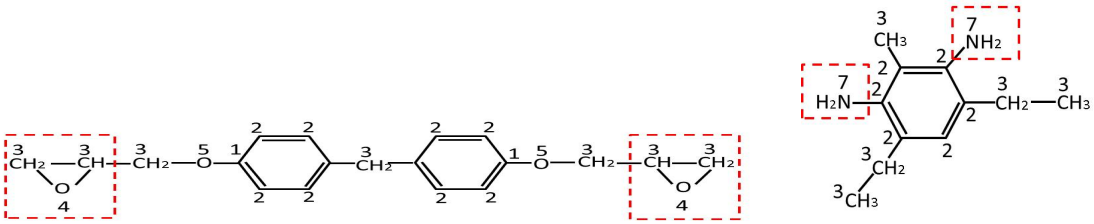

(a) (b)

Figure 5.1: The atomistic structures of (a)Epon 862 monomers and (b)DETDA hardener with the labels of atomic types as described in Table 5.1 and reactive pairs.

The epoxy material considered here consists of EPON 862 monomers and DETDA hardeners,

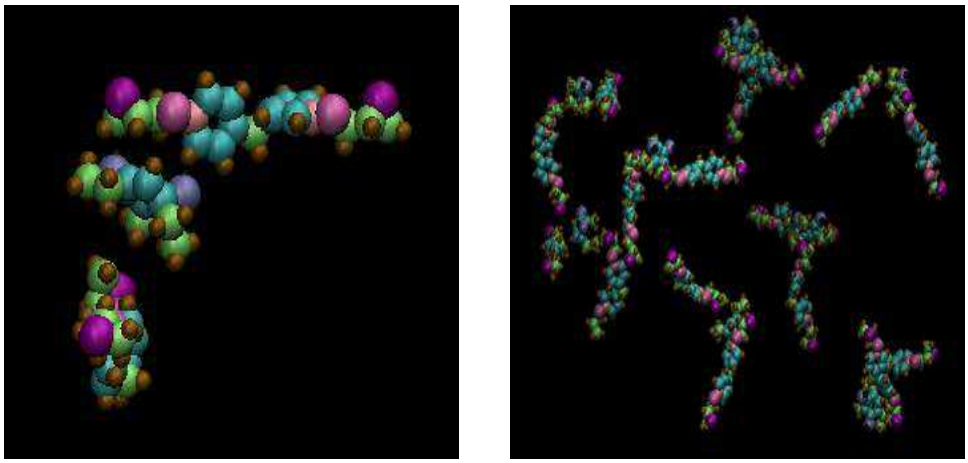

(a) (b)

Figure 5.2: (a) shows the initial configuration of the 3 segments system modeled. (b) shows the initial state of 12/6 system obtained by combining the 3 chains systems with different translations and rotations.

represented in the interface model with the full explicit atomistic details of all molecules in order to capture direct local interactions between the epoxy and graphene atoms at the interface, i.e. no coarse grains is used. An initial configuration of the uncrosslinked epoxy with two EPON 862 monomers and one DETDA hardener were constructed so as to have the three polymer chains positioned as shown in Figure 5.1(a), wherein the relative positions of all atoms within each molecule segment are close to the equilibrium bond distance. Relaxation of the initial configuration has been performed using MD simulations under the NVT ensemble with periodic boundary conditions in all directions in order to achieve a dynamic equilibrium state. Subsequently, a larger system with 12 EPON 862 monomers and 6 DETDA hardeners was formed by repeating the 3 molecule segment system 6 times placed randomly at random orientations in Figure 5.1(b). Pre-crosslinking was done for the 12/6 system to achieve a crosslink density of 53%[1] using the dynamic crosslinking process discussed below. The size

[1]The crosslink density equals the ratio of the number of actual crosslinks formed to the number of possible

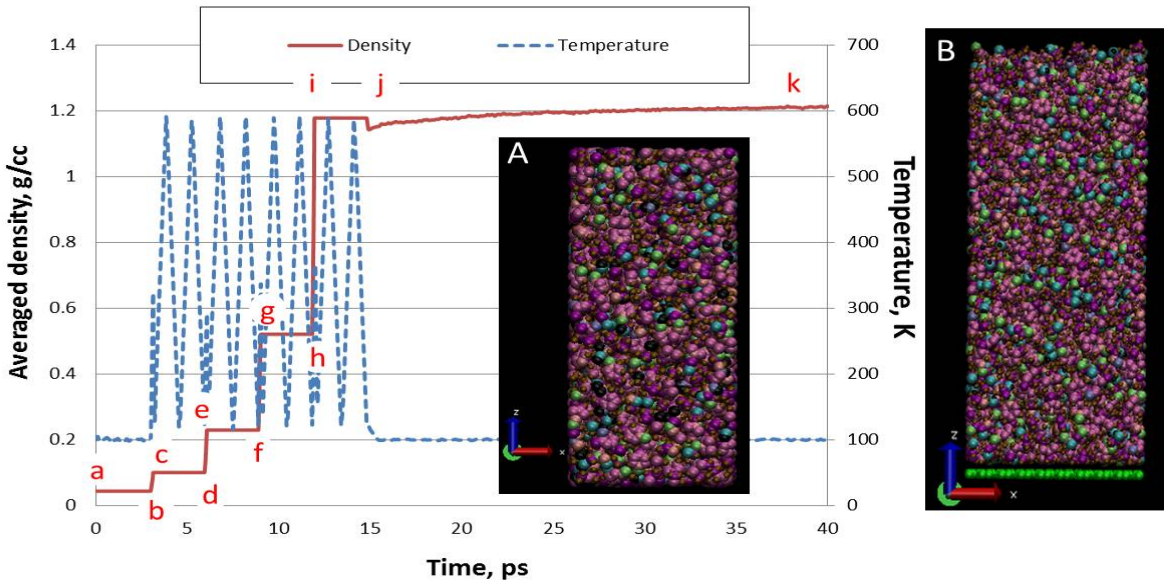

Figure 5.3: The change of the density of the mixed Epon monomers and the hardeners and the temperature of the simulation system with respect to time during the preparing process at 100K. a through k denote key steps in the procedure. (A) gives the amorphous polymer structure and (B) gives the prepared equilibrium interface model

of the system was once again increased to a 240/120 epoxy system which was constructed by combining twenty 12/6 systems with different translations and rotations in a large simulation box with a very low density of around 0.044 g/cm^3 and same crosslinking density of around 53%. A MD simulation using NVT ensemble with two temperature annealing cycles with temperatures ranging between 100K and 600K and five steps of volume shrinkage was applied (Figure 5.3) in order to obtain a 240/120 system possessing a more realistic density of 1.2 g/cm^3. The volume shrinkage steps were applied by reducing the volume of the simulation box in all directions at the same rate under NVT ensemble conditions corresponding to the region labeled from a through j in Figure 5.3. The temperature annealing cycles were

crosslinks that could be formed.

conducted between two volume shrinkage steps to relax the stresses in the polymer system resulting from the volume shrinkage by fixing the volume of the simulation box and using a Nose-Hoover thermostat to control and change the temperature in the simulation system. Subsequent to point j, the simulation box was switched from the NVT ensemble conditions to NPT at 1 atm of pressure at the desired temperature allowing the relaxation of the simulation system in approaching a steady state density at point k. During the whole process, periodic boundary conditions are applied in all directions of the simulation box.The interactions between atoms inside the simulation system are simulated by using unmodified OPLS potential, i.e. without bond breaking. All MD simulations were performed using LAMMPS.

In the present work, a flat graphene sheet is used to study the interfacial load transfer as it has been observed to have similar local morphology as CNTs and to yield comparatively similar force-separation response as CNTs with reasonably large radii [76, 47]. Such a representation has advantages in computation efficiency than the more straight-forward models including individual CNTs or a subset of the bundle along with the locally enveloping polymer applied in other references (see for example [50]) in that characteristic normal and sliding separation modes associated with the local interface can be simulated with fewer atoms.

An interface model for the CNT-Epoxy nanocomposite was constructed by introducing the flat graphene sheet to the Epoxy polymer structure oriented in x-y plane at z=0 with some prescribed distance prior to minimization. With periodic boundary conditions in the x- and y-directions and non-periodic conditions in the z-directions, energy minimization at 0K

and following dynamic equilibration with the NVT ensemble at the required temperature was accomplished to allow for the perfect wetting of the polymer to the graphene sheet and thereby establish the equilibrium distance between the graphene and the epoxy in the graphene-epoxy interface model. By performing the dynamic equilibration for a sufficient amount of time, an equilibrium graphene-epoxy representative interface element was obtained as shown in Figure 5.3(B). The representative interface elements with the epoxy polymer crosslinked at different levels are prepared to conduct normal opening mode and sliding mode separation simulations using the dynamic crosslinking algorithm described below.

5.4 Dynamic Crosslinking Process

In order to capture the complex interactions within the epoxy network and to study the influence of crosslink density on the interfacial load transfer, a dynamic crosslinking procedure was developed which allowed for the degree of crosslinking to be specified.

The reactive pairs in EPON 862 monomers and DETDA hardeners, i.e. the epoxide ends and amines, are highlighted in Figure 5.4. Crosslinks were formed statically based on the distance between the C atoms in epoxide ends of the EPON 862 molecules and N atoms in the amines of the DETDA hardeners either in the 12/6 systems having mixed EPON monomers and DETDA hardeners (establishing the baseline of 53% crosslinked) or in the equilibrated structure of the representative interface element (allowing for crosslinking densities greater than 53%). An active N atom in the amine could form a crosslink with the active C in

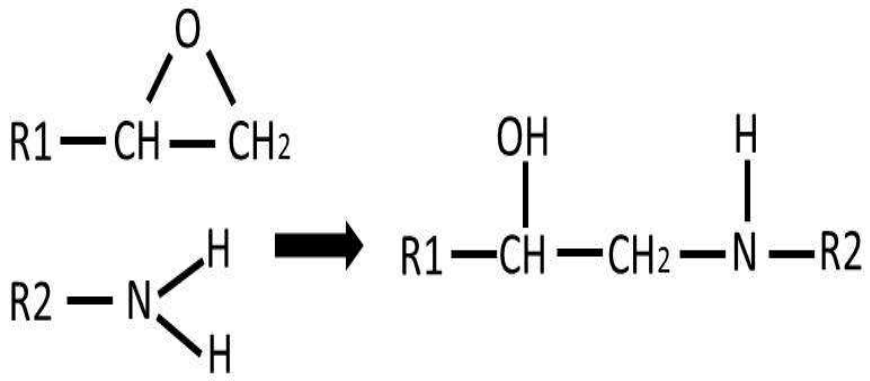

Figure 5.4: The crosslinking reaction for the reactive pairs in the EPON 862 monomers and DETDA hardener, the epoxide ends and amines in the left. The C-O and N-H bonds are debonded during the crosslinking process. The new C-N and O-H bonds are formed to create an epoxy network. One type of R1 and R2 can be the parts of EPON 862 monomer and DETDA hardener inside the red boxes as shown in Figure 5.2.

the epoxide end when the N atom and the C atom are within a specified cutoff distance. Several assumptions were made for the dynamic crosslinking process. First, all the potential reactive sites were activated in both the epoxy resin and the curing agent. Second, the two amine groups in the DETDA hardener were assumed to be equally reactive. Third, during the crosslinking process, the $CH_2 - O$ bonds and $N - H$ bonds were broken simultaneously and subsequently simultaneously reacted. A flowchart describing the crosslinking process is provided in Figure 5.5.

A cutoff distance with an upper bound of 6Å were defined in order to achieve the desired level of crosslink denisty. The distances were computed between N atoms and C atoms in the active reactive pairs within the cutoff distance. Crosslinks were formed between the N atoms and the C atoms which have the minimum distance. Simultaneous bond breaking

Table 5.2: The stiffness and the equilibrium bond lengthes of the newly formed C-N bonds and O-H bonds in each step of the multiple-step relaxation.

Step	Stiffness of the bonds		Equilibrium bond length	
	C-N bond	O-H bond	C-N bond	O-H bond
step 1	169	276	4	4
step 2	260	400	3	3
step 3	303	500	2	2
step 4	337	553	1.34	0.96

in the corresponding $N-H$ bonds and CH_2-O bonds were enacted which would result in the H^+ ions and O^- atoms. Then the H^+ ions are reacted with the O^- atoms [2] in the broken epoxide ends restoring the neutrality of the EPON 862-DETDA system. At the moment while breaking and forming bonds, all of the atoms in the simulation system were held stationary before the being re-equilibrated with the new crosslinked topology. It is noted that in forming the crosslinked covalent bonds, that the associated angle and dihedral multi-atom interactions were also deleted.

If there were crosslinks formed, multiple relaxation steps were applied in order to prevent instability of the system with the new topology as the new bonds may be formed at distances much greater than that of equilibrium [81]. The multiple relaxation steps were used in order to prevent suddenly spatial changes in the vicinity near the newly formed bonds in the new topology by gradually increasing the stiffness of the new bonds and gradually decreasing the bond length of the new bonds to their actual values in a series of steps as indicated in Table 5.2. After the interface system with the new topology achieved equilibrium, the associated

[2]The ions are not actually simulated here as no electrostatic potential is included to account for the Coulombic interactions between charged atoms.

new angles and dihedrals were created for the newly formed bonds.

Whether or not new crosslinks are formed, a MD simulation under the NVT ensemble at the specified temperature was conducted to further relax the system as well as to dissipate the unreacted reactive species, thereby preparing the system for the next crosslinking step. Temperature annealing cycles were applied in order to put energy into the simulation system by raising the temperature well above the transition temperature (144°) thereby aiding in the diffusion induced dispersion of the crosslinking entities before returning the temperature back to the required temperature.

After the equilibration of the newly crosslinked system, if the required crosslinking density is reached, the algorithm is stopped and the topology information of the new structure is output; else the algorithm returns to the crosslinking step and proceeds with additional inner loops as indicated in Figure 5.5.

5.5 Functionalization

It is noted that large improvements in the load transfer ability of a functionalized CNT-polymer interface have been observed in MD studies of CNT-PE nanocomposites study [76]. However, as the amorphous thermoplastic PE did not contain crosslinks and therefore did not form a network structure, the efficiency of the functionalization depends on the entanglements of the functionalized polymer chains. Functionalized polymer chains which were sufficiently entangled with the bulk polymer would indeed provide additional load trans-

fer (interface strength and toughness) until either a bond broke or the chains disentangled. However, those functionalized polymer chains which were not sufficiently entangled simply disentangled and provided little to no improvement of the interface. In contrast, as a crosslinked thermoset polymer, epoxy forms a dense covalently bonded network structure. As such, functionalization of the CNT surface so as to covalently bond to any segment of the network structure is expected to consistently improve interfacial load transfer until loads become sufficiently large enough to break covalent bonds in the functional group or surrounding network structure.

For CNT-reinforced epoxy nanocomposites, directly grafting amino groups to the nanotube surfaces has been observed to be an efficient approach to improve the interfacial bonding of CNTs to the polymer matrix [30, 82]. By using the scheme depicted in Figure 1 in reference [82], the DETDA molecule is able to be grafted to the surface of the outer wall of CNTs thereby serving as the functional groups. Because a graphene sheet is utilized herein to represent CNTs in our representative interface element, DETDA molecules as functional groups were covalently attached to the surface of the graphene sheet by carbon-carbon bonds as shown in Figure 5.6. In the functionalized graphene sheet, there is one amine group (labeled by the boxes in Figure 5.6) left in each functional group which can participate in the crosslinking process of the EPON 862/DETDA epoxy polymer to form covalent bonds between the graphene sheet and the polymer matrix network. As the main interest here is the final configuration of the functionalized CNTs, the specific details about the process of the amino-grafting functionalization are not discussed or modeled here.

A functionalized graphene-epoxy representative interface element is constructed by introducing the functionalized graphene sheet to the 240/120 epoxy system with 53% crosslinking density. The dynamic crosslinking process described in the previous section was performed to obtain the functionalized graphene-epoxy representative interface element with higher crosslinking density, e.g. 83% crosslinked. First, only the amine ends in the functional groups and the epoxy ends in the polymer matrix were allowed to form crosslinks. Subsequently, crosslinking within the epoxy polymer matrix was performed in order to obtain different realizations of the funcitionalized graphene-epoxy representative interface element with various crosslinking densities higher than 53%.

5.6 Characterizing Load Transfer in the Nanoscale Representative Interface Element

Load transfer of both the nonfunctionalized and functionalized representative interface elements with varying crosslink densities was characterized by conducting normal opening and sliding mode separation studies at 100K and 300K using MD simulations.

5.6.1 Normal Opening Mode Separation

In order to conduct normal mode load transfer studies on the representative interface element, a region of the polymer at the top of the representative interface has been frozen, i.e. is

fully constrained to simulate a grip as shown in figure 5.7(a), while the graphene sheet was displaced in the z- direction through a uniform application of a velocity of 2.5 m/s. Periodic boundary conditions were applied in the x- and y-directions such that the interface can be effectively taken to be repeated (i.e. infinite) in the x- and y-directions as shown in figure 5.7(b). Throughout the simulation, which was continued until full separation was achieved, the temperature was fixed at the certain temperature under NVT ensemble conditions. The force on each of carbon atoms in the graphene sheet (576 carbon atoms) over 4 ps is averaged and combined with the displacement of the graphene sheet to obtain the force-separation response.

In Figure 5.8(a), typical force-separation responses are depicted for the normal mode separation of the non-functionalized interface models with crosslink densities of 53% and 86% at 100K. The normal mode force-separation responses for the functionalized interface model are discussed in the following section separately. It is observed that there are three regions in a typical normal mode force-separation response for the non-functionalized interface. The first region has a sharp initial loading corresponding to the increasing of the force in a nearly linear fashion with the separation of the graphene sheet from the gripped polymer matrix which is believed to be associated with the stretching of the epoxy polymer network. The second is an unloading region after reaching the peak force, which corresponds to a gradual decreasing of the force on the graphene sheet with further increase in displacement of the graphene sheet. The unloading region is a much slower process with respect to the loading region and is believed to correspond to failure initiating in the matrix. The third region is

identified to begin after the total separation of the graphene sheet from the epoxy polymer, which is indicated by the force either approaching zero or a relative low value depending on whether or not a portion of epoxy polymer staying with the graphene sheet after the separation.

5.6.2 Sliding Mode Separation

As with the normal mode separation, in the sliding mode separation a region of polymer at the top of the representative interface element is frozen to simulate a grip while the graphene sheet is displaced at constant velocity until full separation occurs, only here this velocity is in the y-direction as opposed to the z as shown in figure 5.9(a). In order to simulate sliding, periodic boundary conditions are retained in the x-direction while non-periodic boundary conditions are applied in the y- and z-directions as shown in figure 5.9(b). During the separation process, the averaged force on graphene sheet has been monitored in y-direction.

A typical sliding mode traction-separation response for the non-functionalized graphene-epoxy interface model is provided in figure 5.10(a) where a similar profile as the normal mode traction-separation response for the non-functionalized graphene-epoxy interface model is noted. It is observed that the traction initially increases gradually and then plateaus for a significant period before beginning to decay to zero or a stable small value depending on whether or not any polymer remains attracted to the graphene surface upon full separation. The peak traction is around 0.05 GPa which is fairly low compared with the peak traction

of normal separation. Three snapshots of sliding mode separation are shown in the Figure 5.10(b) and correspond to the points labeled a),b) and c) in the traction-separation response. The low force-separation response in sliding mode separation is critical to the overall load transfer of the interface between CNTs of high aspect ratio and the polymer matrix in a nanocomposites because much of the load expected to be experienced by the CNT will be associated with shear load transfer.

5.7 Parametric Study on the Crosslink Density

To study the influence of the crosslink density on the performance of the interface, normal mode separations were simulated for the non-functionalized epoxy-graphene representative interface elements with equilibrium non-functionalized representative interface elements having the crosslink densities of 53% and 86% prepared using the dynamic crosslinking process introduced above. To insure there are no biases resulting from the dynamic crosslinking process, the mass densities of the crosslinked epoxy polymer with various crosslink densities in the non-functionalized interface element were calculated along the z-axis. The non-functionalized representative interface elements were divided into slices of a specified thickness of approximately 0.2Å along the z-axis. The density was calculated for each slice by summing up per-atom masses and then averaged over the volume of the slice yielding the distribution of the molecules in the crosslinked epoxy away from the graphene surface oriented in the x-y plane. The traditional mass density is a parameter on the continuum level

and is considered to be nearly constant over the spatial domain of the studied volume. As we are studying the properties of atomistic models, the local density is strongly sensitive to and reflecting the spatial distribution of the molecules in the simulation system, while the overall global density (i.e. averaged over the total simulation space) remains comparable to the bulk mass density. Figure 5.11 shows the local mass density profile of the non-functionalized representative interface elements with various crosslink densities along the z direction. As the graphene sheet was oriented in the x-y plane at z=0, a peak density is found at z=0 corresponding to the presence of the graphene sheet. Then a trough with a width around 2.5-3.0 Å is observed which is believed to be associated with the equilibrium distance between the graphene sheet and the epoxy polymer as set by the vdW interactions at the given temperature and is reflective of the interface. Immediately following the trough, the local mass density of the epoxy polymer in the vicinity of the graphene sheet is different from the bulk mass density. This difference in the local polymer morphology near the graphene interface can be viewed as an interphase region, where local mechanical properties may also differ from those of the bulk. It is noted that the peak mass density of the epoxy polymer above the bulk density is followed by a trough below the bulk density before the mass density approaches the bulk density and fluctuates around it. Similar increase and decrease in local mass density before obtaining the bulk mass density was likewise observed in [50]. In the present work, the thickness over which the local polymer density differs significantly from the bulk mass density of the polymer is around 7-8 Å away from the graphene sheet before approaching the mass density in bulk, which suggests the effective surface polymer thickness

of the interphase region. It is further noted that with increasing crosslink density, there is no discernible change observed for the magnitude of the peak and the trough in the profile of the mass density of the epoxy matrix in the vicinity of the graphene sheet. This implies that the crosslink density does not have a big influence on the distribution of the epoxy polymer molecules surrounding the graphene sheet, and therefore any difference observed in load transfer as a function of crosslink density are associated with the load distribution in the extended polymer network.

In addition to looking at the local mass distribution in the representative interface, the distribution of crosslinks within the epoxy was observed. The number of $C-N$ bonds formed within 3Å thick slices in the z-direction were obtained and plotted versus the distance from the graphene sheet in Figure 5.12. It is noted that for both crosslinking densities considered here that the distribution of crosslinks appears uniform relative to the graphene sheet, indicating that the presence of the graphene sheet did not have significant influence on the long range crosslinking within the epoxy network.

Figure 5.13 gives the normal mode traction-separation responses for the nonfunctionalized graphene-PE and graphene-epoxy interface models at 100K. As the graphene sheets used in the representative interface elements have different dimensions for different material systems, the traction on the graphene sheet was calculated by averaging the force over the area of the graphene sheet for comparison purposes. For the graphene-PE interfacial system, the traction-separation responses are given for two cases with different length of polymer chains in the amorphous polymer matrix. Both of the cases have 10 polymer chains but one has 78

monomers per chain (10c80c case) and the other has 298 monomers per chains (10c300c case). In comparing the two polymer systems, it is noted that similar behavior is observed in the normal mode traction-separation responses of the graphene-PE and graphene-epoxy interface models. For example, both include an initial sharp loading region followed by a relative slow unloading region after the peak traction. However, the graphene-epoxy interface models with various crosslinking densities demonstrate only slightly higher peak traction (0.43 vs 0.3 GPa). In addition, it is observed that the displacement of the graphene sheet at the peak traction and the final separation distance for the graphene-epoxy interface model is around 4.5Å and 50Å on average, respectively, which is closer to those for the 10c300c case (4.3Å and 48Å) than those for the 10c80c case (2.4Å and 80Å). As was observed via tortuosity measurements in [76], the longer chains of the 10c300c case has a greater potential for forming strong entanglements than the 10c80c case. As the crosslinks between the Epon monomers and the hardeners are analogous (though more frequent) to the entanglements between the PE chains hindering the movements of the polymer molecules during the separation, it is believed that more entanglements, and therefore by analogy more of crosslink network, becomes engaged in transferring the load to the interface, resulting in the increase in peak force before separating from the interface in more of a block network and thereby leading to a narrow force-separation response.

The observations of the similarity between the epoxy and entangled PE extend to understanding the slight differences between the epoxies of different crosslink densities. For example, as in Figure 5.13, the peak traction in the normal mode separation is observed to be higher for

the graphene-epoxy interface models with a higher crosslink density than that with a lower crosslink densities. The crosslinks between the Epon monomers and the hardeners create a more connected network of epoxy polymer wherein the polymer molecules interact with each other by strong covalent bonding forces in addition to the weaker vdW forces. The non-functionalized graphene-epoxy interface model with higher crosslink density has less polymer molecules moving freely and therefore more fixed in the network. As such, there are more portions of the network which remain within van der Waals interaction range and better distribute that load through the network such that increasing crosslink density leads to higher peak traction in the normal mode separation and increased averaged separation energy. This demonstrates that increasing the crosslink density of the epoxy polymer matrix, a better load transfer ability of the graphene-epoxy interface can be obtained.

5.8 Influence of Temperature Effects on the Non-functionalized Interface

In addition to the 100K results presented in Figure 5.8(a), opening mode separation simulations have been conducted at 300K in order to investigate the influence of temperature on the force-separation response for the non-functionalized CNT-epoxy interface. The opening mode force vs displacement curves at 100K and 300K for cases with different crosslink densities are provided in Figure 5.14. The 100K and 300K force-separation responses show similar trends, beginning with a rapid increase to peak force (peaking at 4-13 angstroms of displace-

Table 5.3: Peak force (pN) , separation energy (mJ/m^2) and separation distance ($\mathring{A}$)for all non-functionalized realizations at 100K and 300K

Temp	Realization	Crosslink density	Peak force	Separation energy	Separation distance
100K	1	86%	10.00	552	58.2
	2	86%	9.44	529	55.0
	3	86%	9.94	479	34.6
	average	86%	9.79	520	49.3
	4	53%	8.00	664	53.0
	5	53%	6.00	391	39.6
	6	53%	6.00	360	33.4
	average	53%	6.67	472	42.0
300K	1	86%	3.00	353	63.9
	2	86%	3.09	279	58.0
	3	86%	2.59	232	65.0
	average	86%	2.89	288	62.3
	4	53%	1.00	48.0	29
	5	53%	0.94	46.8	23.7
	6	53%	1.41	53.4	19.9
	average	53%	1.12	49.4	24.2

ment), and followed by a gradual decrease in force with increasing graphene separation until full separation. However, it is observed that the peak forces at 300K are much lower than that at 100K, therefore leading to a much smaller separation energy for the 300K case. This implies that the increased kinetic energy of the polymer atoms near the interface associated with the increase in temperature leads to a weaker nanoscale interface, and indicates the macroscale effective properties will likewise display temperature dependence.

The temperature effect on the load transfer ability is also noted to be different for the non-functionalized graphene-epoxy interface models with different degrees of crosslinked polymer matrix. The decrease of the peak force for the interface model with high crosslink density at 300K is not as much as the decreasing observed for the interface model with low crosslink

density, 69% decrease vs 90.9% decrease in peak force for 86% and 53% crosslink densities, respectively. In addition, an increasing separation distance is also observed for the 86% crosslinked case at 300K. This implies that the load transfer ability of the interface becomes less sensitive to the temperature effects by increasing the crosslink density in the thermoset polymer matrix(58% decreased separation energy for 86% crosslink density case vs 91.5% decreasing for 53% crosslink density case).

5.9 The influence of functionalization of the interface at varying temperature

As the OPLS potential does not generally include bond breaking, strain energy failure criteria are defined for certain covalent bonds in the polymer matrix and the functional groups as identified in Table 5.4 in order to enable bond breaking during the separation. The bond energy E_b^i of the i^{th} covalent bond is checked every certain number of time steps, e.g. 10000 in a simulation involving 0.1 femtosecond(fs) time steps. Once the bond energy for a given covalent bond reaches the strain energy failure criterion, the bond is disconnected and the associated angles and dihedral bonds are deleted.

Normal mode force-separation simulations have been conducted for the functionalized representative interface elements with 2 functional groups at both 100K and 300K to investigate the influence of functionalization on the load transfer ability of the interface at the different

Table 5.4: Strain energy failure criteria for covalent bonds.

Covalent bonds	Strain energy failure criterion(Kcal/mole)
CT-CT	83.17
CT-OH	86.04
C-OH	86.04
C-CA	83.17
CA-CA	83.17
CA-CT	83.17
CT-N2	74.61
CA-N2	74.61

temperature. Figure 5.15(a) compares the force-separation responses for the functionalized and non-functionalized graphene-epoxy interface models at 100K and 300K. It is noted that generally three regions are observed in the normal mode force-separation responses for the functionalized graphene-epoxy interface at both 100K and 300K versus two regions for the non-functionalized interface. The first region displays a monotonically increasing loading of the interface similar to the loading region observed in the non-functionalized interface. This region is believed to describe the force response of the interface associating with the stretching of the crosslinked network of the epoxy polymer. In the second region, as opposed to beginning to unload after reaching the peak force as in the non-functionalized interface, in the functionalized interface models the loading stabilizes for a brief period where the force plateaus or even slightly decreases. It is believed that this region of the force-separation response is associated with the slip of local network regions within the epoxy as it rearranges (sometimes as evidenced by observable voids) before loading of the network segments attached to the functional groups, and therefore is again similar to the non-functionalized interface response but in its unloading region. In the third region, the functionalized inter-

face demonstrates the force-separation responses having saw tooth shapes with sharp and steady increasing loading and subsequent dramatic drops while the non-functionalized interface is observed to have the force gradually decrease and eventually go to zero implying the degradation and final failure of the interface. Therefore, it is believed that region 3 in the functionalized interface is attributed to the functional groups participating in the load transfer as shown in the snapshots in Figure 5.15(c), and is characterized by the large peak force with following sharp drops denoting the failure of the covalent bonds inside the epoxy polymer or the functional groups. As the epoxy polymer has a crosslinked network, it is noted that both functional groups grafted between the graphene sheet and the epoxy matrix participate in the load transferring at the interface which corresponds to the two loading and subsequent unloading segments in the third region of the force-separation responses. At both 100K and 300K, significant increasing has been observed for peak force(5.7 times at 100K and 11.1 times at 300K), separation energy(21.6 times at 100K and 14.9 times at 300K) and separation distance(1.5 times at 100K and 0.5 times at 300K) in the normal mode separation of the functionalized interface relative to the non-functionalized interface. This indicates that theoretically the interface does become stronger by the functionalization treatment at various temperature, which leads to improved load transfer ability at the interface.

In Figure 5.15(a), the effects of temperature effect have been observed on the response of the functionalized interface in the normal mode separation. Region 1 mirrors the non-functionalized interface behavior in the normal mode separation where the temperature effect has been observed to result in a decrease in the peak force of region 1 with increase in

temperature. In region 3, both peak force and separation distance demonstrates decreasing with the increasing temperature for the functionalized interface and therefore the decreasing total separation energy, which indicates the elevated temperature also reduces the strength of the functionalized interface.

Comparison has been done of the load transfer abilities of the functionalized graphene-PE interface and the functionalized graphene-epoxy interface both having 5 functional groups in Figure 5.16 . The traction-separation relations show that the functionalized graphene-epoxy interface demonstrates a higher peak traction (4.23 GPa), much longer separation distance (179Å) and therefore significantly increased separation energy (16600 mJ/m^2) compared to the functionalized graphene-PE interface (4.03 GPa, 40.8Å and 7560mJ/m^2). This is in stark contrast to the comparison of the non-functionalized interface response of the two material system, which demonstrated very similar normal mode force-separation responses. This indicates that the load transfer ability of the graphene-epoxy interface can be improved more efficiently through functionalization relative to the graphene-PE interface as we expected due to the crosslinked network of epoxy polymer matrix.

5.10 Macroscale effective elastic properties of CNT-epoxy nanocomposites with non-functionalized interface

It is observed that the force-separation responses of the graphene-epoxy interface at varying temperature exhibits similar trends as those of the graphene-PE interface. As shown in Figure 5.17, the cohesive zone traction-displacement laws developed for the non-functionalized graphene-epoxy interface have a bilinear form in the normal direction keeping the separation energy obtained from MD simulations while in the sliding direction the cohesive zone law rises to the peak traction and then stay at the peak value as the interface is assumed to stay contact in the sliding separation.

Adopting the 2-D RVE as in Chapter II, the in-plane properties, i.e. the stiffness components C_{22}, of the transversely isotropic effective nanocomposites is calculated using finite element analysis based on the volume averaged stresses and strains. The stress contour and deformed configuration of the nanocomposites at a CNT vf of 0.1 are shown in Figure 5.18 corresponding to the C_{22} and C_{66} boundary conditions, respectively. It is observed that the cohesive zones in the interface regions are experiencing different loading conditions, i.e some are in the initial loading region and some have fully separated. Table 5.5 gives the percentage reduction of C_{22} and C_{66} relative to their counterpart perfect bonding values at 100K and 300K for the CNT-epoxy nanocomposites at CNT vfs of 0.1 and 0.5. Effective C_{22}

and C_{66} at 100K and 300K are provided in Figure 5.19 with applied strain for CNT-epoxy nanocomposites with a CNT vf of 0.1, respectively. For perfect bonding cases, C_{22} and C_{66} are calculated for a small strain range of 0-0.1 wherein both of them are constant and independent of temperature and applied load levels. For cohesive zone models, C_{22} is constant in the strain range of 0-0.3 and then begins to decrease non-linearly with further increasing of the applied load. This transition corresponds to the loading and unloading regions of the normal cohesive zone law, which indicates that the C_{22} is dominated by the normal mode separation of the cohesive zone elements. As for C_{66}, it demonstrates a initial increasing which leads to the maximum value around the transition strain level observed in the C_{22} results and then a subsequent decreasing. The different response of C_{66} relative to the applied load attributes to the weaker sliding mode separation of the interface and a transition of cohesive zone being primarily loaded in sliding mode to the normal mode with the increasing of the applied shear strain. The transition strain level of C_{22} and C_{66} for the epoxy based nanocomposites at a CNT vf of 0.1 is higher than that for the PE based nanocomposites with the same amount of CNTs. This corresponds to the different displacements at the peak traction in the cohesive zone traction-displacement laws for the CNT-PE(around 1.82Å) and CNT-epoxy(around 5.26Å) interface, which demonstrates the nanoscale interface effects on the effective material properties of the nanocomposites as the amorphous PE matrix are more readily slip off the graphene sheet than the crosslinked network of the epoxy polymer.

The effective in-plain bulk modulus K_{23} is calculated by using the relation $K_{23} = C_{22} - C_{66}$. Table 5.5 gives the reduction in K_{23} at 100K and 300K relative to the perfect bonding case

Table 5.5: Reduction of C_{22} and C_{66} in computational micromechanics (FEA) for cohesive zone model with respect to the perfect bonding model for 0.1, and 0.5 volume fraction. Values are reported in terms of loading/unloading stages.

CNT vf	% reduction at 100 K			% reduction at 300 K		
	C_{22}	C_{66}	K_{23}	C_{22}	C_{66}	K_{23}
10%	32.0 -36.0%	28.4 -27.3%	33.0 -39.0%	35.3 -35.8%	32.8 -27.6%	36.0 -39.0%
50%	86.6 -88.7%	84.7 -80.8%	88.0 -92.0%	90.1 -90.0%	90.1 -83.5%	90.0 -93.0%

at CNT vfs of 0.1 and 0.5. In Figure 5.20, K_{23} is observed to decrease initially in the small strain region of 0-0.1, stay constant in the range of 0.1-0.3 and then decrease non-linearly with the increasing strain, which shows the significant effects of mode mixity. Compared with the perfect bonding case, the cohesive zone cases yield lower K_{23}, which shows dependency temperature, applied load and vf of CNTs. It is expected that the functionalization of the interface can enhance the strength of the interface and therefore the macroscale effective material properties of the CNT-reinforced polymer nanocomposites.

5.11 Macroscale effective elastic properties of functionalized CNT-epoxy nanocomposites

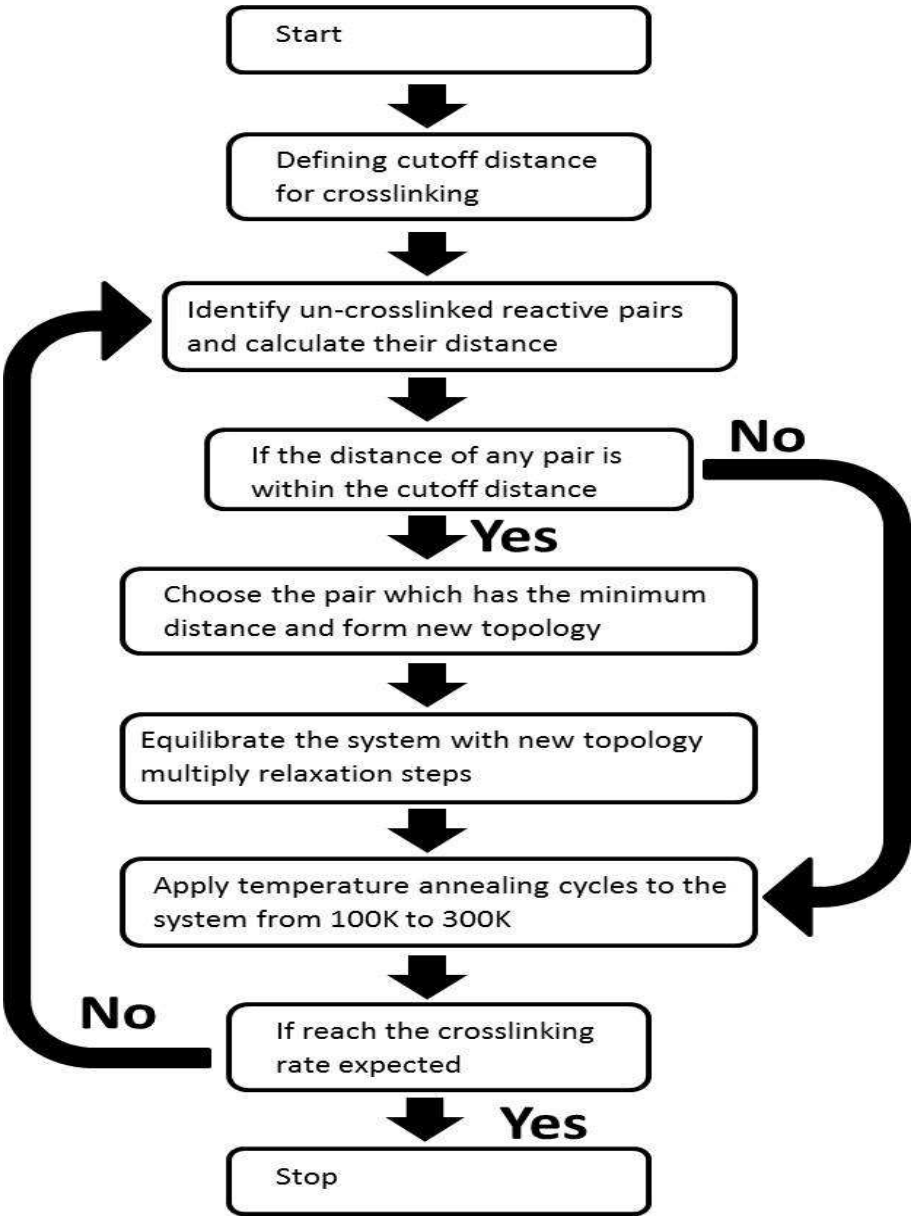

Figure 5.5: The flowchart of the algorithm designed for the crosslinking process

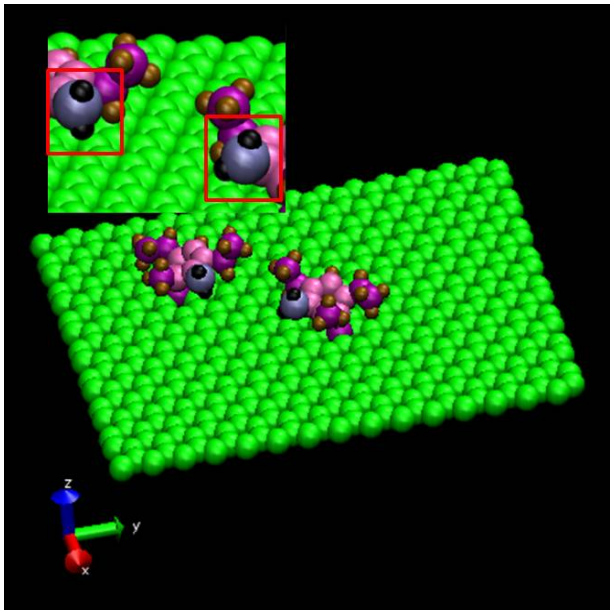

Figure 5.6: The configuration of the graphene sheet with the grafted functional groups having amine groups labeled by the red rectangles.

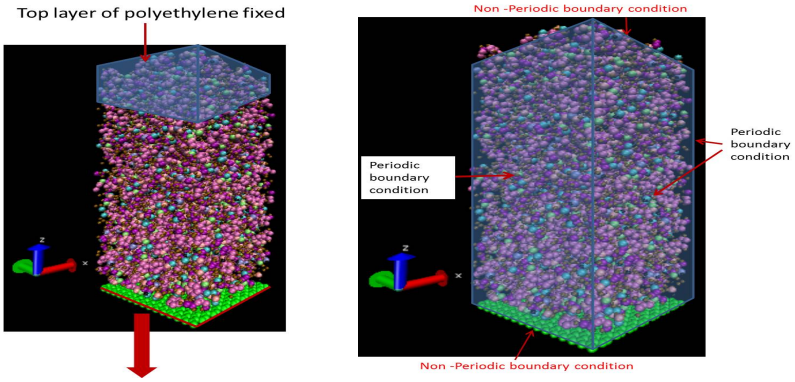

(a) (b)

Figure 5.7: Constraints with the arrow indicating the direction of the velocity on graphene sheet(a) and boundary conditions(b) for representative interface element(10c80c case) in normal mode separation. r in parametric study is defined in (a) as $r = \frac{D}{L}$.

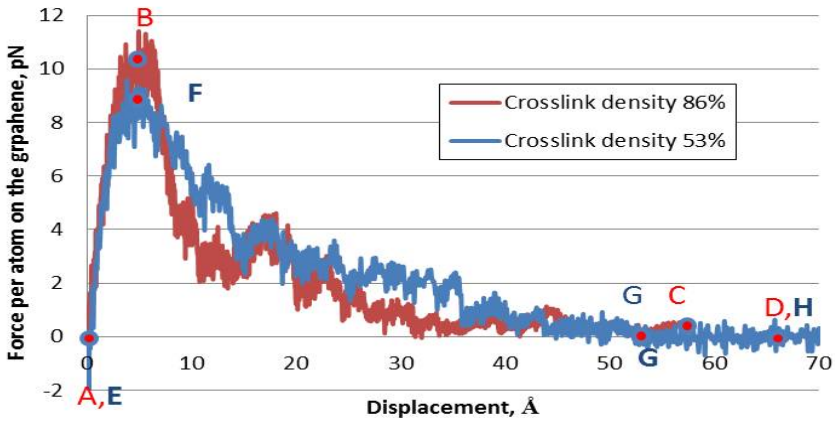

(a)

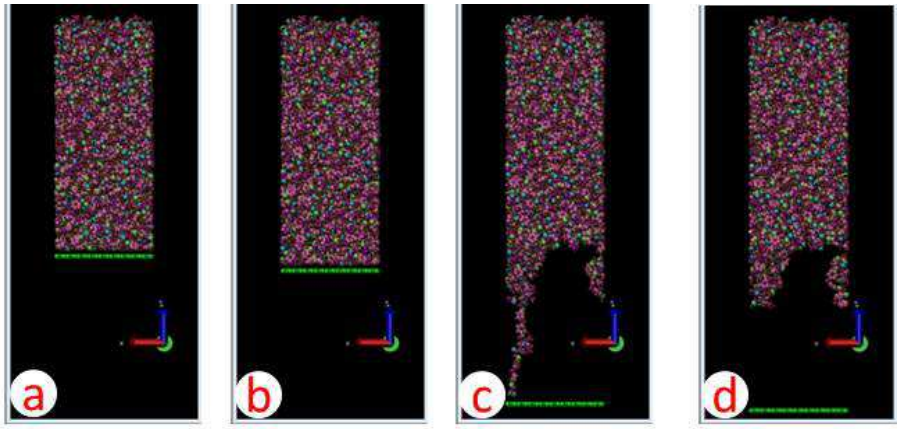

(b)

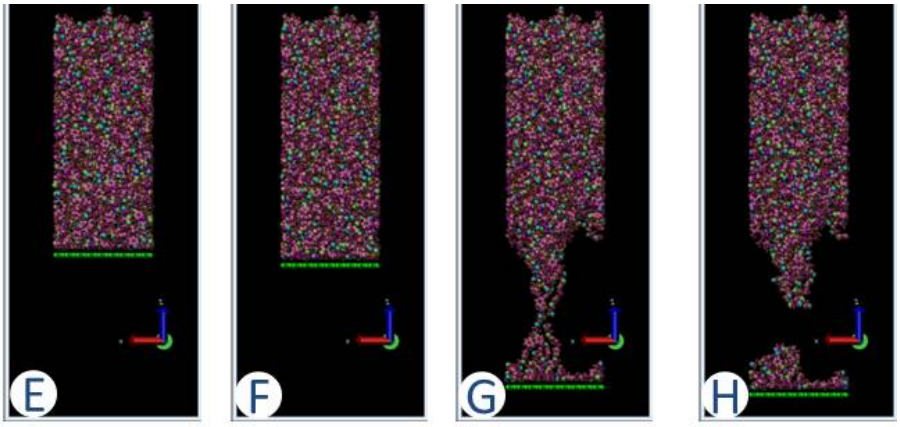

(c)

Figure 5.8: The comparison of force-separation responses for the normal mode separation of the non-functionalized graphene-epoxy interface models with crosslink density of 53% and 86%. (A) and (H) give the snapshots of the non-functionalized graphene-epoxy interface models during the normal mode separation corresponding to the points labeled in the force-separation responses.

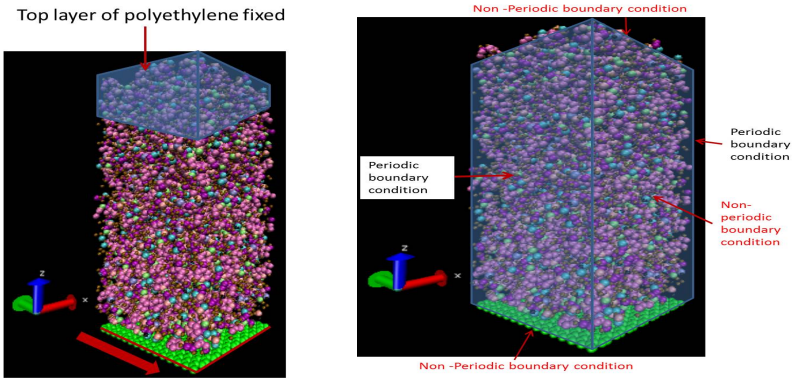

(a) (b)

Figure 5.9: Constraints with the arrow indicating the direction of the velocity on graphene sheet(a) and boundary conditions(b) for representative interface element(10c80c case) in sliding mode separation. r in parametric study is defined in (a) as $r = \frac{D}{L}$.

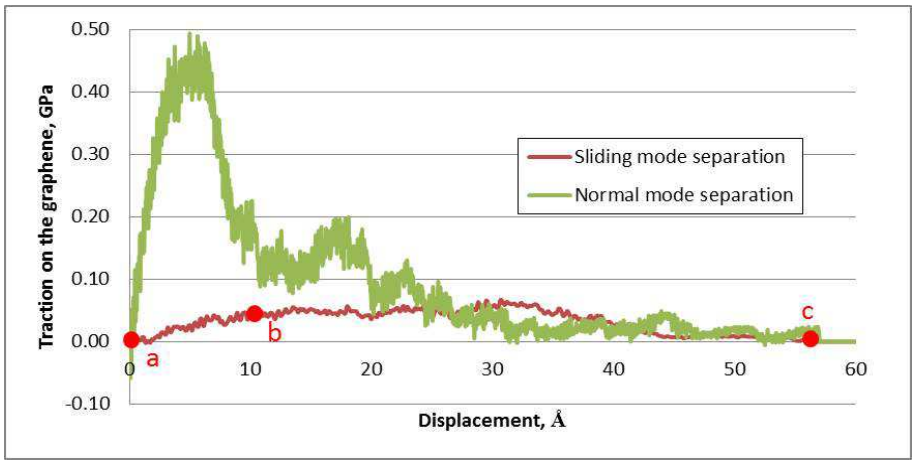

(a)

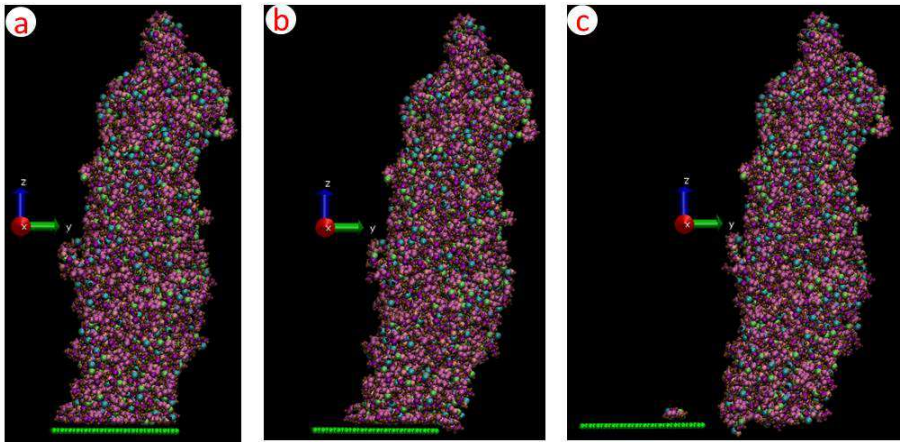

(b)

Figure 5.10: Traction-separation responses for the sliding mode and normal opening mode separations(a) of the non-functionalized graphene-epoxy interface models with snapshots for the sliding mode separation (b).

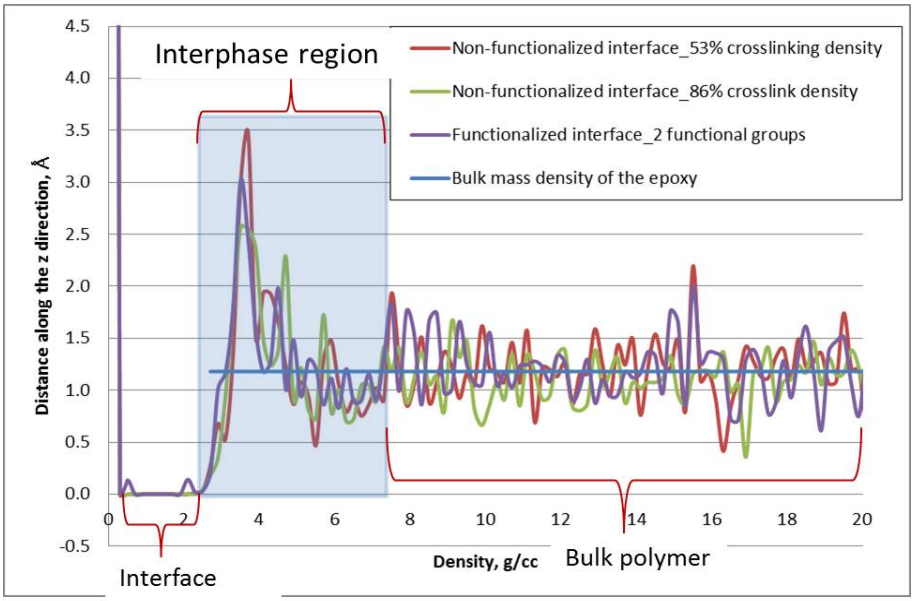

Figure 5.11: The density profiles of the non-functionalized and functionalized graphene-epoxy representative interface elements with various crosslink densites in the z dimension.

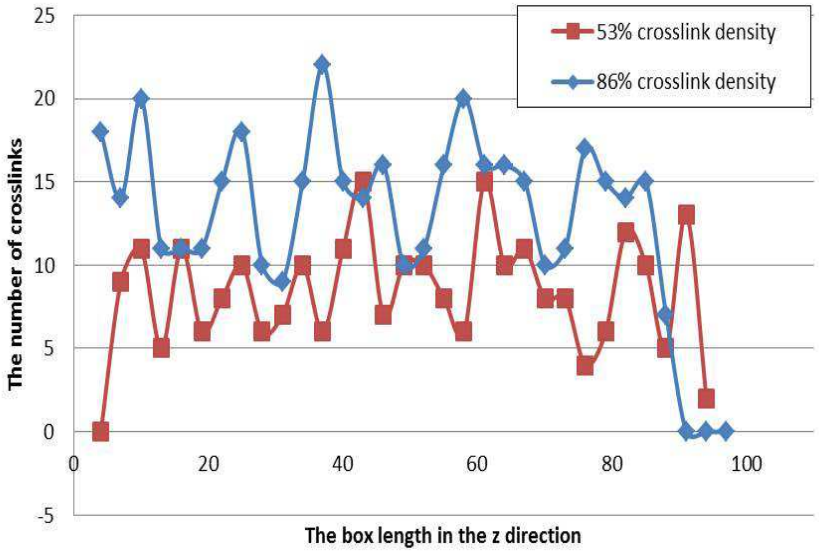

Figure 5.12: The distribution of the crosslinks in the epoxy polymer matrix along the z dimension inside the non-functionalized and functionalized graphene-epoxy representative interface elements with various crosslink densites.

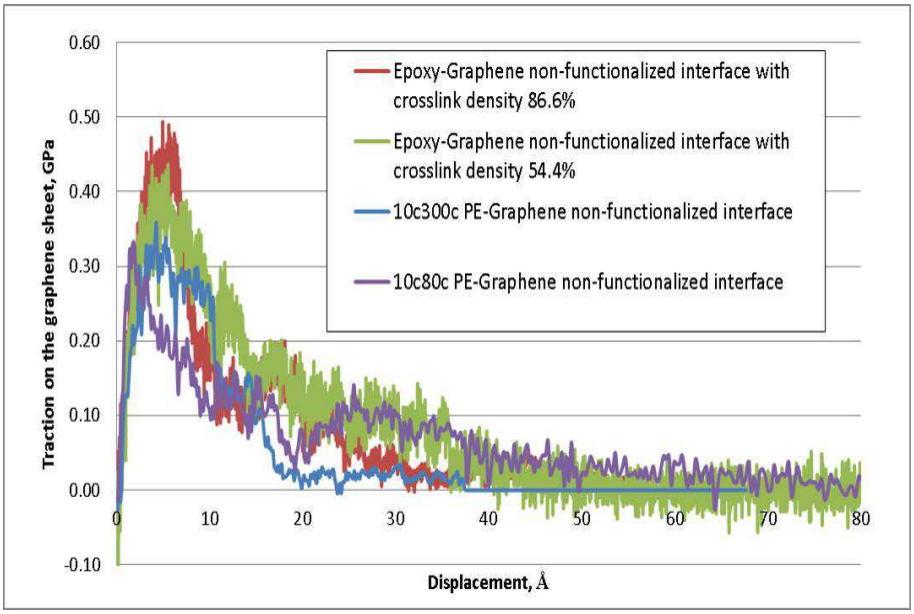

Figure 5.13: The normal mode traction-separation responses for the non-functionalized graphene-PE interface models with different length of polymer chains (80 vs 300) and the non-functionalized graphene-epoxy interface models with different crosslink densities (53% vs 86%).

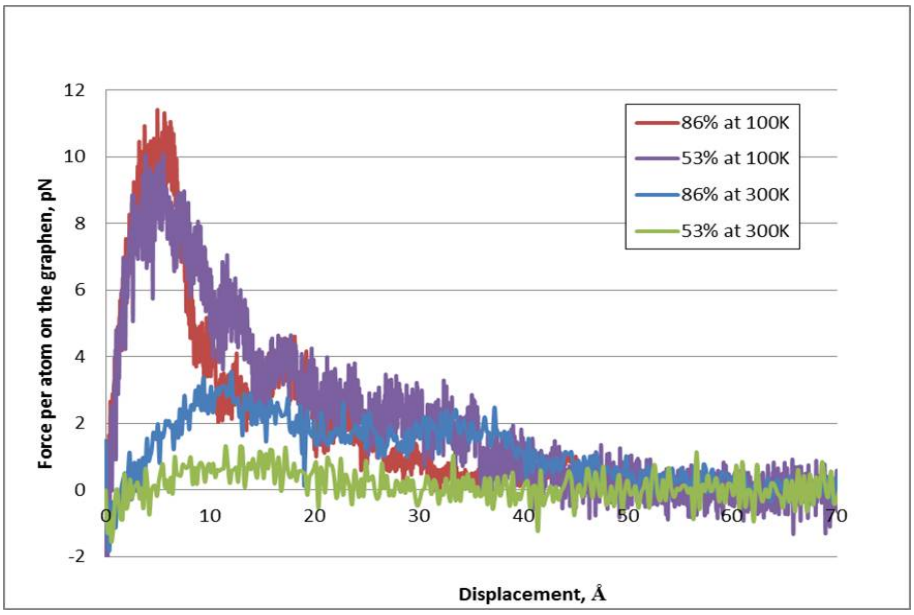

Figure 5.14: Comparison of normal mode force-separation responses at 300K and 100K for the graphene-epoxy interface models with crosslink density of 53% and 86%.

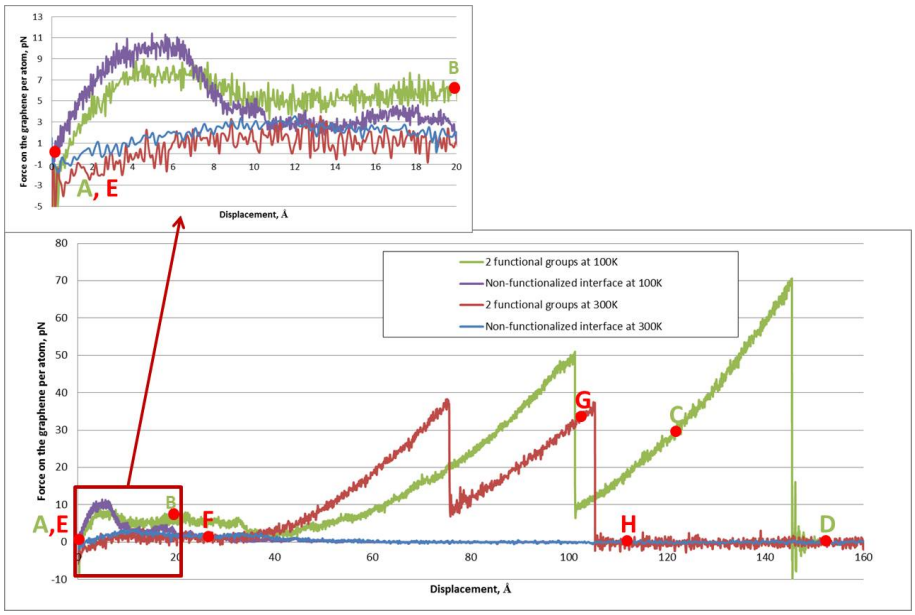

(a)

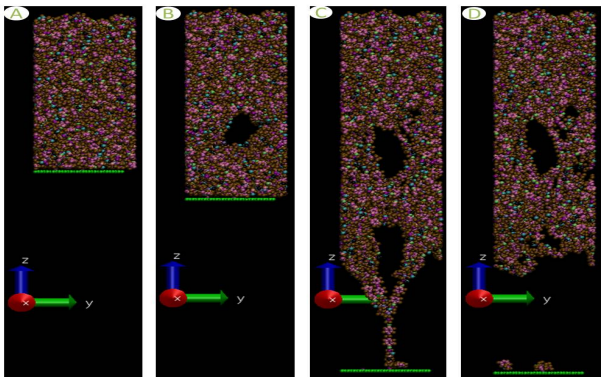

(b)

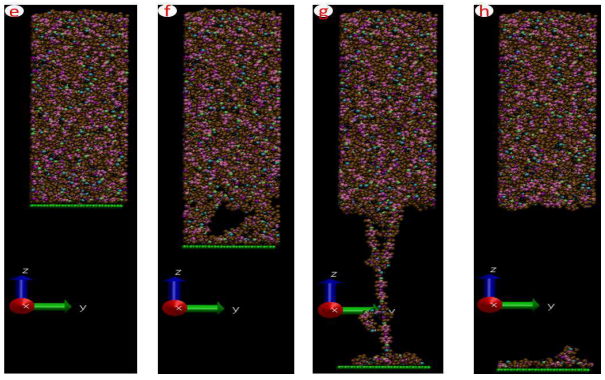

(c)

Figure 5.15: Normal mode force-separation responses for the functionalized and non-functionalized graphene-epoxy interface models with 86% crosslinked epoxy polymer at 100K and 300K. Snapshots corresponding to points labeled in the force-separation responses are shown in (b) and (c)

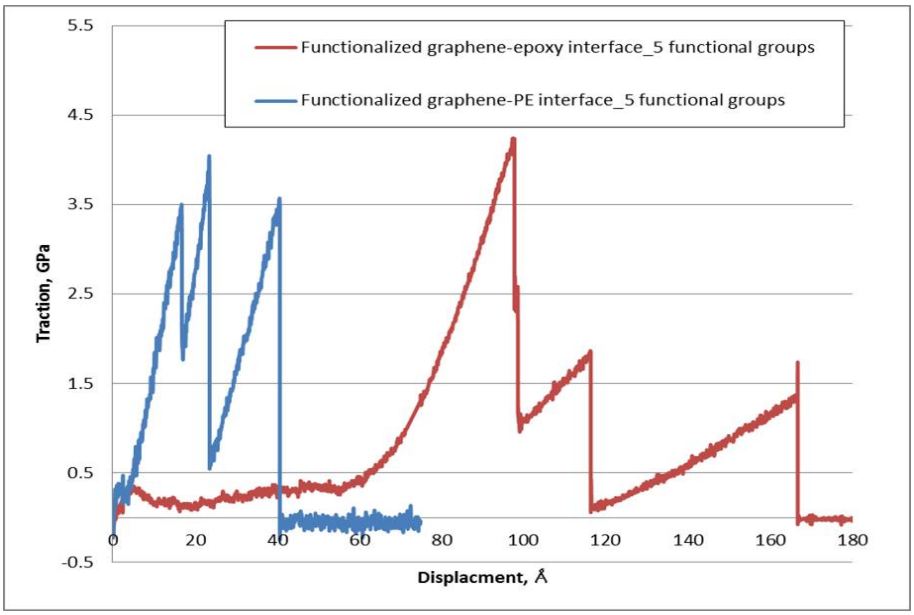

Figure 5.16: Comparison of normal mode traction-separation responses at 100K for the functionalized graphene-epoxy interface model with crosslink density of 86% and and the functionalized graphene-PE interface model.

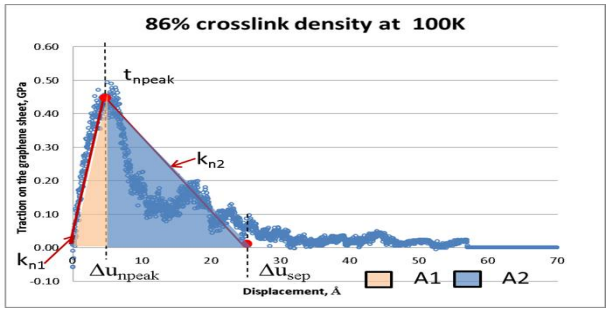

(a)

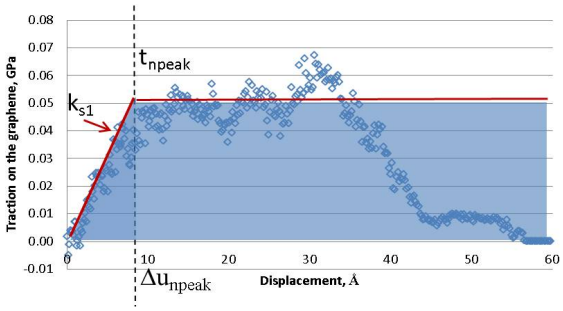

(b)

Figure 5.17: MD cohesive zone traction-displacement laws and corresponding bilinear cohesive zones laws for the graphene-epoxy interface in normal and sliding mode separation at 100K

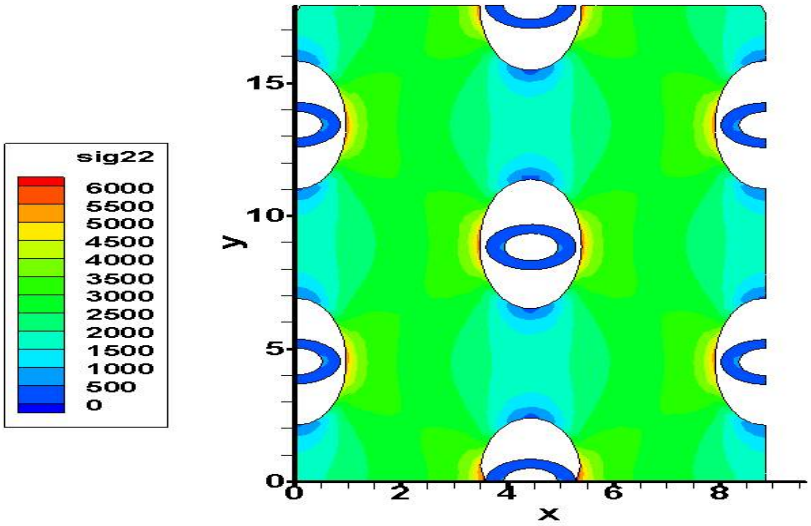

(a)

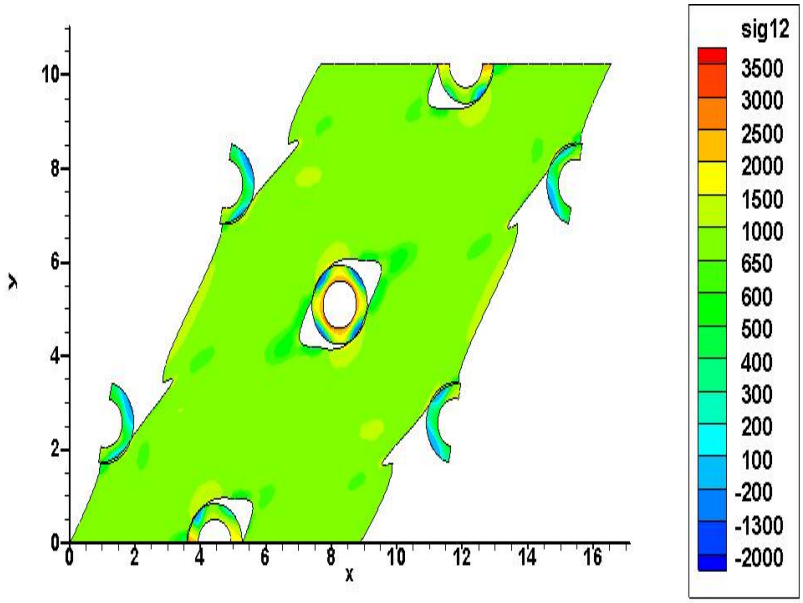

(b)

Figure 5.18: (a) shows deformation of computational RVE with the stress contour σ_{yy}(MPa) for Vf 0.1 CNT-epoxy nanocomposites under 0.75 strain loading with the displacement loading condition and the boundary conditions used for C_{22} stiffness components calculation and (b) shows deformation of computational RVE with the stress contour σ_{xy}(MPa) for Vf 0.1 CNT-epoxy nanocomposites under 0.75 strain loading with displacement loading condition and the boundary conditions used for C_{66} stiffness components calculation.

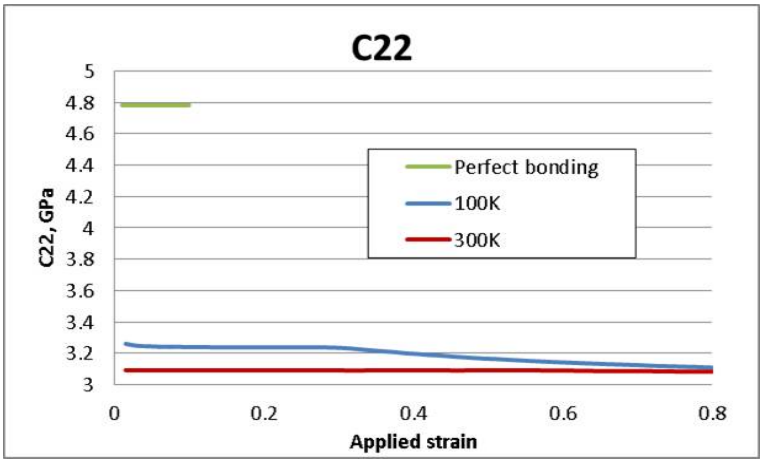

(a) C_{22}

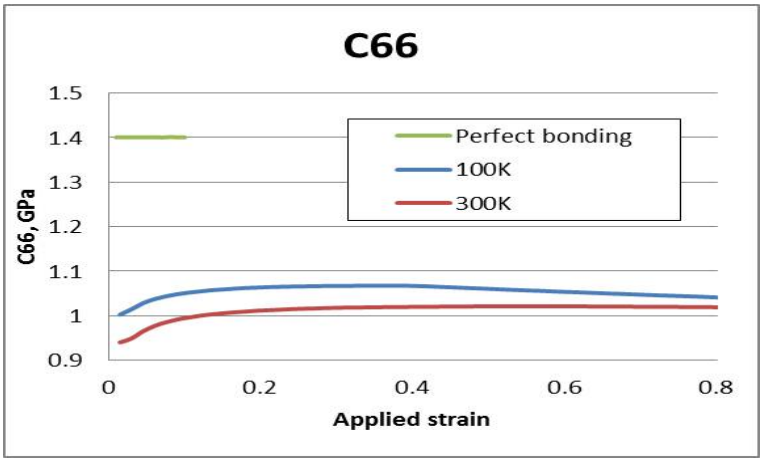

(b) C_{66}

Figure 5.19: Macroscale effective C_{22} and C_{66} stiffness components at 100K and 300K for 0.1 vf CNT-epoxy nanocomposites for perfect bonding and cohesive zone cases obtained from FEA-based computational micromechanics approach

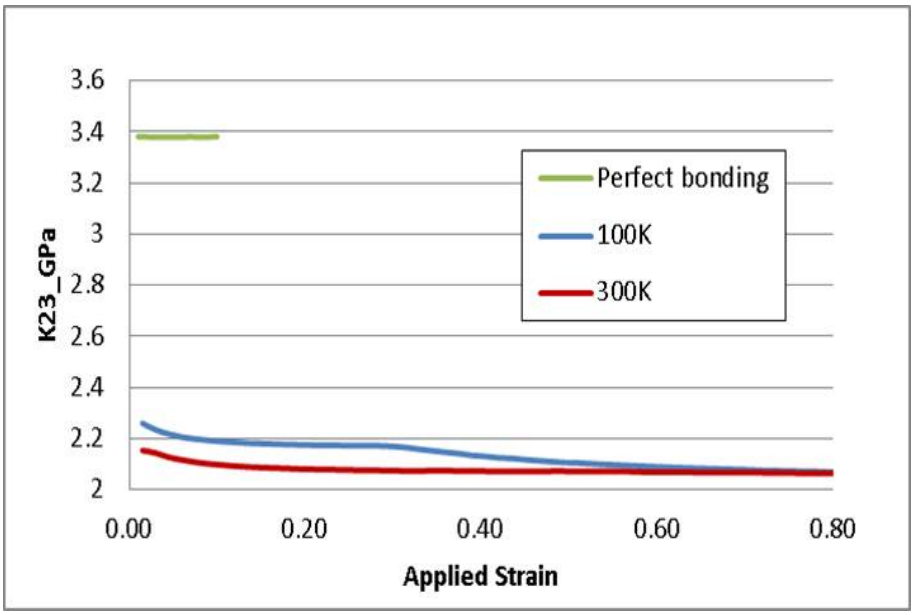

Figure 5.20: Macroscale effective K_{23} for CNT-epoxy nanocomposites with a CNT volume fraction of 0.1 for perfect bonding and cohesive zone cases from FEA-based computational micromechanics approach at 100K and 300K

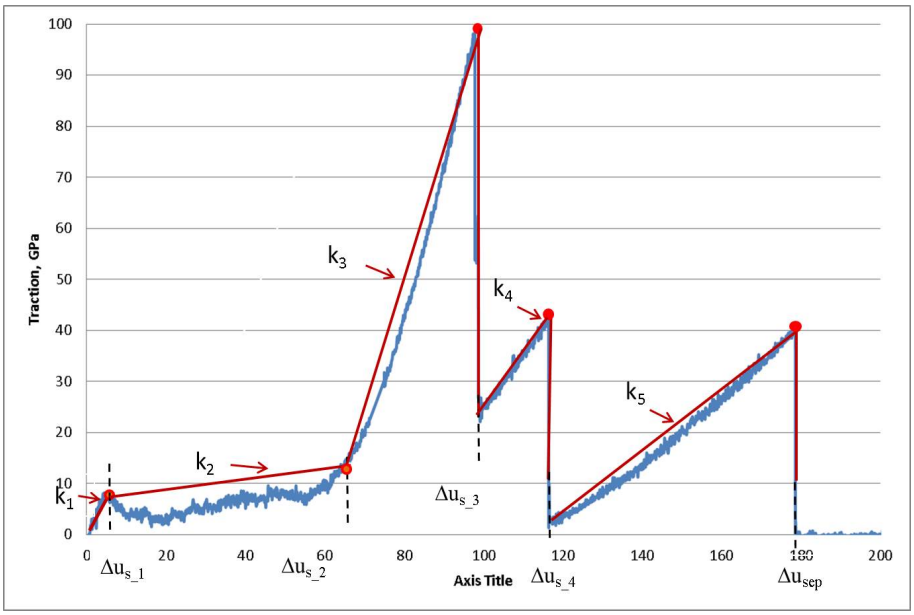

Figure 5.21: Cohesive zone law developed based on the force-separation response of the functionalized graphene-epoxy interface in MD simulations.

Cohesive zone laws are developed for the functionalized graphene-epoxy interface as shown in Figure 5.21 which have a similar form as those developed for the functionalized graphene-PE interface where the focus is on retaining all the local peak tractions and the relative displacements where the local peak tractions are reached.

The 2-D hexagonal RVE at a CNT vf of 0.1 is shown in Figure 5.22 in the deformed configurations with the stress contour corresponding to the boundary conditions for determining C_{22}. It is observed that the cohesive zones in the interface regions are experiencing different loading conditions, i.e they are in the loading regions with varying stiffnesses K_n. Effective C_{22} at 100K is provided in Figure 5.23 as a function of applied strain for CNT-epoxy nanocomposites with a CNT vf of 0.1. C_{22} of the CNT-epoxy nanocomposites with the functionalized

interface decreases gradually with the increasing of the applied strain which is associated with the decreasing stiffness of cohesive zone elements. Relative to C_{22} of the nanocomposits with non-functionalized interface, 6%-3% increasing is observed for C_{22} of the CNT-epoxy nanocomposites at 100K through functionalization in the strain range of 0-0.8. It is observed that when grafted with the same number of functional groups, the graphene-epoxy interface demonstrates much higher load transfer capacity than the graphene-PE interface in terms of separation energy and peak separation traction. However, as for C_{22}, the percentage increase obtained through functionalization for the CNT-epoxy nanocomposites (6%-3%) is not higher than that for the CNT-PE nanocomposites (2%-12%). This results from the late engagement of the functional groups in transferring load for the functionalized graphene-epoxy interface as shown in Figure 5.16 indicated by the wide region 1 and region 2 in the traction-separation response. Within the range of the applied strain to the RVE, most of the cohesive zone elements of the CNT-epoxy interface remain in their respective region 1 and 2 portion of the cohesive zone laws which were associates with the stretching and slipping of the epoxy network before loading of the functional groups. To fully engage the region 3 portions of the CNT-epoxy interface, higher strain levels, perhaps associated with higher degrees of local clustering, are needed, though such strain levels may not be achievable as the portions of the epoxy matrix may damage and fracture before such strain levels near the CNT interface are achieved.

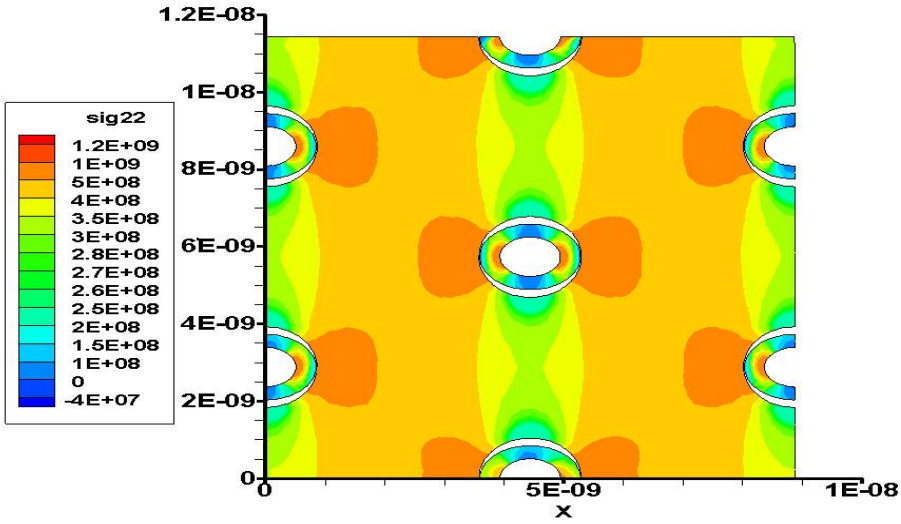

Figure 5.22: The deformation of computational RVE with the stress contour σ_{yy}(Pa) for Vf 0.1 CNT-epoxy nanocomposites under 0.24 strain loading.

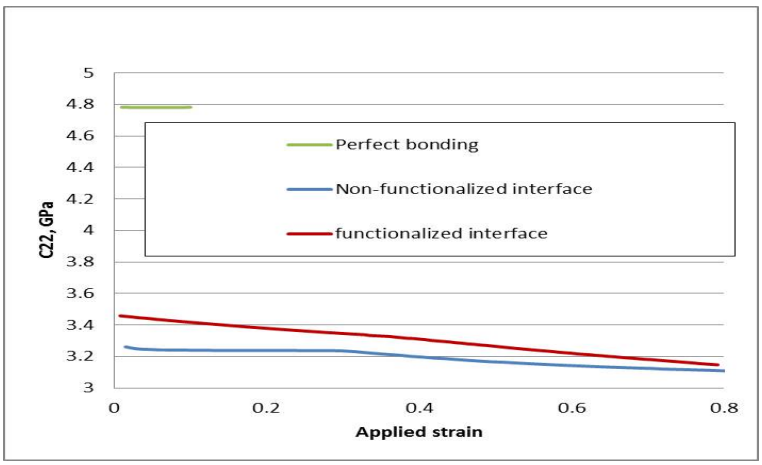

Figure 5.23: Macroscale effective C_{22} stiffness component at 100K for 0.1 vf functionalized CNT-epoxy nanocomposites for perfect bonding and cohesive zone cases obtained from FEA-based computational micromechanics approach

5.12 Conclusions

MD simulations were conducted to characterize the behavior of the non-functionalzied and functionalized interface between CNTs and the epoxy matrix in both normal opening and sliding separations in terms of force-separation responses in order to investigate the load transfer ability at the interface in the CNT reinforced epoxy nanocomposites. With thermoset polymer matrix material, the influence of the crosslink density and the system temperature have been investigated on the load transfer ability of the non-functionalized interface during the separations. The effect of functionalization on the load transfer ability at the graphene-epoxy interface is explored at varying temperature.

A dynamic crosslinking process was developed to prepare the epoxy matrix with various crosslink densities in order to investigate the influence of the crosslink level of the epoxy matrix on the load transfer ability at the interface between CNTs and the epoxy matrix. In order to verify the interface model, the distributions of the crosslinks and the local density in the epoxy matrix with varying crosslink densities were studied with the presence of the graphene sheet. No bias is observed for the distribution of the crosslinks inside the epoxy matrix along the z-direction. The profile of the local density along the z-direction for the epoxy matrix, which is related to the interaction between the graphene sheet and the epoxy matrix, is consistent with the observations in the literature. These observations indicated that a reasonable configuration of the crosslinked epoxy matrix was obtained from the developed dynamic crosslinking process. For the normal mode separation of the nonfunctionalized

interface, the typical force-separation responses are observed to have two regions, which have a sharp initial loading region and subsequent slow unloading region after reaching the peak force. The nonfunctionalized interfacial force-separation response in the sliding direction has a plateau region with a value around the peak force after an initial loading region and followed by a relative shorter unloading region. The peak force is much lower in the sliding direction than in the normal direction, which indicates a weaker interface in the sliding direction.

The non-functionalized graphene-epoxy interface models with 53% crosslinked and 86% crosslinked epoxy matrix were characterized and compared in order to study the influence of the crosslink density on the behavior of the non-functionalized interface. It was observed that the non-functionalized interface with 86% crosslink density has a higher averaged peak force and averaged separation energy in the normal mode separation comparing to the non-functionalized interface with 53% crosslink density. This indicated that the epoxy matrix with higher crosslink density can contribute to forming a stronger non-functionalized graphene-epoxy interface. Comparison of the force-separation responses of the non-functionalized graphene-PE interface and the non-functionalized graphene-epoxy interface were also made which demonstrates that higher peak traction and larger separation energy were observed for the non-functionalized graphene-epoxy interface. This observation implies the application of the thermoset polymer matrix can attribute to stronger interfacial interactions in the CNT-reinforced nanocomposites. Temperature effect on the load transfer ability of the non-functionalized graphene-epoxy interface was investigated and a 69-90%

decreased peak force and 58-91.5% decreased separation energy were observed, which indicated that the elevated temperature can reduce the strength of the interface significantly. It was also noted that the non-functionalized graphene-epoxy interface with 53% crosslinked epoxy matrix has peak force and separation energy decreased by 90.8% and 91.5% respectively, while only 69% and 58% decrease were observed for those of the non-functionalized graphene-epoxy interface with 86% crosslinked epoxy matrix. This demonstrated that increasing the crosslink density of the epoxy matrix can weaken the temperature effect, i.e. reduce the reduction of the strength of the interface at the elevated temperature.

Significant enhancement of the load transfer was observed for the functionalized graphene-epoxy interface in the normal opening separation at both 100K and 300K. As a result of the crosslinked polymer matrix, both of 2 functional groups are observed to engaged under load and are associated with the two sharp loading segments and subsequent dramatic drops in the third region of the functionalized interface response. For the functionalized graphene-epoxy interface, peak force and separation energy in the normal mode separation have been increased by 5.6 and 21.6 times at 100K, and by 11.1 and 14.9 times at 300K, which demonstrates functionalization can improve the load transfer ability at the interface significantly.

Finite element implementation of cohesive zone models was used to investigate the nanoscale interface effects on the macroscale mechanical performance of the non-functionalized/functionalized CNT-epoxy nanocomposites. It is observed that relative to the perfect bonding case, the inclusion of the interface effects by embedding cohesive zone models in FEM yields lower

K_{23} for the CNT-epoxy nanocomposites, and a macroscale effective elastic property response which demonstrates temperature dependency, volume fraction and load dependency. Through functionalization, it was noted that enhanced C_{22} was obtained for the CNT-epoxy nanocomposites when compared to the nanocomposites with the non-functionalized interface.

The load transfer ability of the non-functionalized graphene-epoxy interface has been observed to have dependence on the crosslink density of the epoxy matrix, the temperature and the separation mode. Through functionalization, improvement has been noted for the load transfer ability associating with a stronger interface and the effective material properties of the CNT-epoxy nanocomposites, which is consistent with the experimental results in the literature [30, 35].

Chapter 6

Conclusions and summations

In the present work, a multiscale model is provided to investigate the macroscale effective material performance of the CNT-reinforce polymer nanocomposites under the nanoscale load transfer ability of the non-functionalized or functionalized interface by bridging the atomistic modeling with continuum micromechanics approaches using cohesive zone models. A brief review of molecular dynamic simulations and cohesive zone models has been provided. The atomistic interface models have been constructed to characterize the load transfer capability at the interface between CNTs and the polymer matrix in CNT-reinforced nanocomposites in terms of sensitivity to parameters such as temperature, sliding mode, the length of polymer chains and numbers for the thermoplastic polymer matrix and the crosslink density for the thermoset polymer matrix. Cohesive zone laws were developed based on traction-separation interface responses for normal opening and sliding mode separations at the nanoscale. The cohesive zones were applied in the analytic and computational micromechanics approaches

to predict the macroscale effective elastic properties under the influence of the nanoscale load transfer ability of the interface.

The use of the graphene sheet in constructing a representative interface element for the non-functionalized graphene-PE interface has been explored in terms of sensitivity to parameters such as the length of the polymer chains, the number of polymer chains, and relative position of the MD 'grip' to the interface, as well as the influences of curvature of the graphene sheet and temperature. The MD results demonstrated that at the nanoscale the load transfer ability of the interface is much lower in the sliding direction than in the normal direction and decrease with the elevated temperature, which indicates a dependence on the separation mode and the system temperature. The macroscale effective properties determined from the micromechanics approaches was observed to experience significant depreciation compared to the perfect bonding cases when the interface model was included and exhibit strain, temperature and CNT volume fraction dependence. This indicates the interface may be the source of overprediction of the material properties of CNT based nanocomposites in the literatures.

The effects of functionalization were investigated on the effective mechanical material properties of CNT-PE nanocomposites. CVFF is modified by adding strain energy criteria for all carbon-carbon covalent bonds to allow for bond breaking. Significant improvement has been observed for the load transfer ability of the functionalized interface in both modified CVFF and AIREBO cases with the peak force increased by 15.3-21.6 times for the modified CVF-F cases and 9.06-25.7 times for the AIREBO cases as compared to the non-functionalized

graphene-PE interface model. Larger separation energy has also been observed for the interface with more functional groups in the normal mode separation which demonstrates higher functionlaization density can lead to the better load transfer ability of the functionalized interface. For the sliding mode separations, 5 functional groups cases demonstrated increased overall peak force and separation energy (43 and 99.6 times for the modified CVFF case and 4.87 and 10.4 times for the AIREBO case). Such observations suggest that the functionalized interface model has a nearly equal load carrying capability in both normal and sliding modes, which indicates significantly improved overall load transfer ability of the interface through the functionalization. The finite element implementation of cohesive zone model was applied to calculate macroscale effective mechanical property of the CNT-PE nanocomposites with the functionalized interface where improved C_{22} (2%-12%) relative to the CNT-PE nanocomposites with the non-functionalized interface was observed.

For nanocomposites with thermoset polymer matrix, a dynamic crosslinking process was developed to construct the epoxy matrix with various crosslink densities in order to investigate the influence of the crosslink level of the epoxy matrix on the load transfer ability at the interface between CNTs and the epoxy matrix. Comparison of the force-separation responses of the non-functionalized graphene-PE interface and the non-functionalized graphene-epoxy interface was made which demonstrates that higher peak traction and larger separation energy were observed for the non-functionalized graphene-epoxy interface. It was also observed that the non-functionalized interface with 86% crosslink density had a higher averaged peak force and averaged separation energy in the normal mode separation compared to the non-

functionalized interface with 53% crosslink density. It infers that the epoxy matrix with high crosslink density can contribute to form a stronger non-functionalized graphene-epoxy interface. Temperature effect on the load transfer ability at the non-functionalized graphene-epoxy interface was investigated and the 69-90% decreased peak force and 58-91.5% decreased separation energy were observed, which indicates that the elevated temperature can reduce the strength of the interface significantly. It was also noted that the non-functionalized graphene-epoxy interface with 53% crosslinked epoxy matrix had peak force and separation energy decreased by 90.8% and 91.5% respectively, while only 69% and 58% decreasing has been observed for those of the non-functionalized graphene-epoxy interface with 86% crosslinked epoxy matrix. It demonstrated that increasing the crosslink density of the epoxy matrix can weaken the temperature effect, i.e. reduce the reduction of the strength of the interface at the elevated temperature. Significant enhancement of the load transfer has been observed for the functionalized graphene-epoxy interface in the normal opening separation at both 100K and 300K. For the functionalized graphene-epoxy interface, peak force and separation energy in the normal mode separation have been increased by 5.6 and 21.6 times at 100K, and by 11.1 and 14.9 times at 300K, which demonstrated functionalization can improve the load transfer ability at the interface significantly. Applying cohesive zone models in the finite element framework, it was noted that C_{22} was increased by 6%-3% through functionalization for the CNT-epoxy nanocomposites when compared to the nanocomposites with the non-functionalized interface.

It was observed that the macroscale effective properties of non-functionalized CNT-polymer

nanocomposites determined from the micromechanics approaches experienced significant depreciation compared to the perfect bonding cases when the interface model was included. The temperature sensitivity of the interface was observed to directly transfer to the effective property calculations, which were also observed to be highly sensitive to the CNT volume fraction and applied load. For the functionalized interface, observing herein that the normal and sliding modes both yield significantly improved interfacial load transfer, the latter more so relative to its non-functionalized counterpart, it is expected that all effective elastic properties, especially those relying on shear load transfer, will be enhanced along with their durability under load. Improved C_{22} relative to the nanocomposites with the non-functionalized interface was observed for both functionlaized CNT-PE and CNT-epoxy nanocomposites, which indicates that the treatment of functionalization helps to improve the effective mechanical properties of the CNT-reinforced polymer nanocomposites.

Chapter 7

Bibliography

Bibliography

[1] Coleman, J., Khan, U., Blau, W., and Gun'ko, Y., "Small but strong: A review of the mechanical properties of carbon nanotube-polymer composites," *Carbon*, Vol. 44, No. 9, 2006, pp. 1624–1652.

[2] Falvo, M., Clary, G., Taylor II, R., Chi, V., Brooks Jr, F., Washburn, S., and Superfine, R., "Bending and buckling of carbon nanotubes under large strain," *Nature*, Vol. 389, 1997, pp. 582–584.

[3] Wong, E., Sheehan, P., and Lieber, C., "Nanobeam mechanics: elasticity, strength, and toughness of nanorods and nanotubes," *Science*, Vol. 277, 1997, pp. 1971–1975.

[4] McEuen, P., Fuhrer, M., and Park, H., "Single-walled carbon nanotube electronics," *IEEE Transaction on Nanotechnology*, Vol. 1, No. 1, 2002, pp. 78–85.

[5] Hone, J., Llaguno, M., Biercuk, M., Johnson, A., Batlogg, B., and Fischer, J., "Thermal properties of carbon nanotubes and nanotube-based materials," *Applied Physics A*, Vol. 74, 2002, pp. 339–343.

[6] Thostenson, E., ZF., R., and Chou, T., "Advances in the science and technology of carbon nanotubes and their composites: a review," *Compos. Sci. Technol.*, Vol. 61, 2001, pp. 1899–912.

[7] Awasthi, K., Srivastava, A., and Srivastava, O. N., "Synthesis of carbon nanotubes," *Journal of Nanoscience and Nanotechnology*, Vol. 5, 2005, pp. 1616–1636.

[8] Collins, P. and Avouris, P., "Nanotubes for Electronics," *Scientific American*, Vol. 283, 2000, pp. 62–69.

[9] Treacy, M., Ebbesen, T., and Gibson, J., "Exceptionally high Young's modulus observed for individual carbon nanotubes," *Nature*, Vol. 381, 1996, pp. 678–680.

[10] Cadek, M., Coleman, J., Barron, V., Hedicke, K., and Blau, W., "Morphological and mechanical properties of carbon-nanotube-reinforced semicrystalline and amorphous polymer composites," *Applied Physics Letters*, Vol. 81, No. 27, 2002, pp. 5123–5125.

[11] Qian, D., Dickey, E., Andrews, R., and Rantell, T., "Load transfer and deformation mechanisms in carbon nanotube-polystyrene composites," *Applied Physics Letters*, Vol. 76, No. 20, 2000, pp. 2868–2870.

[12] Tibbetts, G. and Mchugh, J., "Mechanical properties of vapor-grown carbon fiber composites with thermoplastic matrices," *Journal of Materials Research*, Vol. 14, 1999, pp. 2871–2880.

[13] Xiao, K., Zhang, L., and Zarudi, I., "Mechanical and rheological properties of carbon nanotube-reinforced polyethylene composites," *Composites Science and Technology*, Vol. 67, 2007, pp. 177–182.

[14] Kanagaraj, S., Varanda, F. R., Zhil'tsova, T., Oliveira, M., and Simoes, J., "Mechanical properties of high density polyethylene/carbon nanotube composites," *Composites Science and Technology*, Vol. 67, 2007, pp. 3071–3077.

[15] Yang, Z., McElrath, K., Bahr, J., and D'Souza, N. A., "Effect of matrix glass transition on reinforcement efficiency of epoxy-matrix composites with single walled carbon nanotubes, multi-walled carbon nanotubes, carbon nanofibers and graphite," *Composites: Part B*, Vol. 43, 2012, pp. 2079–2086.

[16] Inam, F., Vo, T., Jones, J. P., and Lee, X., "Effect of carbon nanotube lengths on the mechanical properties of epoxy resin: An experimental study," *Journal of Composite Materials*, Vol. 47, No. 19, 2012, pp. 2321–2330.

[17] Haggenmueller, R., Zhou, W., Fischer, J., and Winey, K., "Production and characterization of polymer nanocomposites with highly aligned single-walled carbon nanotubes," *Journal of nanoscience and nanotechnology*, Vol. 3, No. 1/2, 2003, pp. 105–110.

[18] Mahfuz, H., Adnan, A., Rangari, V., and Jeelani, S., "Manufacturing and Characterization of Carbon Nanotube/Polyethylene Composites," *International Journal of Nanoscience*, Vol. 4, No. 1, 2005, pp. 55–72.

[19] Haggenmueller, R., Gommans, H. H., Rinzler, A. G., Fischer, J. E., and Winey, K. I., "Aligned single-wall carbon nanotubes in composites by melt processing methods," *Chemical Physics Letters*, Vol. 330, 2000, pp. 219–225.

[20] Tang, W., Santare, M. H., and Advani, S. G., "Melt processing and mechanical property characterization of multi-walled carbon nanotube/high density polyethylene (MWNT/HDPE) composite films," *Carbon*, Vol. 41, 2003, pp. 2779–2785.

[21] Zou, Y., Feng, Y. amd Wang, L., and Liu, X., "Processing and properties of MWNT/HDPE composites," *Carbon*, Vol. 41, 2004, pp. 271–277.

[22] McNally, T., Poetschke, P., Halley, P., and et. al., "Polyethylene multiwalled carbon nanotube composites," *Carbon*, Vol. 46, 2005, pp. 8222–8232.

[23] Park, S., Yoon, S. W., Choi, H., Lee, J. S., Cho, W. K., Kim, J., Park, H. J., Yun, W. S., Choi, C. H., Do, Y., and Choi, I. S., "Pristine Multiwalled Carbon Nanotube/Polyethylene Nanocomposites by Immobilized Catalysts," *Chemistry of Materials*, Vol. 20, 2008, pp. 4588–4594.

[24] Zhang, X., Liu, T.a nd Sreekumar, T., Kumar, S., Moore, V., Hauge, R., and Smalley, R., "Poly(vinyl alcohol)/SWNT Composite Film," *Nano Letters*, Vol. 3, No. 9, 2003, pp. 1285–1288.

[25] Dyke, C. and Tour, J., "Overcomi ng the Insolubility of Carbon Nanotubes Through High Degrees of Sidewall Functionalization," *Chem. Eur. J.*, Vol. 10, 2004, pp. 812–817.

[26] Cadek, M., Coleman, J., Ryan, K., Nicolosi, V., Bister, G., Fonseca, A., Nagy, J., Szostak, K., Beguin, F., and Blau, W., "Reinforcement of Polymers with Carbon Nanotubes: The Role of Nanotube Surface Area," *Nano Letters*, Vol. 4, No. 2, 2004, pp. 353–356.

[27] Wagner, H. and Vaia, R., "Nanocomposites: issues at the interface," *Materials Today*, Vol. 7, No. 11, 2004, pp. 38–42.

[28] Desai, A. and Haque, M., "Mechanics of the interface for carbon nanotubepolymer composites," *Thin-Walled Structures*, Vol. 43, 2005, pp. 1787–1803.

[29] Rahmat, M. and Hubert, P., "Carbon nanotube-polymer interactions in nanocomposites: A review," *Composites Science and Technology*, Vol. 72, 2011, pp. 72–84.

[30] Wang, S., Liang, Z., Liu, T., Wang, B., and Zhang, C., "Effective amino-functionalization of carbon nanotubes for reinforcing epoxy polymer composites," *Nanotechnology*, Vol. 17, 2006, pp. 1551–1557.

[31] Ma, P., Zheng, Q., Mader, E., and Kim, J., "Behavior of load transfer in functionalized carbon nanotube/epoxy nanocomp osites," *Polymer*, Vol. 53, 2012, pp. 6081–6088.

[32] Zhu, J., Peng, H., Rodriguez-Macias, F., Margrave, J. L., Khabashesku, V. N., Imam, A. M., Lozano, K., and Barrera, E. V., "Reinforcing epoxy polymer composites through covalent integration of functionalized nanotubes," *Advanced functional materials*, Vol. 14, No. 7, 2004, pp. 643–648.

[33] Gong, X., Liu, J., Baskaran, S., Voise, R., and Young, J., "Surfactant-assisted processing of carbon nanotube/polymer composites," *Chemistry of Materials*, Vol. 12, No. 1049-1052, 2000.

[34] Coleman, J., Cadek, M., Blake, R., Nicolosi, V., Ryan, K., and Belton, C., "High-performance nanotube-reinforced plastics: understanding the mechanism of strength increase," *Advanced functional materials*, Vol. 14, No. 8, August 2004, pp. 791–798.

[35] Zhu, J., Peng, H., Rodriguez-Macias, F., Margrave, J., Khabashesku, V., Imam, A., Lozano, K., and Barrera, E., "Reinforcing epoxy polymer composites through covalent integration of functionalized nanotubes," *Advanced Functional Materials*, Vol. 14, No. 7, 2004, pp. 643–648.

[36] Barber, A., Cohen, S., and Wagner, H., "Measurement of Carbon Nanotube-Polymer Interfacial Strength," *Applied Physics Letters*, Vol. 82, No. 23, June 2003, pp. 4140–4142.

[37] Tsuda, T., Ogasawara, T., Deng, F., and Takeda, N., "Direct measurements of interfacial shear strength of multi-walled carbon nanotube/PEEK composite using a nano-pullout method," *Composites Science and Technology*, Vol. 71, 2011, pp. 1295–1300.

[38] Rafiee, R., Rabczuk, T., Pourazizi, R., Zhao, J., and Zhang, Y., "Challenges of the Modeling Methods for Investigating the Interaction between the CNT and the Surrounding Polymer," *Advances in Materials Science and Engineering*, Vol. 2013, 2013.

[39] Chen, X. and Liu, Y., "Square representative volume elements for evaluating the effective material properties of carbon nanotube-based composites," *Computational Materials Science*, Vol. 29, No. 1, 2004, pp. 1–11.

[40] Liu, Y. and Chen, X., "Evaluations of the effective material properties of carbon nanotube-based composites using a nanoscale representative volume element," *Mechanics of Materials*, Vol. 35, 2003, pp. 69–81.

[41] Liu, Y., Nishimura, N., and Otani, Y., "Large-scale modeling of carbon-nanotube composites by a fast multipole boundary element method," *Computational Materials Science*, Vol. 34, 2005, pp. 173–187.

[42] Seidel, G. and Lagoudas, D., "Micromechanical analysis of the effective elastic properties of carbon nanotube reinforced composites," *Mechanics of Materials*, Vol. 38, 2006, pp. 884–907.

[43] Hammerand, D., Seidel, G., and Lagoudas, D., "Computational micromechanics of clustering and interphase effects in carbon nanotube composites," *Mechanics of Advanced Materials and Structures*, Vol. 14, 2007, pp. 277–294.

[44] Seidel, G., Lagoudas, D., Frankland, S., and Gates, T., "Modeling functionally graded interphase regions in carbon nanotube reinforced composites," *Proceedings of the 20th ASC Technical Conference*, American Society for Composites, Drexel University, Philadelphia, PA, September 7-9 2005.

[45] Frankland, S., Harik, V., Odegard, G., Brenner, D., and Gates, T., "The stress-strain behavior of polymer-nanotube composites from molecular dynamics simulation," *Composites Science and Technology*, Vol. 63, 2003, pp. 1655–1661.

[46] Haghighatpanah, S. and Bolton, K., "Molecular-Level Computational Studies of Single Wall Carbon Nanotube-Polyethylene Composites," *Computational Materials Science*, Vol. 69, No. 443-454, 2013.

[47] Sul, J., Prusty, B. G., Kelly, D. W., and Christensen, S., "Application of molecular dynamics to evaluate the design performance of low aspect ratio carbon nanotubes infibre reinforced polymer resin," *Composites: Part A*, Vol. 65, 2014, pp. 64–72.

[48] Zhou, M., "A new look at the atomic level virial stress: on continuum-molecular system equivalence," *Proc. R. Soc. Lond. A*, Vol. 459, 2003, pp. 2347–2392.

[49] Mokashi, V., Qian, D., and Liu, Y., "A study on the tensile response and fracture in carbon nanotube-based composites using molecular mechanics," *Composites Science and Technology*, Vol. 67, No. 3-4, 2007, pp. 530–540.

[50] Khare, K. S., Khabaz, F., and Khare, R., "Effect of Carbon Nanotube Functionalization on Mechanical and Thermal Properties of Cross-Linked Epoxy-Carbon Nanotube Nanocomposites: Role of Strengthening the Interfacial Interaction," *Applied Materials and Interfaces*, Vol. 6, 2014, pp. 6098–6110.

[51] Odegard, G., Gates, T., Wise, K., Park, C., and Siochi, E., "Constitutive modeling of nanotube-reinforced polymer composites," *Composites Science and Technology*, Vol. 63, 2003, pp. 1671–1687.

[52] Odegard, G., Frankland, S., and Gates, T., "Effect of Nanotube Functionalization on the Elastic Properties of Polyethylene Nanotube Composites," *AIAA Journal*, Vol. 43, No. 8, August 2005, pp. 1828–1835, AIAA-9468-376.

[53] Wagner, H., "Nanotube-polymer adhesion: a mechanics approach," *Chemical Physics Letters*, Vol. 361, July 2002, pp. 57–61.

[54] Frankland, S., Caglar, A., Brenner, D., and Griebel, M., "Molecular simulation of the influence of chemical cross-links on the shear strength of carbon nanotube-polymer interfaces," *Journal of Physical Chemistry B*, Vol. 106, 2002, pp. 3046–3048.

[55] Gou, J., Minaie, B., Wang, B., Liang, Z., and Zhang, C., "Computational and experimental study of interfacial bonding of single-walled nanotube reinforced composites," *Computational Materials Science*, Vol. 31, 2004, pp. 225–236.

[56] Lau, K., "Interfacial bonding characteristics of nanotube/polymer composites," *Chemical Physics Letters*, Vol. 370, 2003, pp. 399–405.

[57] Xian, T. and Liao, K., "A nonlinear pullout model for unidirectional carbon nanotube-reinforced composites," *Composites: Part B*, Vol. 35, 2004, pp. 211–217.

[58] Jiang, L., Huang, Y., Jiang, H., Ravichandran, G., and et. al., "A cohesive law for carbon nanotube/polymer interfaces based on the van der Waals force," *Journal of the Mechanics and Physics of Solids*, Vol. 54, 2006, pp. 2436–2452.

[59] Awasthi, A., Lagoudas, D., and Hammerand, D., "Modeling of graphene-polymer interfacial mechanical behavior using molecular dynamics," *Modelling Simul. Mater. Sci. Eng.*, Vol. 17, 2009, pp. 15002–37.

[60] Dauber-Osguthorpe, P., Roberts, V. A., Osguthorpe, D. J., Wolff, J., Genest, M., and Hagler, A. T., "Structure and energetics of ligand binding to proteins: Escherichia coli dihydrofolate reductase-trimethoprim, a drug-receptor system," *Proteins*, Vol. 4, No. 1, 1988, pp. 31–47.

[61] Brenner, D., Shenderova, O., Harrison, J., Stuart, S., Ni, B., and Sinnott, S., "A second-generation reactive empirical bond order (REBO) potential energy expression for hydrocarbons," *Journal of Physics: Condensed Matter*, Vol. 14, 2002, pp. 783–802.

[62] Brenner, D., "Empirical potential for hydrocarbons for use in simulating the chemical vapor deposition of diamond films," *Physical Review B*, Vol. 42, No. 15, 1990, pp. 9458–9471.

[63] Stuart, S., Tutein, A., and Harrison, J., "A Reactive Potential for Hydrocarbons with Intermolecular Interactions," *J. Chem Phys.*, Vol. 112, No. 14, 2000, pp. 6472–6486.

[64] Jorgensen, W., Maxwell, D., and Tirado-RivesJ., "Development and Testing of the OPLS All-Atom Force Field on Conformational Energetics and Properties of Organic Liquids," *J. Am. Chem. Soc.*, Vol. 118, No. 45, 1996, pp. 11225–36.

[65] Dugdale, D., "Yielding of steel sheets containing slits," *Journal of the Mechanics and Physics of Solids*, Vol. 8, 1960, pp. 100–104.

[66] Barenblatt, G., "The mathematical theory of equilibrium cracks in brittle fracture," *Advances in Applied Mechanics*, Vol. 7, 1962, pp. 55–129.

[67] Alfano, M., Furgiuele, F., Leonardi, A., Maletta, C., and Paulina, G., "Cohesive Zone Modeling of Mode I Fracture in Adhesive Bonded Joints," *Key Engineering Materials Vols*, Vol. 348-349, 2007, pp. 13–16.

[68] Li, S., Thouless, M., Waas, A., Schroeder, J., and Zavattieri, P., "Use of a cohesive-zone model to analyze the fracture of a fiber-reinforced polymerCmatrix composite," *Composites Science and Technology*, Vol. 65, 2005, pp. 537–549.

[69] Bosch, M. v. d., Schreurs, P., and Geers, M., "An improved description of the exponential Xu and Needleman cohesive zone law for mixed-mode decohesion," *Engineering Fracture Mechanics*, Vol. 73, 2006, pp. 1220–12.

[70] Yu, D. and Liu, F., "Synthesis of Carbon Nanotubes by Rolling up Patterned Graphene Nanoribbons Using Selective Atomic Adsorption," *Nano Lett.*, Vol. 7, No. 10, 2007, pp. 3046–3050.

[71] Fan, C., Cagin, T., and Chen, Z., "Molecular Modeling of Polycarbonate. 1. Force Field, Static Structure, and Mechanical Properties," *Macromolecules*, Vol. 27, 1994, pp. 2383–2391.

[72] Dechant, J., *Polymer handbook. 3rd ed.*, New York: Wiley-Interscience, 1989.

[73] Liu, Y. and Chen, X., "Evaluations of the effective material properties of carbon nanotube-based composites using nanoscale representative volume element," *Mechanics of Materials*, Vol. 35, 2003, pp. 69–81.

[74] Mittal, V., editor, *Surface Modification of Nanotube Fillers*, John Wiley and Sons, 2011.

[75] Blond, D., Barron, V., Ruether, M., Ryan, K., Nicolosi, V., Blau, W., and Coleman, J., "Enhancement of Modulus, Strength, and Toughness in Poly(methyl methacrylate)-Based Composites by the incorporation of Poly(methyl methacrylate)-Functionalized Nanotubes," *Advanced Functional Materials*, Vol. 16, No. 12, 2006, pp. 1608–1614.

[76] Li, Y. and Seidel, D., "The Multiscale Modeling of the Effects of Nanoscale Load Transfer on the Effective Elastic Properties of Unfunctionalized Carbon Nanotube-Polyethylene Nanocomposites," *Modelling Simul. Mater. Sci. Eng.*, Vol. 22, No. 025023-50, 2014.

[77] Sanderson, R. T., *Chemical bonds and bond energy*, Vol. 21 of *Physical chemistry, a series of monographs*, Academic, New York, 1976.

[78] Nakane, K., Watanabe, N., and Iwahori, Y., "DCB Test Simulation of Stitched CFRP Laminates using Interlaminar Tension Test Results," *Composites Science and Technology*, Vol. 69, 2009, pp. 2315–2322.

[79] Ye, Y., Chen, H., Wu, J., and Chan, C., "Interlaminar Properties of Carbon Fiber Composites with Halloysite Nanotube-Toughened Epoxy Matrix," *Composites Science and Technology*, Vol. 71, 2011, pp. 717–723.

[80] Inam, F., Wong, D. W., Kuwata, M., and Peijs, T., "Multiscale Hybrid Micro-Nanocomposites Based on Carbon Nanotubes and Carbon Fibers," *Journal of Nanomaterials*, Vol. 2010, 2010, pp. 453420–32.

[81] Khare, K. and Khare, R., "Directed Diffusion Approach for Preparing Atomistic Models of Crosslinked Epoxy for Use in Molecular Simulations," *Macromolecular Theory and Simulations*, Vol. 21, 2012, pp. 322–327.

[82] Wang, S., Liang, R., Wang, B., and C., Z., "Covalent Addition of Diethyltoluenediamines Onto Carbon Nanotubes for Composite Application," *POLYMER COMPOSITES*, Vol. 30, 2009, pp. 1050–1057.

Appendix A

Parameters for CVFF

Table A.1: CVFF parameters used in the graphene-PE interface model

Masses				
Atom	Atomic mass(amu)			
C	12.01			
H	1.00			
Bond parameters				
bond type	r_0(Å)	K_b(Kcal $mole^{-1}$)		
C-C(PE)	1.526	322.7158		
C-H(PE)	1.105	340.6175		
C-C(graphene)	1.340	480.0000		
Angel parameters				
Angle type	θ_0(degree)	K_θ(Kcal $mole^-1$)		
C-C-C(PE)	110.5	46.6		
H-C-H(PE)	106.4	39.5		
H-C-C(PE)	110.0	44.4		
C-C-C(graphene)	120.0	90.0		
Torsion parameters				
Dihedral type	ϕ_0(degree)	K_ϕ(Kcal $mole^{-1}$)	d	n
-C-C-(PE)	0	0.158	1	3
-C-C-(graphene)	180	3.000	1	2
Van der Waals parameters				
Atom type	ε	σ		
C(PE)	0.08	3.4745		
H(PE)	0.019	2.45		
C(graphene)	0.074	3.617		
r_c =10 Å				

Appendix B

Formula of AIREBO

The AIREBO potential is the sum over three parts, including the covalent bonding(REBO) interactions, non-bonded(LJ) interactions and torsion interactions.

The REBO potential accounts for the covalent bonding interactions using the form developed by Tersoff,

$$E_{ij}^{REBO} = V_{ij}^{R}(r_{ij}) + b_{ij}V_{ij}^{A}(r_{ij}) \tag{B.1}$$

The repulsive interaction V_{ij}^{R} is described using the following formula,

$$V_{ij}^{R} = w_{ij}(r_{ij})[1 + Q_{ij}/r_{ij}]A_{ij}e^{-\alpha_{ij}r_{ij}} \tag{B.2}$$

where the parameters Q_{ij}, A_{ij} and α_{ij} depend on the type of i and j atoms, the w_{ij} term is a bond-weighting factor which is responsible to switch off the covalent bond interaction as the atom pairs exceed the maximum bonding distances,

$$w_{ij} = S^{'}(t_c(r_{ij})) \tag{B.3}$$

The switching function $S^{'}(t)$ has the form,

$$S^{'}(t) = \Theta(-t) + \Theta(-t)\Theta(1-t)\frac{1}{2}[1 + cos(\pi t)] \tag{B.4}$$

where $\Theta(t)$ represents the Heaviside step function.

A scaling function is defined for the switching region of each type of bonds,

$$t_c(r_{ij}) = \frac{r_{ij} - r_{ij}^{min}}{r_{ij}^{max} - r_{ij}^{min}} \tag{B.5}$$

The attractive interaction V_{ij}^{A} is defined using a exponential,

$$V_{ij}^{A} = -w_{ij}(r_{ij}) \sum_{n=1}^{3} B_{ij}^{(n)} e^{-\beta_{ij}^{n} r_{ij}} \tag{B.6}$$

where the parameters B_{ij}, and β_{ij} are determined by the type of i and j atoms.

The b_{ij} term in Equation B.1 defines the bond order of the covalent bonded between the i^{th}

and j^{th} atoms, which is larger for stronger bonds. It accounts for all the chemical effects and modifies the strength of a bond according to the local environment.

$$b_{LJ} = \frac{1}{2}[p_{ij}^{\sigma\pi} + p_{ji}^{\sigma\pi}] + \pi_{ij}^{rc} + \pi_{ij}^{dh} \tag{B.7}$$

in which $p_{ij}^{\sigma\pi}$ gives the covalent bond interaction and depends on the bond angle θ_{ijk}, π_{ij}^{rc} includes all the contributions to the bond order from radical and conjugation effects, π_{ij}^{dh} introduces a penalty for rotation around multiple bonds around i and j atoms.

The non-boned interactions are described by the use of the LJ potential,

$$E_{ij}^{LJ}(r_{ij}) = S(t_r(r_{ij}))S(t_b(b_{ij}^*))C_{ij}V_{ij}^{LJ}(r_{ij}) + [1 - S(t_r(r_{ij}))]C_{ij}V_{ij}^{LJ}(r_{ij}) \tag{B.8}$$

where the universal switching function $S(t)$ is in the form,

$$S(t) = \Theta(-t) + \Theta(-t)\Theta(1-t)[1 - t^2(3-2t)] \tag{B.9}$$

The magnitude of the LJ terms depends on the change of r_{ij} and is determined by the scaling functions,

$$t_c(r_{ij}) = \frac{r_{ij} - r_{ij}^{LJmin}}{r_{ij}^{LJmax} - r_{ij}^{LJmin}} \tag{B.10}$$

The scaling function $t_b(b_{ij})$ in the second switching function $S(t_b(b^*_{ij}))$,

$$t_b(b_{ij}) = \frac{r_{ij} - r_{ij}^{LJmin}}{r_{ij}^{LJmax} - r_{ij}^{LJmin}} \tag{B.11}$$

LJ interactions only exist if the atoms i and j are not connected by three or fewer intermediate atoms which criterion is represented by C_{ij} connectivity switch,

$$C_{ij} = 1 - max w_{ij}(r_{ij}), w_{ik}(r_{ik})w_{kj}(r_{kj}), \forall k w_{ik}(r_{ik})w_{kl}(r_{kl})w_{lj}(r_{lj}), \forall k, l \tag{B.12}$$